Chapter 1

Introduction

The field of perovskite manganites started with the seminal paper of Jonker and Van Santen in 1950 [1]. The existence of ferromagnetism in mixed crystals of $LaMnO_3$-$CaMnO_3$, $LaMnO_3$-SrMnO3, and $LaMnO_3$-$BaMnO_3$ was investigated. The perovskite structure of manganites is illustrated in Fig. 1.1. Jonker and Van Santen adopted the terminology "manganites" to refer to these mixed compounds. Being a representative family of strongly-correlated electron system, manganites have been subject of extensive researches in their magnetic, structural and electronic properties $[2-13]$. In particular, in various hole-doped manganites, the colossal magnetoresistance (CMR) effect, manifested by a paramagnetic-ferromagnetic transition at the Curie temperature (T_C) accompanied by a dramatic decrease in resistivity around a similar temperature (T_{IM}), has been ubiquitously observed and attributed to the charge-spin interaction of mixed-valence Mn^{3+}/ Mn^{4+} ions via Zener's seminal double-exchange (DE) mechanism $[14-15]$. However, it has been pointed out that DE alone might be inadequate to explain the observed CMR effect in $La_{1-x}Sr_xMnO_3$ and the incorporation of polaron effect induced by electron-phonon interactions arising from the Jahn-Teller splitting of the Mn d-levels could be essential [16]. Below T_C the mixed valence manganites commonly behave as ferromagnetic metals. This behavior becomes

obvious, if trivalent La in the parent compound $LaMnO_3$ is substituted by divalent ions, in that the missing electron produces a hole by driving the Mn^{3+} into Mn^{4+} state. The crystal field interactions split the 5 $3d$-orbitals of Mn into 3 t_{2g} and 2 e_g orbitals. Therefore, the e_g orbital is occupied by one electron in case of Mn^{3+} and is empty for Mn^{4+} which makes the former subject to Jahn–Teller distortion.
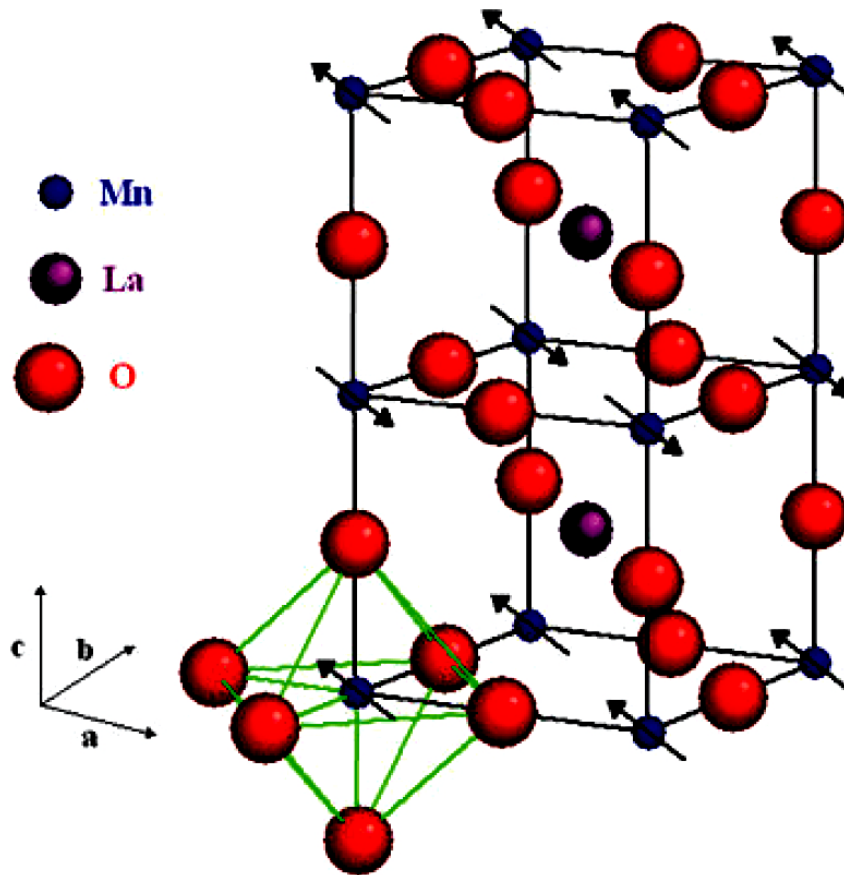

Figure 1.1 Arrangement of ions in the perovskite structure of manganites.

Owing to the rich, exotic, and profound physical properties and enormous MR, the discovery of colossal magnetoresistance in ABO_3 type perovskites recently has brought in intensive interest in fundamental of physics and potential applications. The rich phase diagram established for manganites [8－24] and the realization of "spin-based electronic devices" [25] are just a few representative examples demonstrating the vigorous activities in

this field. The magnetic and transport properties of these compounds vary sensitively with changing chemical pressure by introducing trivalent rare-earth ions of different sizes into the perovskite structure without affecting the valence of the Mn ions. Thus, applying stress could alter the electronic states significantly, resulting in a large change of T_C. It is generally regarded that a compressive/tensile strain can induce an increase/decrease in T_C by an increase/decrease in electron transfer ascribe to the compressed/expanded Mn–O bond lengths [16, 26－28]. In addition, the content of oxygen in $LaMnO_3$ also plays a crucial role on the magnetic and electric transport properties [7, 26－29]. It is believed that the increase/decrease insulator-metal transition temperature and associated transport properties are mostly resulting from the excessive/reduced oxygen content.

The strong interaction and some time competition of the (spin, charge, lattice and orbital) active degrees of freedom have shown a variety of interesting of crystallographic, electronic, and magnetic properties in the hole-doped perovskite manganites [8－24]. On the other hand, efforts in trying to substitute La-ion with tetravalent ions and hence make the manganites electron-doped have been rather inconclusive. Joseph Joly et $al.$ [30] argued that, due to the ion size constraints, it is almost impossible to replace the trivalent La^{3+} ion by tetravalent ions in polycrystalline manganite bulks prepared by solid state reaction. Indeed, early attempts of preparing Ce-doped $R MnO_3$ (R=La, Pr, Nd) manganites by Das and Mandal [31] all showed signatures of mixed-phases and hence blurred the interpretation of the obtained results. In particular, the replacement of tetravalent ions to La^{3+} often led to the self-doped $La_{1-x}MnO_{3-\delta}$ with localized multiphase compounds, which might give rise to very similar magneto-transport properties to those of the hole-doped manganites and jeopardize the genuine electron-doped characteristics [32, 33]. In this dissertation, we study the magnetic, transport, structural properties and microstructure of $La_{1-x}Sn_xMnO_3$ (LSnMO) system. We believed this field is less well-known, nevertheless, but is worth of further studies. We present

the efforts toward the understanding of the profound and exotic phenomena manifested by the tetravalent ion doped colossal manganites.

This dissertation consists of six chapters. We give the introduction in Chapter 1. In Chapter 2, we will describe the basic concepts and origin of magnetism for colossal magnetoresistive (CMR) oxides. The related papers will be surveyed and discussed. The magneto-transport properties of epitaxial $La_{0.7}Sn_{0.3}MnO_3$ manganite thin films on $SrTiO_3$ will be presented in Chapter 3. Three samples with various deposition conditions were prepared. The structural, transport and magnetic properties of these samples are reported in this chapter. The evolution of the crystal structure will also be described. In Chapter 4, we present the results of the magnetotransport properties, electronic structure, and microstructure of $La_{0.7}Sn_{0.3}MnO_3$ thin films on $LaAlO_3$ substrate. In this chapter, various post treatments for the preparation of LSnMO samples will be systematically studied and some outstanding issues will be clarified. The studies reported in this chapter provide conclusive evidences about that post anneal under O_2 or Ar at high temperatures may not be a viable approach for fabricating the so-called "electron-doped" manganites. In Chapter 5, the phase diagram and magnetic properties of the electron doping $La_{1-x}Sn_xMnO_3$ manganites will be presented. Here, the LSnMO family will be discussed systematically and the magnetic phase diagram will be established. Besides, the influence of the Sn content on the physical properties of the LSnMO will be depicted. Finally, we will give a summary in Chapter 6.

Chapter 2

Colossal magnetoresistive oxides

2.1 Introduction
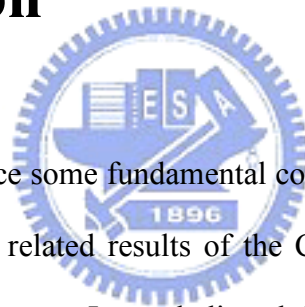
In this chapter, we introduce some fundamental concepts of the colossal magnetoresistive (CMR) oxides and survey the related results of the CMR, hole doped and electron doping manganites reported in the literature. It was believed that the valence of the Mn-ions may be altered from purely Mn^{3+} in the parent compound $LaMnO_3$ to the mixture of Mn^{3+}/Mn^{4+} or Mn^{2+}/Mn^{3+} by doping with divalent ions (Ca^{2+}, Sr^{2+}, Ba^{2+}…) or tetravalent ions (Ce^{4+}, Sn^{4+}, Te^{4+}…). The e_g electron can hop between Mn^{3+}/Mn^{4+} or Mn^{2+}/Mn^{3+} to lower the total energy via the interaction with O $2p$. Owing to their profound physical properties which might eventually open up a vast field of application potential, these kinds of compounds soon attracted a great deal of attention. In particular, the research interest has been mostly focused on the several key physical parameters of the system that appeared to experience various interactions of the same order of energy scale. We will concentrate on the Sn doped $LaMnO_3$ reported in the literature and discuss the issues remained to be clarified.

2.2 Double exchange

The concept of the double-exchange (DE) interaction was introduced by Zener [14, 34−35] in order to explain the ferromagnetism of the perovskite manganites ABO_3. Zener's work is widely believed to provide a conclusive zero[th] order account for the manganites ferromagnetism. Mean-field type arguments of these models, including those by de Gennes [36], also helped us to realize the magnetism of manganite compounds. The states of manganites become uniformly ferromagnetic to give a way for the charges to move freely in such a spin polarized state. Zener explained that the ferromagnetism was resulted from an indirect coupling between the Mn $3d$ incomplete d-shells, by means of the intermediates of O $2p$ conducting electrons. The manganites were addressed that the incomplete d-shell was the so-called t_{2g} electrons, and the conduction electron were the e_g electrons [3]. The basic process in the double-exchange mechanism is the hopping of the e_g electrons between Mn^{4+} and Mn^{3+} ions. This involves a simultaneously transfer of an electron from the Mn^{3+} site to the central oxide ion and an electron from the oxide ion to the Mn^{4+} site [37], as schematically depicted in Fig. 2.1.
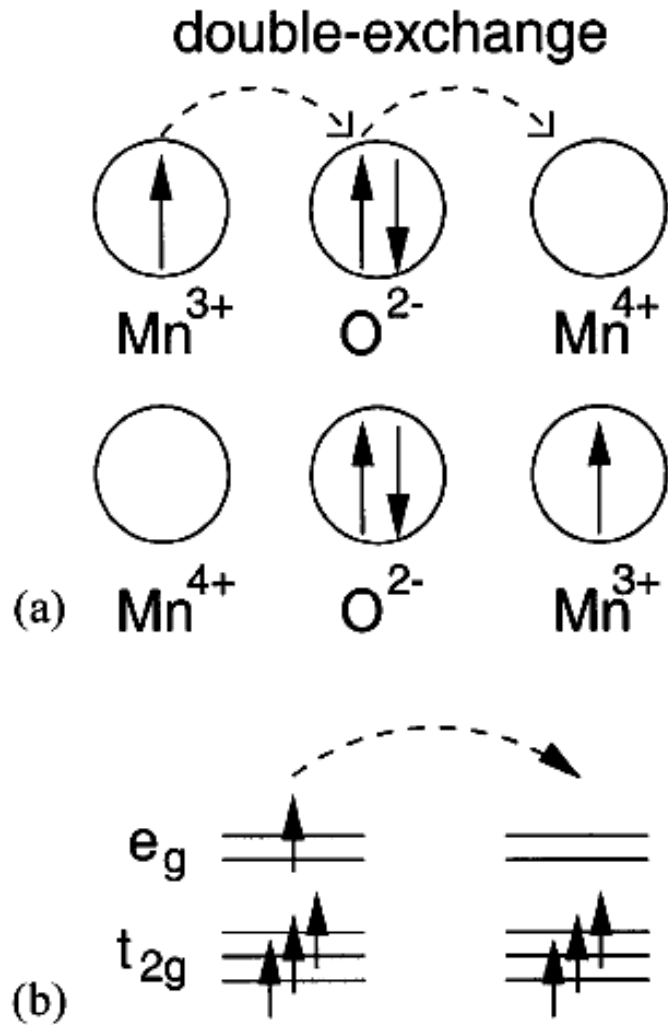
Figure 2.1: (a) Sketch of the Double Exchange mechanism which involves two Mn ions and one O ion. (b) The mobility of e_g-electrons increases if the nearby localized spins are polarized [37].

The seminal work of Zener was extended by Anderson and Hasegawa [15], who studied the proposed mechanism in greater detail. They explained that a better argument of the motion of electrons from Mn to Mn is to transfer electron one by one, still using the oxygen as a bridge between ions, rather than simultaneously as proposed by Zener. The work constructed by Anderson and Hasegawa indicated the effective hopping t_{eff} of an electron jumping between two nearest-neighbor Mn ions, can be written as $t_{eff} = t\cos\dfrac{\theta}{2}$, where θ is the angle

between t_{2g} spins located at two sites involved in the electron transfer, as shown in Fig. 2.2. These simple effective hopping ideas provided plausible interpretations for the obtained research results of manganites in the early days. However, currently it is well known that more elaborate theories are needed to explain the complexity of the phase diagrams of these compounds.
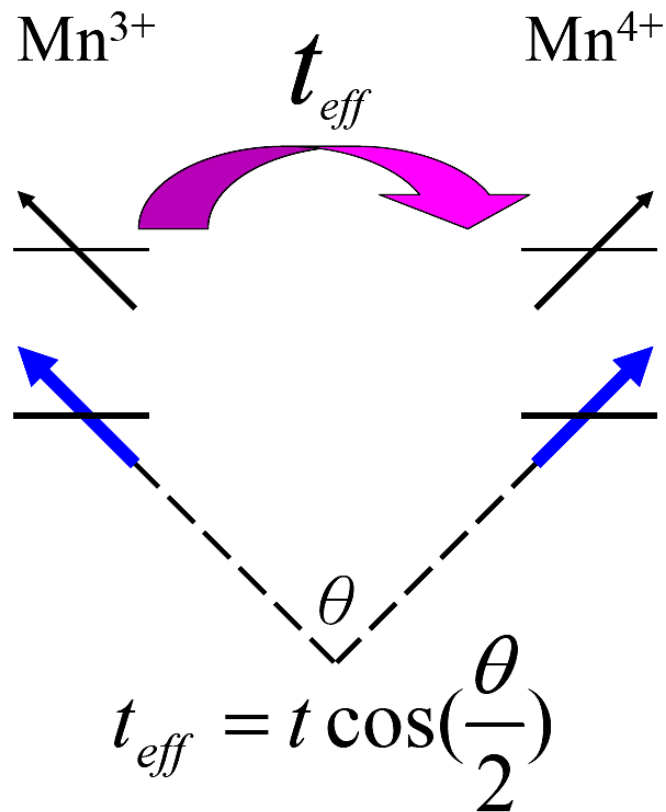

$$t_{eff} = t\cos(\frac{\theta}{2})$$

Figure 2.2: The effective hopping t_{eff} of an electron jumping between two nearest-neighbor Mn ions (reproduced from Ref. [38]).

2.3 Crystal field splitting and Jahn-Teller distortion

The LaMnO$_3$ has one electron occupies the e_g orbital of the $3d$ shell of a manganese ion. Although for an isolated ion a five-fold degeneracy exists for the $3d$-orbitals, this degeneracy is partially lifted by the crystal field due to the six oxygen ions surrounding the manganese forming an octahedron. This has been analyzed by the ligand field theory to show that the five-fold degeneracy is lifted into doubly degenerate e_g-orbitals ($d_{x^2-y^2}$ and $d_{3z^2-r^2}$) and triply degenerate t_{2g}-orbitals (d_{xy}, d_{yz}, and d_{zx}) [37, 38]. If including the consideration of Jahn-Teller effect, the doublet degenerate e_g state splits into $d_{x^2-y^2}$ and $d_{3z^2-r^2}$ states; the triplet degenerate t_{2g} state splits into d_{xy}, d_{yz}, and d_{zx} states, as illustrated in Fig. 2.3. It reveals that the energy level for the three t_{2g}-orbitals is lower than that for the two e_g-orbitals [37, 38]. The distributions of the five d orbitals electron clouds are also displayed in Fig. 2.4.
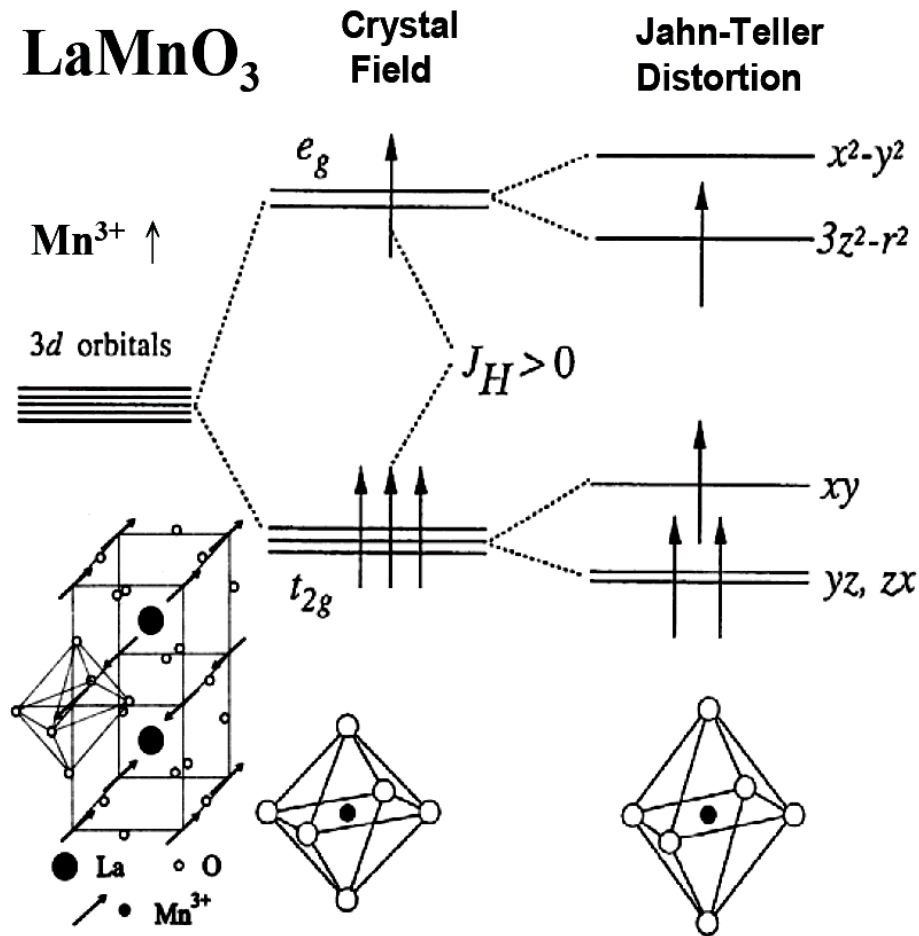

Figure 2.3: Field splitting of the five-fold degenerate atomic $3d$ levels into two t_{2g} and three e_g levels [38].
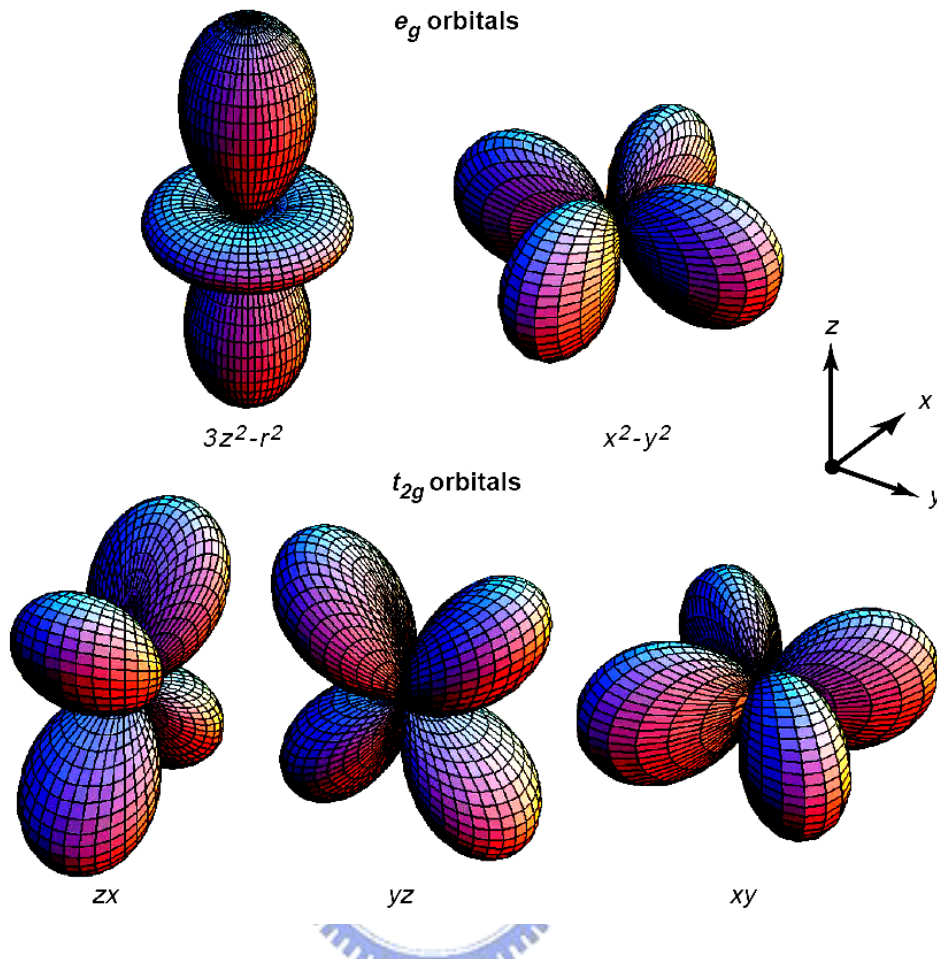
9

Figure 2.4: The electron distribution of five d orbital. In the cubic crystal field, this fivefold degeneracy is split into two e_g orbitals [(x^2-y^2) and ($3z^2-r^2$)] and three t_{2g} orbitals [(xy), (yz), and (zx)][2].

Nevertheless, the investigations of these models which are motivated by the observation of colossal magnetoresistance (CMR) phenomena [37, 12] in manganites revealed that such simplified treatments are inadequate to explain the observed experimental results quantitatively. It was pointed out that the Curie temperature determined from theoretical calculation was not consistent with the experimental results, and the resistivity was too small for theoretical prediction. Curie temperature T_C of the model has been estimated by Millis *et al*. [16]. Using some appropriate values for t and J_H, they found that the mean field T_C of the

model is much larger than those for perovskite manganites $La_{1-x}Sr_xMnO_3$, and concluded that double exchange alone is insufficient to explain the thermodynamics of these manganites. Millis *et al.* [39] reached this conclusion by demonstrating the manifestations of the critical Curie temperature and of the resistivity within the framework of double-exchange mechanism, and argued that the polaron effect should be involved. They also suggested that the ratio $\lambda_{eff} = \dfrac{E_{JT}}{t_{eff}}$ predominates the physics of the problem. Here E_{JT} is the static Jahn-Teller distortion trapping energy at a given octahedron, and t_{eff} is an effective hopping matrix element that is temperature dependent following the standard DE discussion. It appeared that as the temperature is higher than T_C, the effective coupling λ_{eff} could become larger due to electron localization and, in turn, lead to insulator behavior. On the other hand, when λ_{eff} becomes smaller than the critical value below T_C, it becomes smaller due to electron delocalization and metallic behavior [37].

2.4 LaMnO$_3$ and Lanthanum-deficiency manganites La$_{1-x}$MnO$_3$

LaMnO$_3$, (LMO) being the parent compound of the CMR manganese oxides, is very important for understanding the properties of these materials. There have been studies of the structural and magnetic properties of LMO materials [5, 16, 40−49]. The crystal structure of LaMnO$_3$ is perovskite, with Mn being located at the center, oxygen at the face center and La at the corner of the cubic perovskite structure, respectively. There are four $3d$ electrons: three t_{2g} electron and one e_g electron for Mn-ions in LaMnO$_3$. The e_g electron can hop to neighbor e_g electron via the "super exchange interaction". Consequently, LaMnO$_3$ is an antiferromagnetic insulator with Mn being valence of 3+. The Mn^{3+} spin order is parallel in

the plane and antiparallel between the planes. The pure LaMnO$_3$ compound has a distorted perovskite structure and is antiferromagnetic below T_N=140 K. It exhibit ferromagnetic ordering in *ab* planes and antiferromagnetic ordering along the *c* axis. As the divalence ions (Ca, Sr, Ba, Pb) are doped onto the La sites, the material may present ferromagnetism, antiferromagnetism, or charge ordering insulator and other kinds of phases depending on the doping amount.

However, the family of La-deficiency manganites, La$_x$MnO$_3$ also attracted much attention due to the similar magnetic and transport behavior when comparing with the CMR manganites [29, 32－33, 50－63]. Gupta *et al*. [32] systematically studied the epitaxial thin films of lanthanum-deficient La$_x$MnO$_{3-\delta}$ (0.67＜x＜1) grown on (100) SrTiO$_3$ substrates by pulsed laser deposition (PLD). It revealed that the as-deposited films exhibit a ferromagnetic transition at temperatures ranging from 115 to 240 K, with the transition temperature (T_C) increasing with higher La deficiency, as displayed in Fig. 2.5. The relationships of resistivity and *x* are also presented in Fig. 2.6. The lanthanum-deficient La$_x$MnO$_{3-\delta}$ (0.67＜x＜1) thin films exhibited similar behaviors with the samples investigated in the divalent ions substituted La$_{1-x}$A$_x$MnO$_3$ (A＝Ba, Sr, Ca, Pb) thin films. In addition, post annealing the films in O$_2$ environments may reduce the resistivity and increase the T_C to values close to room temperature. A magnetoresistance value of 130% ($\Delta\rho$ /ρ_H) has been obtained at 300 K at 4 T for a post-annealed film with *x*＝0.75. The results reported by the researchers [29, 32－33, 50 － 63] provided us crucial experimental evidences for the properties of the lanthanum-deficient manganites La$_x$MnO$_{3-\delta}$ system. It revealed that, owing to the resembling transport and magnetic properties between the divalent ions substituted manganites La$_{1-x}$A$_x$MnO$_3$ and lanthanum-deficient manganites La$_x$MnO$_3$, in fact, the usual experimental data were inadequate to differentiate their genuine mechanism in nature. These facts point out that the transport and magnetic behaviors taken from the experimental measurement of lanthanum-deficient manganites can not be excluded for the studies of CMR materials.
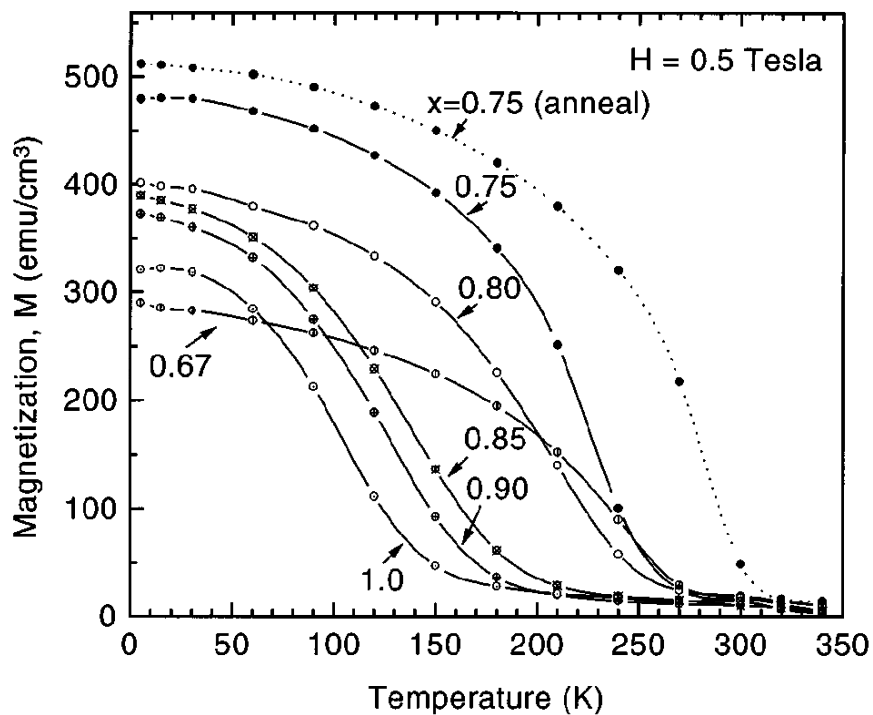
Figure 2.5: The $M(T)$ for the as prepared La$_x$MnO$_{3-\delta}$ films of different compositions in a magnetic field of 0.5 T [32].
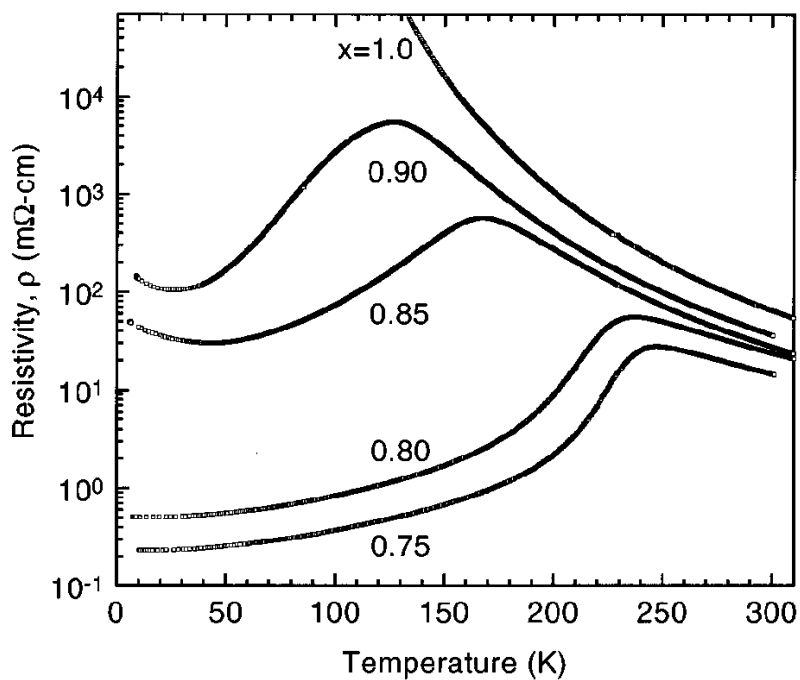

Figure 2.6: Resistivity as a function of temperature for La$_x$MnO$_{3-\delta}$ films of different composition [32].

2.5 Hole doped manganites

In the study of manganites, considerable emphasis has been given to the analysis of $La_{1-x}Sr_xMnO_3$. The lattice structure of Sr-doped perovskite manganite is displayed in Fig. 2.7. The Curie temperature T_C as a function of hole doping is relatively high, providing great application possibilities. It has also been observed that $La_{1-x}Sr_xMnO_3$ presents a complex behavior near $x = 1/8$. Resistivities vs. temperature for this compound at several densities are shown in Fig. 2.8. From these transport measurements, the phase diagram of this compound can be determined, as is demonstrated in Fig. 2.9. At hole concentrations such as $x = 0.4$, the system is metallic even above T_C. At densities above $x = 0.5$ an interesting A-type antiferromagnetic metallic state is stabilized, with ferromagnetism in planes and antiferromagnetism between neighboring planes. When the hole density is lowered to slightly below $x = 0.30$, the state above T_C becomes an insulator. It is this unexpected property of paramagnetic state transforming into metallic state with reducing temperature that stimulates extensive researches over the years [37].
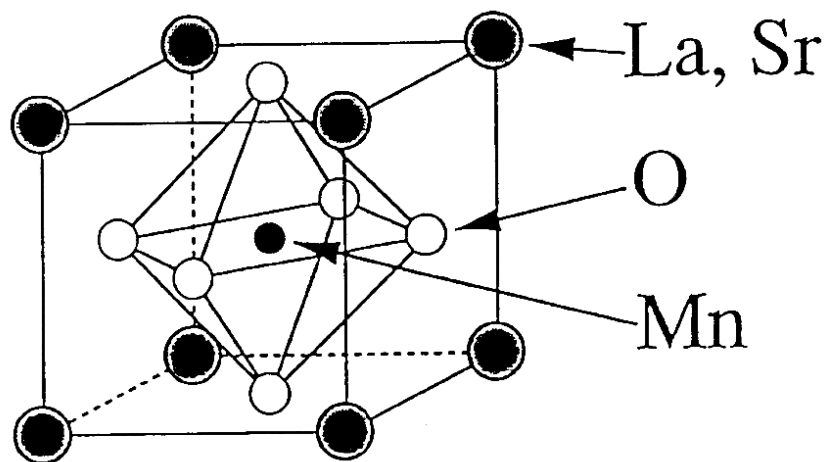

Figure 2.7: Lattice structure of Sr-doped perovskite manganite [37].
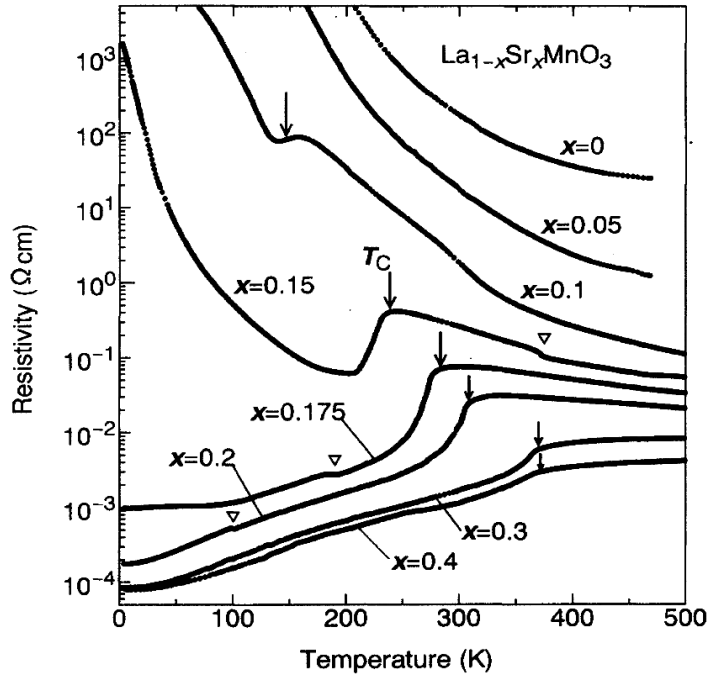
Figure 2.8: Temperature dependence of resistivity for various single crystals of $La_{1-x}Sr_xMnO_3$.

↓: Curie temperature. ▽: the anomalies due to structural transitions [64].
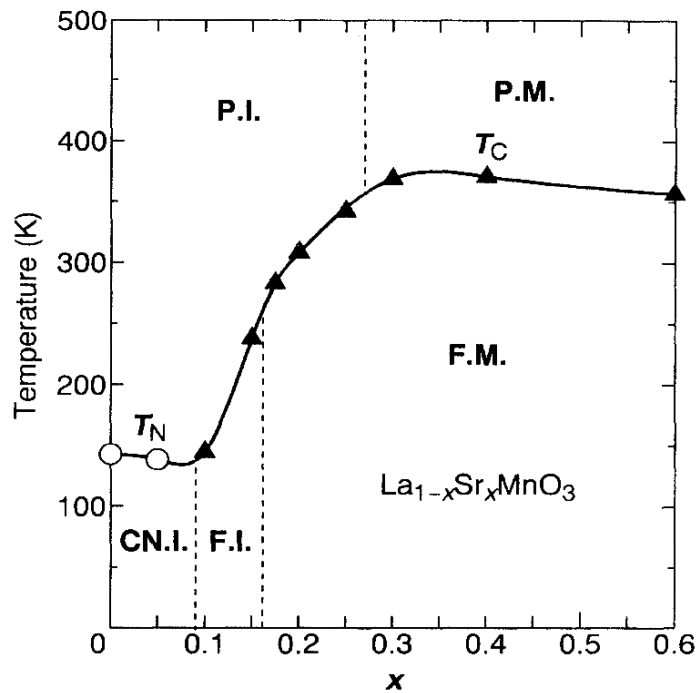

Figure 2.9: Electronic phase diagram of $La_{1-x}Sr_xMnO_3$. The AFM phase at large x is an A-type

AF metal with uniform orbital order. PM, PI, FM, FI, and CI denote paramagnetic metal,

paramagnetic insulator, FM metal, FM insulator, and spin-canted insulator states, respectively.

T_C is the Curie temperature and T_N is the Néel temperature [64].

In addition, the other conspicuous CMR material is the Ca-doped manganites, $La_{1-x}Ca_xMnO_3$. The properties of $La_{1-x}Ca_xMnO_3$ are very important and will be discussed in the followings. $La_{1-x}Ca_xMnO_3$ has been widely investigated since the early days of manganite studies [1]. In particular, it has been declared that $La_{1-x}Ca_xMnO_3$ has a large MR effect. Fig. 2.10 showed the results reported by Schiffer et al. [5] at $x=0.25$ showing the magnetization and resistivity as a function of temperature, and the existence of a robust MR. The drop in $\rho_{dc}(T)$ with decreasing temperature and the peak in MR are correlated with the ferromagnetic transition in the magnetization. The complete phase diagram of $La_{1-x}Ca_xMnO_3$, based on magnetization and resistivity measurements, was reproduced in Fig. 2.11. It was found that the FM phase actually occupies just a fraction of the whole diagram, indicating that DE alone does not provide a complete understanding of the manganites. For instance, equally prominent are the charge ordered (CO) states between $x=0.50$ and 0.87. The CO state at $x=0.50$ was proposed by Wollan and Koehler [41] as a CE-state. The experimental results reported by Ramirez et al. [65] were attributed to strong electron-phonon coupling, in agreement with the predictions of Millis et al. in the CO-states [16, 37].

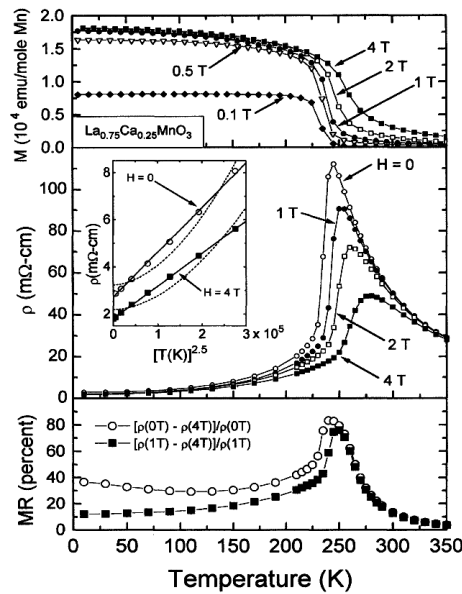Figure 2.10: The magnetization, resistivity, and magnetoresistance of $La_{1-x}Ca_xMnO_3$ ($x=$ 0.25), as a function of temperature at various fields (reproduced from [5]).
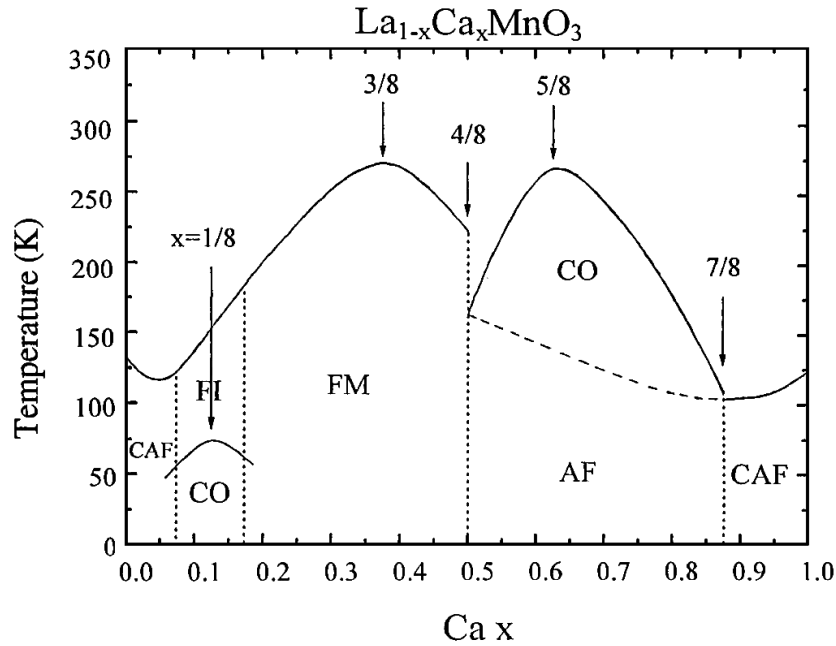
Figure 2.11: Phase diagram of $La_{1-x}Ca_xMnO_3$, constructed from the experimental measurements results of the transport and magnetic properties. FM: Ferromagnetic Metal, FI: Ferromagnetic Insulator, AF: Antiferromagnetism, CAF: Canted AF, and CO: Charge/Orbital Ordering. [38].

2.6 Electron doped manganites

In this section, we would like to introduce some notable electron doped manganites. In Ce-doped $RMnO_3$ manganites, the rare earth ions are partially replaced with cerium ions instead of divalent alkaline earth metals. These compounds are very sensitive to annealing. In fact, the results of preparing Ce-doped $RMnO_3$ (R＝La, Pr, Nd) manganites by Das and Mandal [31] all led to the mixed-phases composed by Ce-compounds and La-deficiency manganites. Nevertheless, the $La_{1-x}Ce_xMnO_3$ films were demonstrated to be single phase when being fabricated by PLD, as proposed by Mitra et al. [66－71]. They provided an x-ray absorption spectroscopic (XAS) study on thin films of $La_{0.7}Ce_{0.3}MnO_3$, as illustrated in Fig.

2.12. The measurements clearly showed that the cerium was in the Ce^{4+} valence state, and that the manganese was present in a mixture of Mn^{2+} and Mn^{3+} valence states, suggesting that $La_{0.7}Ce_{0.3}MnO_3$ was an electron-doped colossal magnetoresistive manganite. They claimed that it may open up opportunities for device applications as well as for further research on the colossal magnetoresistance phenomenon in these materials. Moreover, they reported the Ce-doped manganite on the electronic, transport, and magnetic properties. They believed the property of $La_{1-x}Ce_xMnO_3$ was similar to the hole-doped manganite $La_{1-x}Ca_xMnO_3$. The main difference is the fact that Ce doping drives the manganese in a mixture of Mn^{2+} and Mn^{3+} induced by electron doping. In addition, the magnetic phase diagram of $La_{1-x}Ce_xMnO_3$ was established, as shown in Fig. 2.13. It revealed that the phase diagram seems symmetry to that of hole-doped manganites.
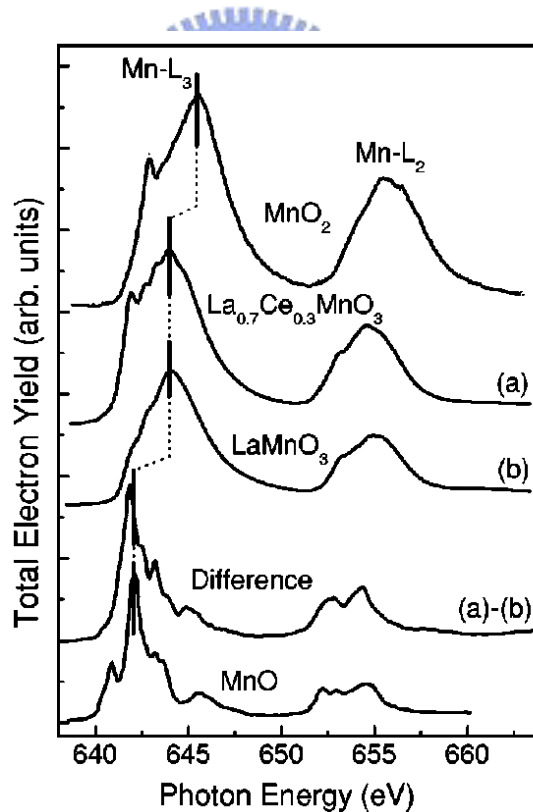

Figure 2.12: Mn-$L_{2,3}$ XAS spectra of $La_{0.7}Ce_{0.3}MnO_3$ (a) and for comparison of MnO_2 , $LaMnO_3$ (b) and MnO for Mn^{4+}, Mn^{3+} and Mn^{2+} references, respectively [67].
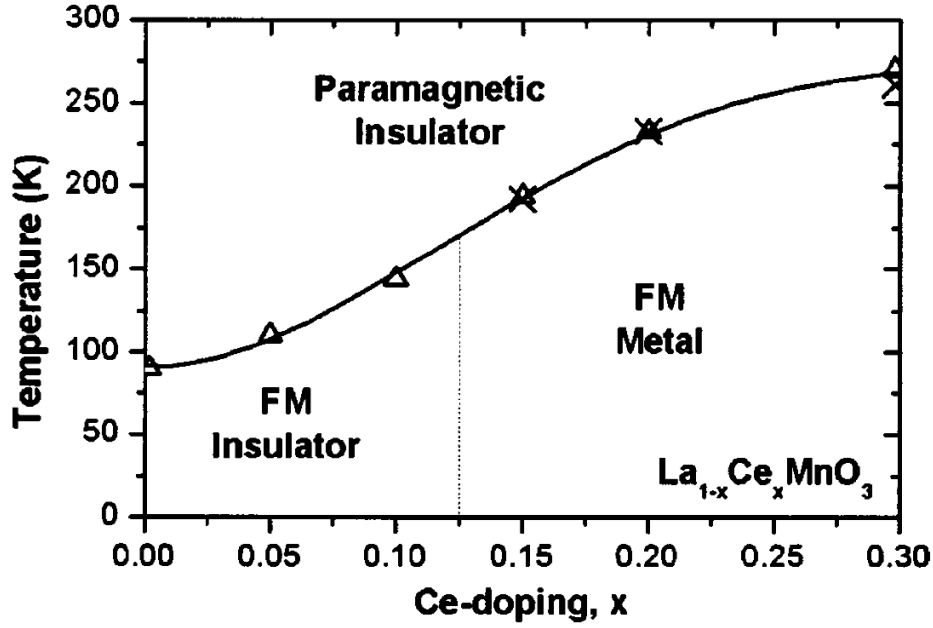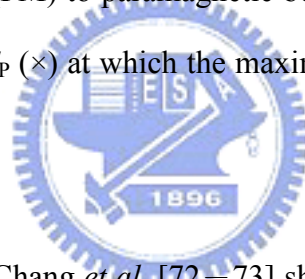
Figure 2.13: Magnetic phase diagram of $La_{1-x}Ce_xMnO_3$ in the doping range $0 < x < 0.3$. The transition from ferromagnetic (FM) to paramagnetic behavior was determined from T_C (Δ) as well as from the temperature T_P ($\times$) at which the maximum resistivity of the metallic samples occurs [66].

Moreover, the studies by Chang *et al.* [72−73] showed the single-phase $La_{0.7}Ce_{0.3}MnO_3$ thin films can be prepared on $SrTiO_3$ (100) substrates by PLD. The conditions for obtaining purely single-phase LCeMO films should be controlled within a very narrow window of substrate temperature and laser energy density. After that, the x-ray absorption spectroscopy (XAS), optical reflectance spectroscopy, and the Hall Effect measurements were carried out to investigate the electronic structure in $La_{0.7}Ce_{0.3}MnO_3$ thin films. Their LDA+U calculations results, as shown in Fig. 2.14−15 were consistent with the results of XAS. The Hall measurement results also indicated that in LCeMO the carriers display the characteristics of holes as LDA+U calculations predict. Therefore, they concluded that the doping electrons did not drive LCeMO into *n*-type manganite and the itinerant carriers were still holes, but with a much less concentration as compared with that of LCaMO.
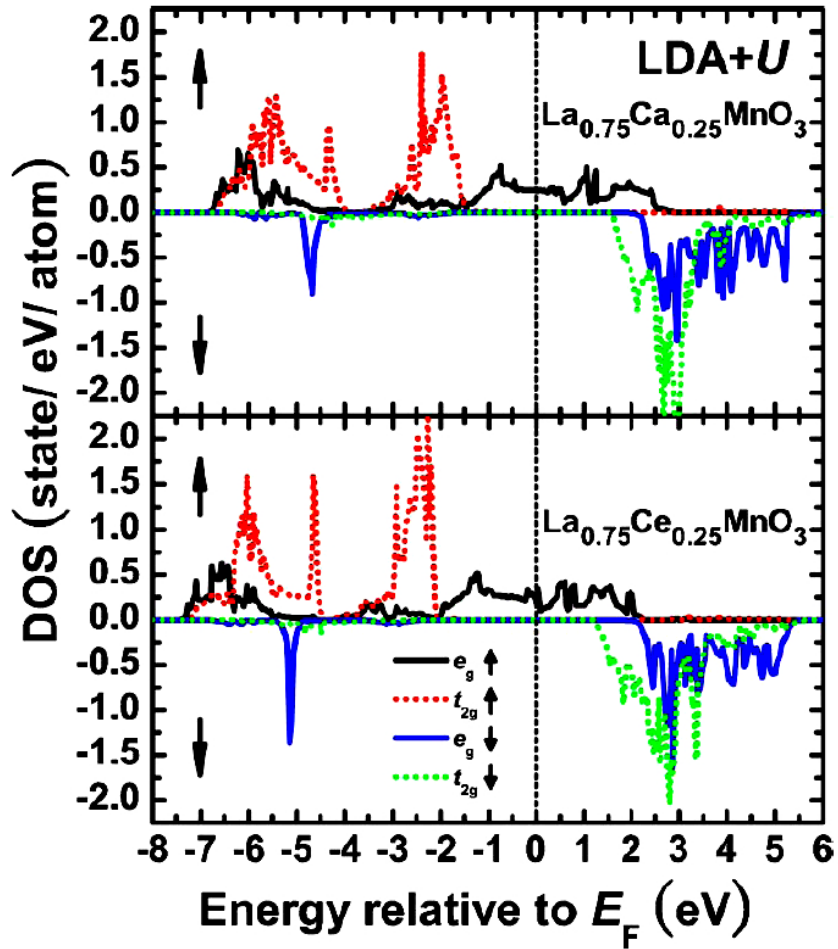
Figure 2.14: DOS of Mn 3*d* in LCaMO and LCeMO calculated by LDA+*U* method [73].
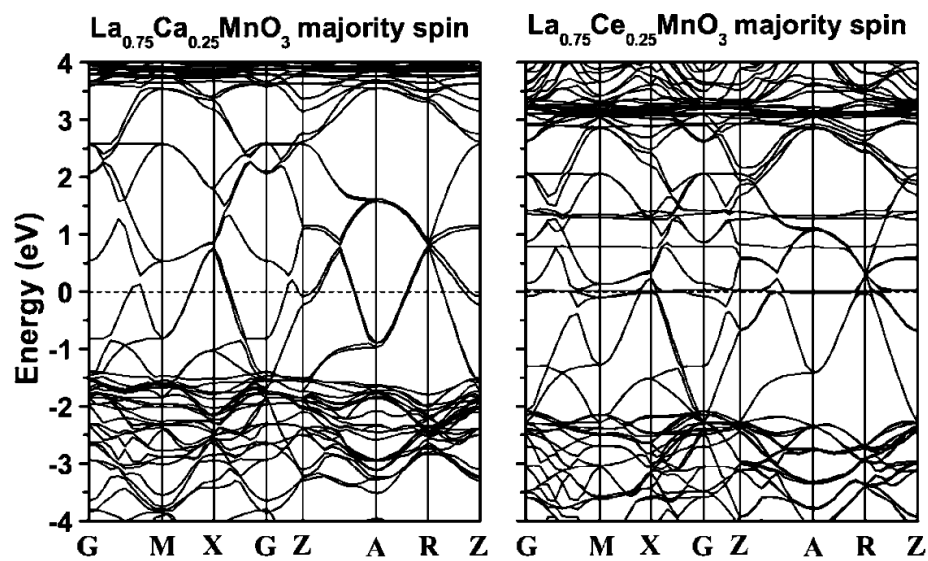

Figure 2.15: The results of LDA+*U* band structure calculations for LCaMO and LCeMO [73].

Nevertheless, unlike to the investigations mentioned above, the $La_{1-x}Ce_xMnO_3$ prepared by Kawai *et al*. [74－76] all exhibited significant ferromagnetic insulator behavior. The nature of metal-insulator transition and ferromagnetism phenomena of perovskite $La_{0.7}Ce_{0.3}MnO_3$ thin films was investigated. In particular, the effects of post-annealing under oxidization and reduction atmospheres on the electrical transport and magnetic properties were systematically examined. The metal-insulator transition temperature and the Curie temperature of ferromagnetism were found to be significantly influenced by the post-annealing and increase with increasing post-annealing temperature under both oxygen and argon atmospheres. In addition, the major carriers within the conductive films were identified to be holes from the results of Hall Effect measurement. Moreover, from the analysis of transmission electron spectroscopy (TEM) and electron dispersive x-ray analysis (EDX), as illustrated in Fig 2.16 and Table 2.1, they concluded that the cation deficiencies due to nanoclustering cerium oxides within the post-annealed films were responsible for the emergence of the metal-insulator transition and ferromagnetism phenomena.
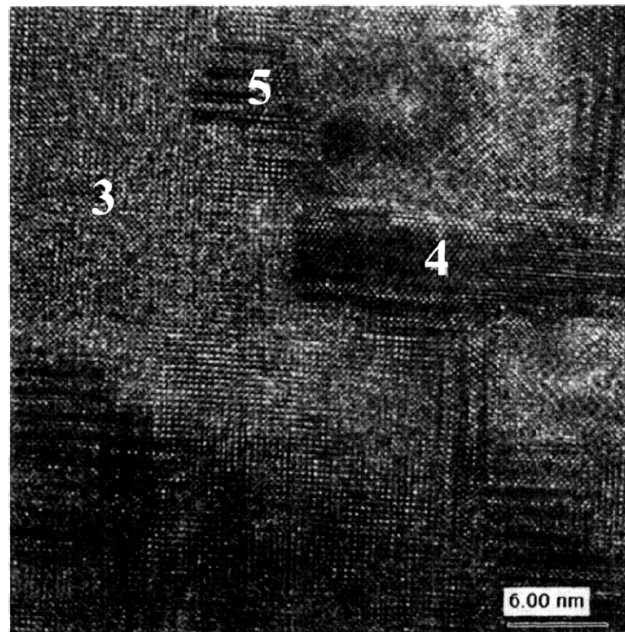

Figure 2.16: High-resolution TEM image of $La_{0.7}Ce_{0.3}MnO_3$ thin film post-annealed at 800 °C under oxygen atmosphere [75].

	Atomic ratio (%)		
	La	Mn	Ce
Point 3	46.90	51.67	1.43
Point 4	9.13	11.08	79.79
Point 5	29.72	29.12	41.16

Table 2.1: Averaged atomic cation ratio of films post-annealed at 800 °C under oxygen atmosphere [75].

In addition, the investigation of the tellurium (Te) doped manganites were also be proposed [77−81]. Tan *et al*. claimed that the Te-doped lanthanum manganite perovskite compound $La_{1-x}Te_xMnO_3$ was a good colossal magnetoresistance behavior according to the related magnetic and electrical properties. The magnetoresistance ratio MR＝$[\rho(0)-\rho(H)]/\rho(0)$ was about 63% for $x=0.04$ under an applied magnetic field of 40 KOe, and the resistivity of the compounds was primarily affected by temperature and the Te doping amount. Additionally, Chen *et al*. reported the Pr doped manganites $La_{1-x}Pr_xMnO_{3+\delta}$ ($x=0.3$) [82]. They prepared the sample by using solid-state reaction which showed semiconductor behavior, and no colossal magnetoresistance (CMR) effect. However, it significantly showed CMR behavior when it was annealed in a flowing argon. From the measurement of the x-ray photoemission spectroscopy, it revealed that Pr ions were in a mixed-valence state of Pr^{4+} and Pr^{3+} in the Pr doped manganite. Therefore, $La_{1-x}Pr_xMnO_3$ ($x=0.3$) could be an electron-doped CMR manganite. They argued that the excess oxygen induced the hole carriers, which will compensate the electrons. The samples annealed in argon flow for a long time exhibit metal-insulator transition and CMR effect induced by a reduction in oxygen content, and the $La_{0.7}Pr_{0.3}MnO_{3+\delta}$ had been transferred to $La_{0.7}Pr_{0.3}MnO_3$.

2.7 Sn-doped manganites

Recently, the discovery of a new manganite of composition $(La_{0.7}Sn_{0.3})_2Mn_2O_7$ in addition to the ABO_3 type that exhibited colossal magnetoresistance had been reported [83]. It was claimed that the new insights into the basic properties were likely to emerge from the investigations on the new materials and some of them may be more useful for applications. Besides, the transport properties of the polycrystalline $La_{1-x}Sn_xMnO_{3+\delta}$ with $x=0.1-0.5$ and of Fe-doped samples had been investigated [84]. It is concluded that the $La_{0.5}Sn_{0.5}MnO_{3+\delta}$ is a single phase material and the manganites $La_{1-x}Sn_xMnO_{3+\delta}$ with $x < 0.5$ consisted of two phases, ABO_3 and $A_2B_2O_7$ of which the chemical formulas were $LaMnO_{3+\delta}$ and $(La_{1-x}Sn_x)_2Mn_2O_7$, respectively. It is believed the colossal magnetoresistance (CMR) in appears to have its origin in deficient La and/or Mn ions in the ABO_3 phase. However, the results had been commented by A. Caneiro *et al.* [85], who provided the conclusive evidences of the x-ray diffraction data, SEM, EDS, and dc magnetization to demonstrate that the $La_{0.5}Sn_{0.5}MnO_{3+\delta}$ was a multiphase material composed mainly of $La_2Sn_2O_7$ and Mn_3O_4 which was not in agreement with a single-phase one of the composition $(La_{0.5}Sn_{0.5})_2Mn_2O_7$ as proposed in Refs, 83, 84 and 86.

The results of polycrystalline Sn doped $LaMnO_3$ manganites were also reported [87-90] after that. The results all revealed that the phases of the polycrystalline Sn doped $LaMnO_3$ manganites were composed of two type phase: ABO_3 and $A_2B_2O_7$. B. Revzin *et al.* [88] claimed the magnetic and magnetoresistive properties of polycrystalline ceramic $La_{0.67}Sn_{0.33}MnO_3$ indicated that the compound was found to be composed of 73% perovskite-like and 27% pyrochlore-like. In fact, Joseph Joly *et al.* [30] argued that, due to the ion size constraints, it is almost impossible to replace the trivalent La^{3+} ion by tetravalent ions in polycrystalline manganite bulks prepared by solid state reaction. Therefore, early study on

the Sn doped manganites all exhibited similar behaviors.

In addition to the bulk results mentioned above, some researchers prepared Sn doped manganites thin films on different substrates by PLD method. Guo *et al.* fabricated the La-Sn-Mn-O epitaxial films on $LaAlO_3$ substrates by PLD [91－94]. They reported the dependence of electrical transport and magnetic properties on the $La_{0.9}Sn_{0.1}MnO_{3-\delta}$ film thickness. The results revealed that the electrical transport, in contrast with the magnetic phase transition, was more sensitive to the thickness of the films. They also reported the properties $(La_{1-x}Sn_x)_y MnO_{3-\delta}$ and concluded that the tin in the films had the same effect as a divalent ion. They believed the kinetic nature of epitaxial films grown by PLD alters the perovskite $(La_{1-x}Sn_x)_y MnO_{3-\delta}$ films in which the tin doping has a divalent effect. Additionally, the spin-glass state has been observed in the $(La_{1-x}Sn_x)_y MnO_{3-\delta}$ films, and the magnetic inhomogeneity and the strain in the films were responsible for the spin-glass phenomenon. Besides, Gao *et al*. [95] had studied the structure, transport properties, and electronic structure of $La_{0.9}Sn_{0.1}MnO_3$ and $La_{0.9}Ca_{0.1}MnO_3$ films. According to their Hall-effect measurement, $La_{0.9}Sn_{0.1}MnO_3$ was *n*-type conductor in the metallic state. They also applied the x-ray photoelectron spectroscopy to demonstrate that the Sn ions were in the four-valence state in the LSMO films and therefore Mn ions in the $La_{0.9}Sn_{0.1}MnO_3$ was at a Mn^{2+}/Mn^{3+} mixed-valence state, which is significantly different from the divalent-element-doped manganese oxides since the $La_{0.9}(Ca, Sr)_{0.1}MnO_3$ both present ferromagnetic insulator behavior. The results also implied that the transport and magnetic mechanism of the hole-doped manganites could be different from that of the electron-doped manganites.

2.8 Discussion

The results introduced above revealed that all attempts to replace the tetra-valence ion into the La ion site frequently result in ferromagnetic-insulator CMR, suggesting either the lack of itinerant carriers or the exchange mechanism may be essentially different in the electron-doped regime. And it is still not clear that the electronic states of the doped ions indeed directly reflect the doping states of the CMR materials. Besides, owing to the lack of direct evidences of microstructure, as well as the data are usually confined within the probe profile range near the sample surface, it may obstruct the in depth understanding about the electron-doped manganites. Therefore, much work is needed to clarify this issue. In this dissertation, we present results obtained from the magneto-transport, electronic and microstructure analyses of the $La_{0.7}Sn_{0.3}MnO_3$ (LSnMO) that evidently clarify some of the interesting issues mentioned above.

Chapter 3

The magneto-transport properties of epitaxial $La_{0.7}Sn_{0.3}MnO_3$ manganite thin films grown on STO

In this chapter, we study the single-phase $La_{0.7}Sn_{0.3}MnO_3$ (LSnMO) thin films fabricated on $SrTiO_3$ (STO) substrates by pulsed laser deposition (PLD). The as-deposited films, though were insulating with no sign of insulator-metal transition (IMT), did display paramagnetic-ferromagnetic transition (PFT) around 170 K. *Ex-situ* annealing the films at 850 °C in 250 Torr oxygen for 4 h, nonetheless, not only significantly improves the crystallographic quality but also raises IMT and PFT to 315 K and 320 K, respectively. The manifestations of spin-glass-like behavior in both the as-deposited and post-annealed films suggest it could be intrinsic to LSnMO, albeit transport properties can be drastically changed by the strain originates from large ion-size misfit between Sn and La and film/substrate epitaxial relation. The preliminary x-ray absorption spectroscopy shows signature of Mn^{3+}/Mn^{2+} mixed-valence indicating that tetravalent Sn ions does result in electron-doping into the e_g band of Mn.
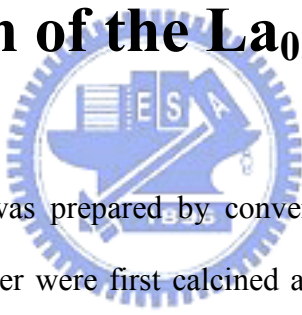
3.1 Introduction

The colossal magnetoresistance (CMR) effect and associated exotic physical properties exhibited in various hole-doped perovskite manganites have been subject of extensive researches [2－3]. On the other hand, due to the large size differences between the trivalent La^{3+} and tetravalent ions, it is generally very difficult to obtain single-phase electron-doped manganites by ionic substitution. In fact, Joseph Joly et al. [30] even argued that it is almost impossible to replace La^{3+} by tetravalent ions in polycrystalline manganite bulks. Indeed, early attempts in preparing Ce-doped RMnO$_3$ (R＝La, Pr, Nd) manganites by Das and Mandal [31] all showed signatures of mixed-phases and hence blurred the interpretation of the obtained results. In particular, it has been argued [32, 33] that the replacement of tetravalent ions to La^{3+} could lead to the self-doped $La_{1-x}MnO_{3-\delta}$ with localized multiphase compounds, which might give rise to very similar magneto-transport properties to those of the hole-doped manganites and jeopardize the genuine characteristics of electron-doping.

Recently, successful fabrication of single-phase electron-doped $La_{0.7}Ce_{0.3}MnO_3$ (LCeMO) thin films by pulsed laser deposition (PLD) has been demonstrated [71, 72], indicating that ionic constraints and stoichiometry conservation can both be compromised provided proper growth conditions were chosen [77]. Comparing to LCeMO, obtaining single-phase $La_xSn_{1-x}MnO_3$ encounters an even more severe challenge because of the larger ionic size misfit between La^{3+} and Sn^{4+}. Nevertheless, CMR effect has been reported in several $La_xSn_{1-x}MnO_3$ and Fe-doped $La_xSn_{1-x}MnO_3$ systems [91－92, 95], albeit the phases formed were still a matter of discussion [85] and only limited doping ($x = 0.04－0.2$) has been achieved in thin film form [91－92]. Since most manganites display optimum CMR effects at $x \approx 0.3$, it is desirable to extend the study of $La_xSn_{1-x}MnO_3$ to higher doping. Here, we report results of fabricating perovskite-like single-phase $La_{0.7}Sn_{0.3}MnO_3$ (LSnMO) films epitaxially

grown on $SrTiO_3$ (STO) substrates by PLD. Although, the as-deposited films were insulating, it was found that *ex-situ* post-deposition annealing not only raises the paramagnetic-ferromagnetic (PM-FM) transition temperature T_C from 175 K to over 320 K but also drives the films to display a typical insulating-metallic transition at $T_{IM} \approx 315$ K. The significant spin-glass-like behavior [96] observed in both as-deposited and annealed films indicate that the absence of insulator-metal transition in the as-deposited film is not due to spin-glass-induced effects [97]. Preliminary x-ray absorption spectroscopy (XAS) also indicates the presence of Mn^{2+}/Mn^{3+} signature, indicating the realization of electron-doping by Sn substitution.

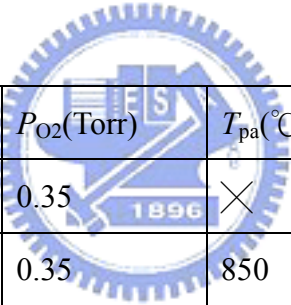# 3.2 Preparation of the $La_{0.7}Sn_{0.3}MnO_3$ target

Sintered LSnMO target was prepared by conventional solid-state reaction technique. Briefly, La_2O_3 and SnO_2 powder were first calcined at $800°C$ for 8 h. The calcined product was then mixed and ground with stoichiometric (with nominal $x = 0.3$) amount of $MnCO_3$ and sintered at $1200°C$ for 30 h. After repeating the grind-and-sinter process three times, it was pressed into pellet and sintered at $1200°C$ for 72 h.

3.3 The fabrication of $La_{0.7}Sn_{0.3}MnO_3$ thin films on $SrTiO_3$ substrate

LSnMO films with a typical thickness of about 200 nm were deposited on single crystalline STO(100) substrates using a 248 nm KrF excimer laser operating at energy density

of 2-3 J/cm^2 and repetition rate of 5-10 Hz. Figure 3.1 displays the schematics of the PLD system. In trying to obtain LSnMO films displaying CMR behavior *in-situ*, we had changed the substrate temperature (T_s) from 25 °C to 780 °C while keeping the oxygen partial pressure (PO$_2$) at 0.35 Torr. However, all the as-deposited films, though exhibited PM-FM transition at lower temperatures, were insulating and did not show metallic transition. Consequently, post-deposition *ex-situ* anneals were respectively carried out at 850°C and 800°C in 250 Torr oxygen for 25 min and 4h for films obtained at each T_s. The arrangement of post-annealed system is illustrated in figure 3.2, and the sample preparation conditions are listed in Table 3.1. The temperature dependences of magnetization (M(T)) and magneto-transport properties were measured using a Quantum Design® PPMS system with a maximum applied field strength of 8 Tesla.

Sample	T_s (℃)	P_{O2}(Torr)	T_{pa}(℃)	P_{02PA}(Torr)	t_{PA}
AD	780	0.35	✕	✕	✕
PA1	780	0.35	850	250	25 min
PA2	780	0.35	850	250	4 h

Table 3.1: Detailed prepareation conditions of the samples discussed in this study. T_s is the substrate temperature and P_{O2} is oxygen partial pressure in the deposition by PLD. T_{PA} is the annealed temperature, P_{02PA} is the annealed oxygen partial pressure and t_{PA} is the annealed duration time.
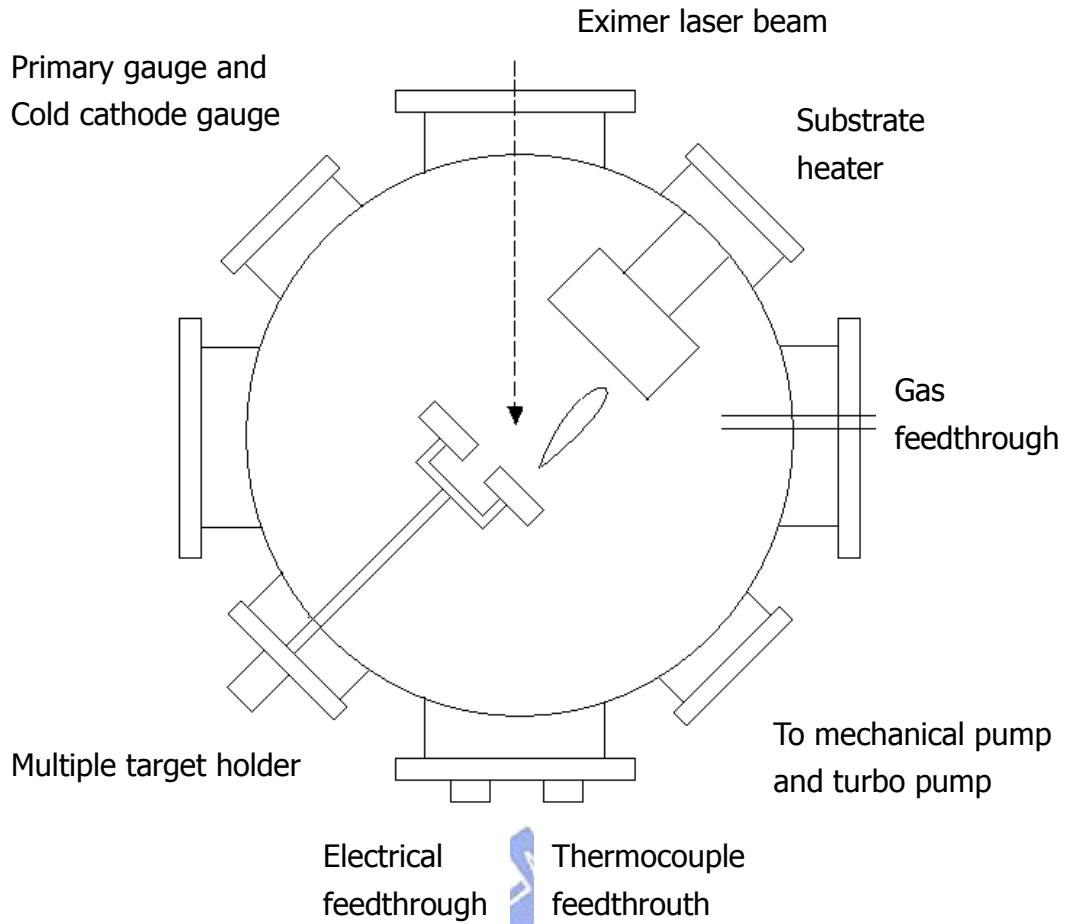
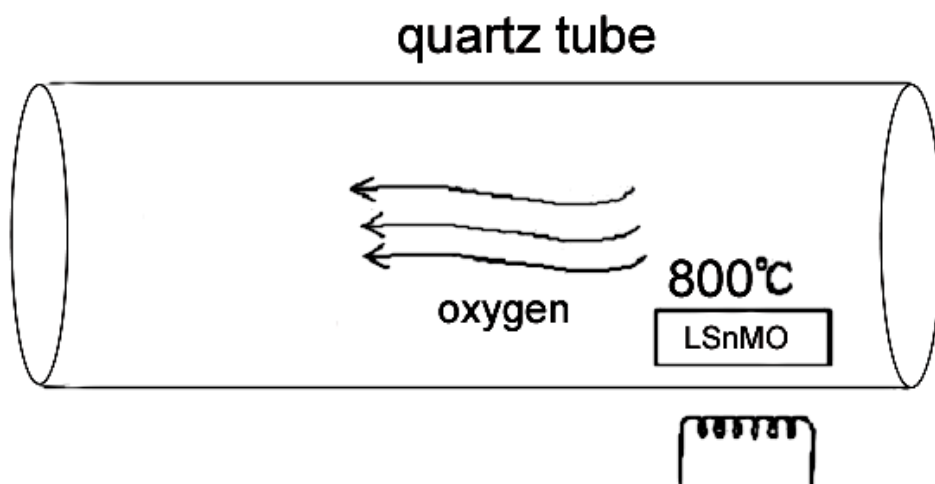Figure 3.1: Schematics of the pulsed-laser deposition (PLD) system.

Figure 3.2: Schematics of the post-annealed system.

3.4 The structure characterization

The energy dispersive x-ray analysis of both films shows an average composition ratio of La: Sn: Mn $=$ 0.756: 0.295:1 (normalized to Mn $=$ 1), as illustrated in Fig 3.3, in good agreement with the nominal stoichiometry of the target. Fig. 3.4 compares the x-ray diffraction (XRD) results of an as-deposited (AD) film obtained at T_s $=$ 780°C with that of a film deposited at the same T_s but *ex-situ* post-annealed at 850℃ for 25 min (referred as PA1 hereafter) and at 850℃ for 4 h (referred as PA2 hereafter). As is evident from the results, there are no observable impurity phases in AD, PA1 and PA2 films. For further clarification, L scan of AD, PA1 and PA2 films across (003) Bragg peak were performed, as displayed in Fig. 3.5. We note that similar peak-alignment was obtained for the AD-film, except that the peak width of the film is wider for the AD-film, presumably due to the extensive strain existent in the as-grown case. The slight split of the (00ℓ) peaks between the PA films and the substrates indicate that significant strain relaxation evolution may have occurred during annealing. In addition, as illustrated in Fig. 3.6, the x-ray scattering azimuthal-scans of the PA2-film across the STO (222) and LSnMO (222) Bragg peaks, clearly show very narrow peak width and good alignment between the peak positions, indicating high quality film crystallinity and the epitaxial relationship between the film and the substrate after prolonged annealing.
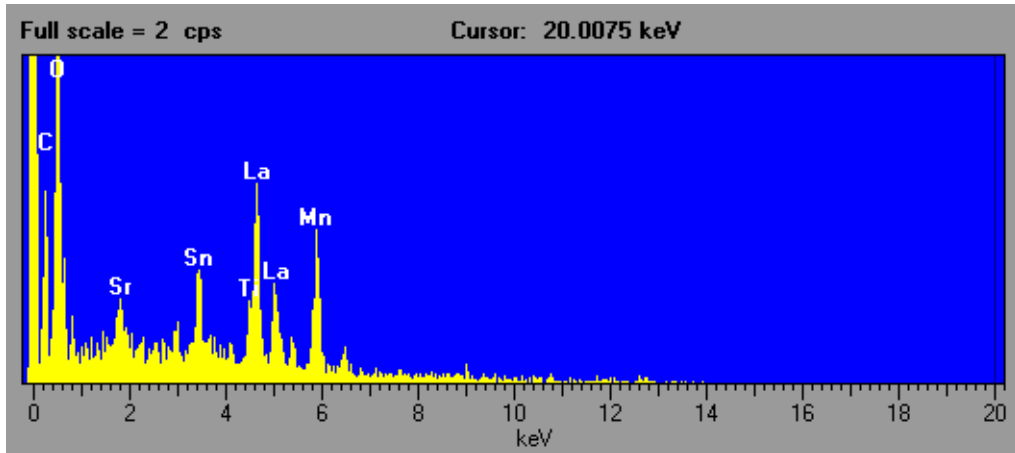
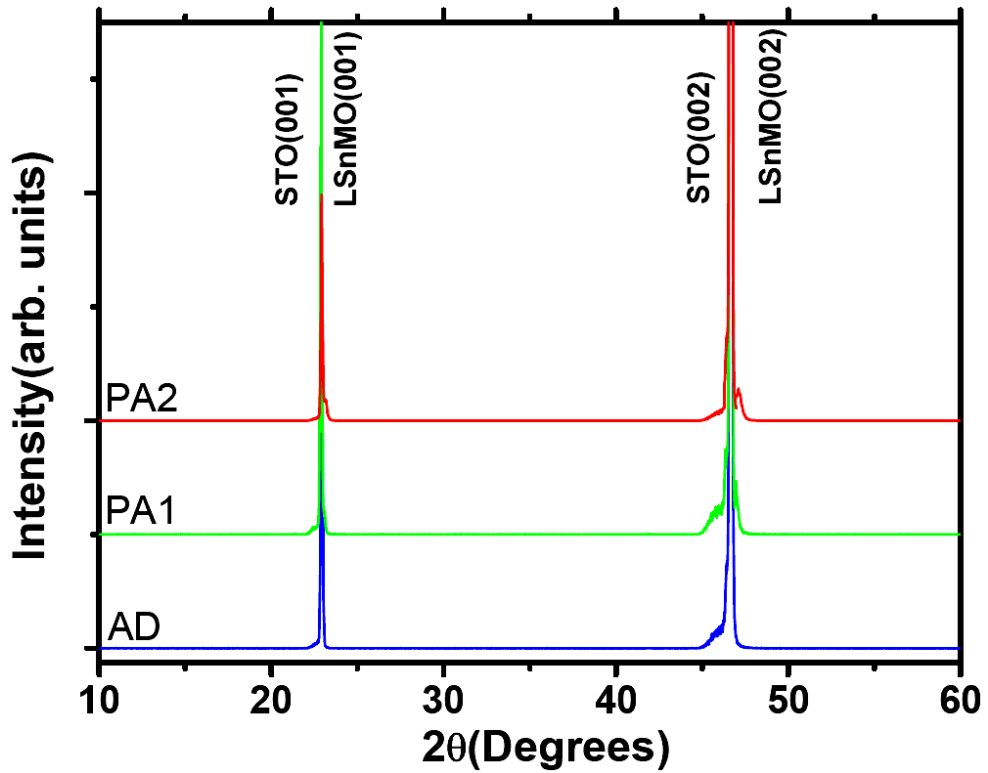Figure 3.3: The energy dispersive x-ray analysis (EDX) for AD film.

Figure 3.4: XRD results for the as-deposited, and post-annealed LSnMO films grown on STO substrate at $T_s = 780^{o}C$.
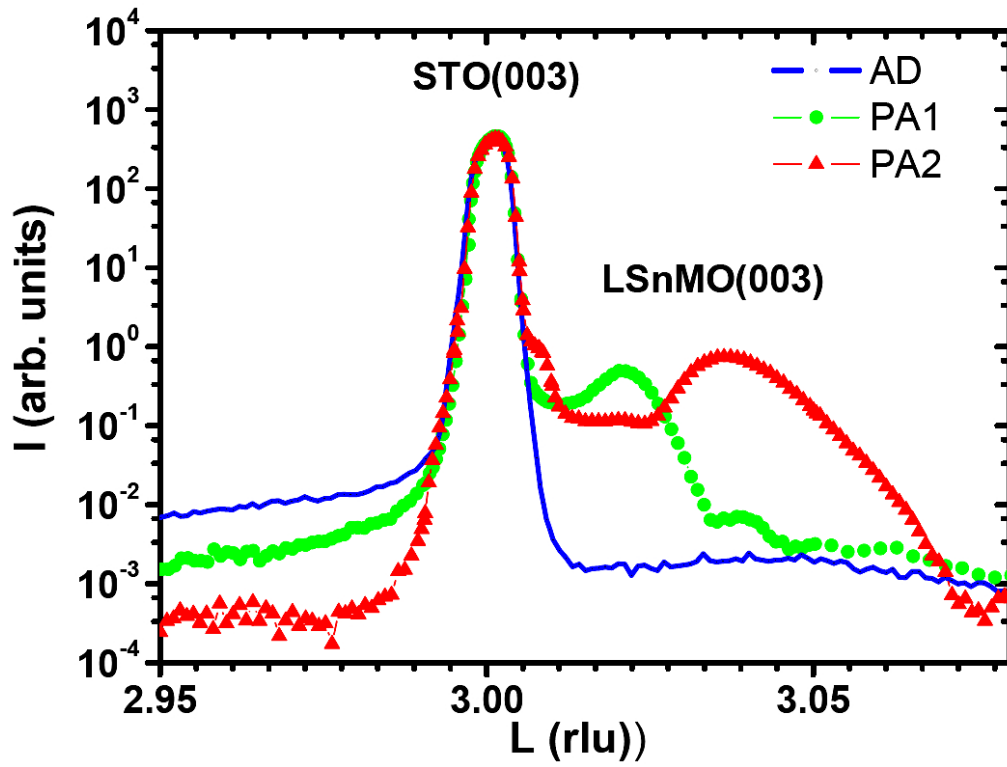
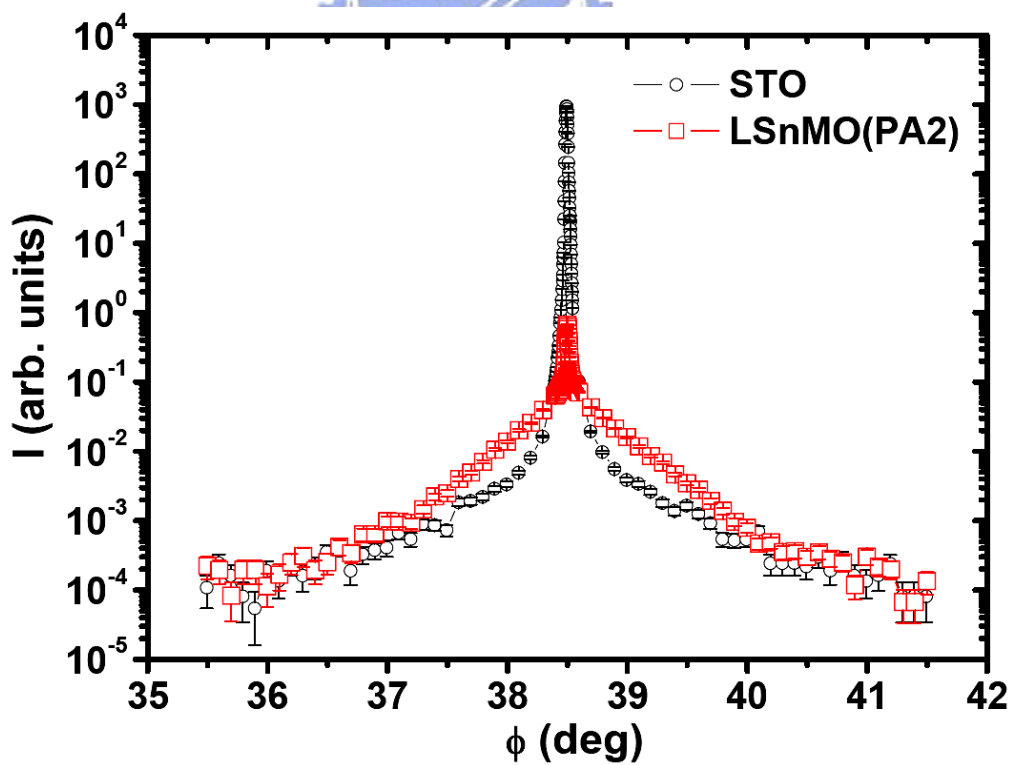Figure 3.5: L scan of AD, PA1 and PA2 films across (003) Bragg peak.

Figure 3.6: The Phi (azimuthal) scan across the STO (222) and LSMO (222) Bragg peaks, respectively.

3.5 The magnetic properties and electric transport

To give a further account on the present results, we first note that in the PM state the resistivity for the AD and PA2 films (Fig. 3.7 and 3.9) differs drastically, by nearly two orders of magnitude. While this can be attributed to charge localization effects associated with lattice distortion [98−99], the absence of a temperature-induced T_{IM} in the AD-film can be more subtle and complicated. De Teresa et al. [97] argued that it might be related to the absence of long range FM order signified with a manifestation of spin-glass behavior at lower temperatures. This would imply that the large epitaxial strain originally existent in the AD-film not only induces enormous charge localization effect but also hinders the formation of long range FM ordering. If this argument is true, one expects to see the opposites for the PA2-films. At the first glance, it seems to explain the over 200% enhancement in magnetization and dramatic increase in T_{IM} rather consistently. However, since the $M(T)$ data were measured under an applied field of 0.1T, the magnetizations of the samples are not yet saturated and cannot be used to estimate the saturated magnetic moment in the ferromagnetic state. Instead we estimate the saturation magnetization of AD- and PA-films by using the results obtained from the magnetization *vs* applied magnetic field (*M-H*) measurements. The estimated values for AD, PA1 and PA2 films are, in the unit of Bohr magnetons (μ_B), 1.34μ_B, 2.45μ_B and 3.54μ_B, respectively. Though the values are still significantly less than the expected value of 4 to 5μ_B for electron doped manganites, they nevertheless show an even pronounced enhancement in magnetization for PA-films as compared to that implied in the M(T) results taken at 0.1T.

Despite of these seemingly consistencies with the strain-induced suppression of long

range magnetic ordering suggested by De Teresa *et al.* [97], we note, however, as shown in Fig. 3.7－3.9, significant spin-glass behavior, characterized by the pronounced irreversibility between the field-cooled (FC) and zero-field-cooled (ZFC) M(T) curves, is evident for all three cases. This implies that the insulator-metal transition and spin-glass are not necessary mutually exclusive. Furthermore, Fig. 3.7－3.9 also reveal some features deviating from that reported for low-doping LSnMO [91]. In that progressive suppression of spin-glass-like behavior with increasing Sn-doping was observed and has been attributed to an increase of Mn^{4+} ions induced by La-vacancies resulted from Sn-doping. However, we suspect this scenario may not apply to our case. This is hinted firstly by the absence of impurity phase revealed by the XRD results and the stoichiometric composition of metallic ions observed. In addition, the 30% substitution of La by Sn would imply the existence of 90% Mn^{4+} ions [50], which will be well beyond the phase region exhibiting CMR effects in most manganites. Finally, we note that, in our case ($x=0.3$) the spin-glass transition not only emerges at much higher temperature ($T_g \approx 250$ K) than that reported in Ref. [97] (75 K $\rightarrow$ 20 K for $x=0.04\rightarrow$ 0.18) but also is very sensitive to the applied field. Apparently, the spin-glass behavior and CMR effect observed in the annealed LSnMO here is neither arising from Sn-doping-induced disorder [97] nor from the La-vacancy-induced divalent doping but is related to the strain relaxation in a more subtle manner. The other feature to be noted is the dramatic suppression of the low temperature magnetization for the AD-film when measured at 0.01 T. Since the basic ingredients for spin-glass to occur are disorder and magnetic interaction randomness plus anisotropy and frustration [96], it would be interesting to conduct further experiments to delineate the underlying physics responsible for these observations.

Fig. 3.10 shows ρ(T) as a function of applied field for the PA2-film. The resistivity was measured with the field applied parallel to the film surface. For the AD-film, although there exists typical PM-FM transition with $T_C \approx 175$ K, the ρ(T) increases steeply with decreasing temperature (Fig. 3.7) and has no sign of metallic transition for applied field up to 8 Tesla. On

the contrary, for the PA2-film, in addition to having a nearly two orders of magnitude reduction in resistivity as compared to the AD-film in PM state, it also displays the typical CMR behavior with $T_{IM} = 314$ K at zero-field. T_{IM} shifts to over 350 K at an applied field of 8 Tesla. The maximum magnetoresistance (MR) ratio, defined as $\Delta\rho/\rho = (\rho(0) - \rho(H))/\rho(0)$ with $\rho(0)$ and $\rho(H)$ being the resistivity at zero field and that at field H, respectively, appears around 300 K and reaches about 65% at a field of 8 Tesla. Combining with the $M(T)$ results shown in Fig. 3.7 and Fig. 3.9 for both the AD- and PA2-films, the results demonstrate that annealing not only changes the magneto-transport properties of the LSnMO films dramatically but also significantly enhances the magnetization by more than 200%. Guo et al. [91], by varying the film thickness in their $La_{0.9}Sn_{0.1}MnO_{3+\delta}$ films, have found similar enhancement in raising T_{IM} with increasing films thickness. However, there was no noticeable change in T_C and low temperature magnetization with film thickness variations, which led them to conclude that the enhancement of T_{IM} was due to strain relaxation instead of oxygen- or La-deficiency [37−38], [50, 54, 56, 61, 100]. Similarly, Thomas *et al.* [101] have attributed the improved magneto-transport properties observed in their high temperature (900°C) annealed $La_{0.7}Ca_{0.3}MnO_3$ films to the massive stress relaxation and improved crystallinity accompanied with grain growth. However, they did not give how magnetization and T_C changed with annealing. From the present results (Fig. 3.4−3.6), it appears that similar effects may have occurred in our case. The other possibility is that although post annealing can improve the film crystallinity, it may also simultaneously yield the La-deficient manganites [74]. In that case, the material will become hole-doping and one expects to see enhanced manifestation of Mn^{4+}.
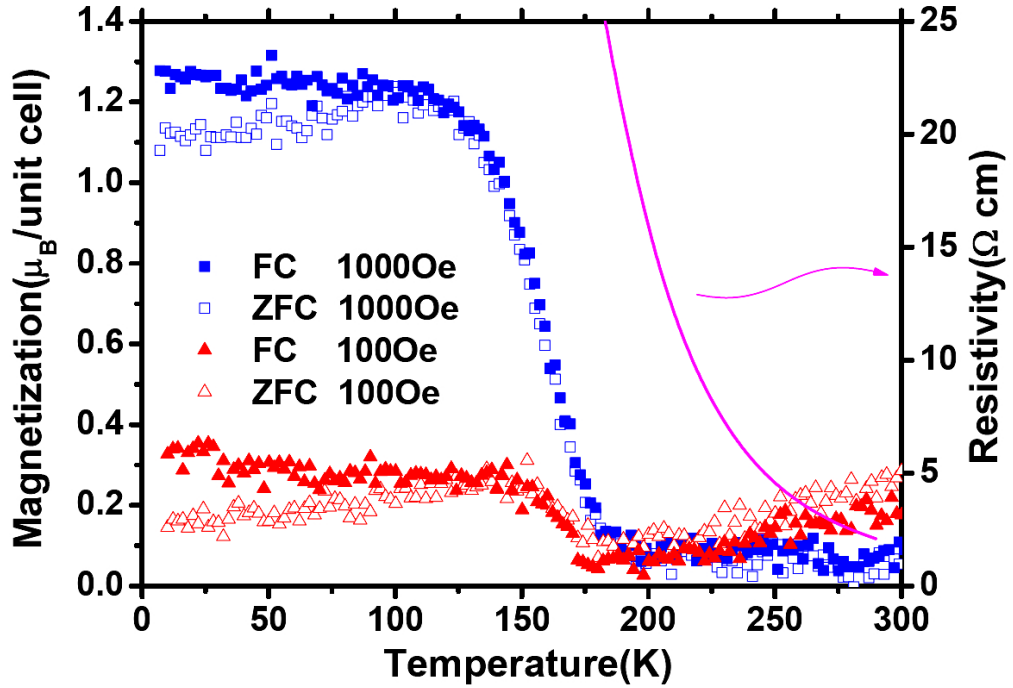
Figure 3.7: The field-cooled and zero-field-cooled temperature-dependent magnetizations measured at 0.1 T and 0.01 T for the as-deposited (AD) LSnMO film.
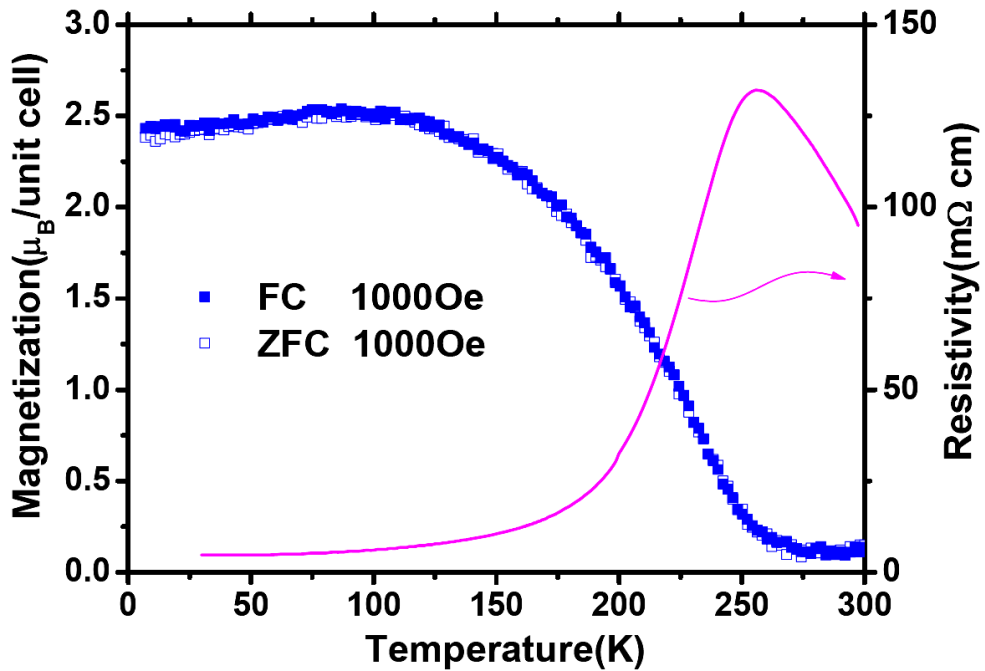

Figure 3.8: The field-cooled and zero-field-cooled temperature-dependent magnetizations measured under 0.1 T for the PA1 LSnMO film.
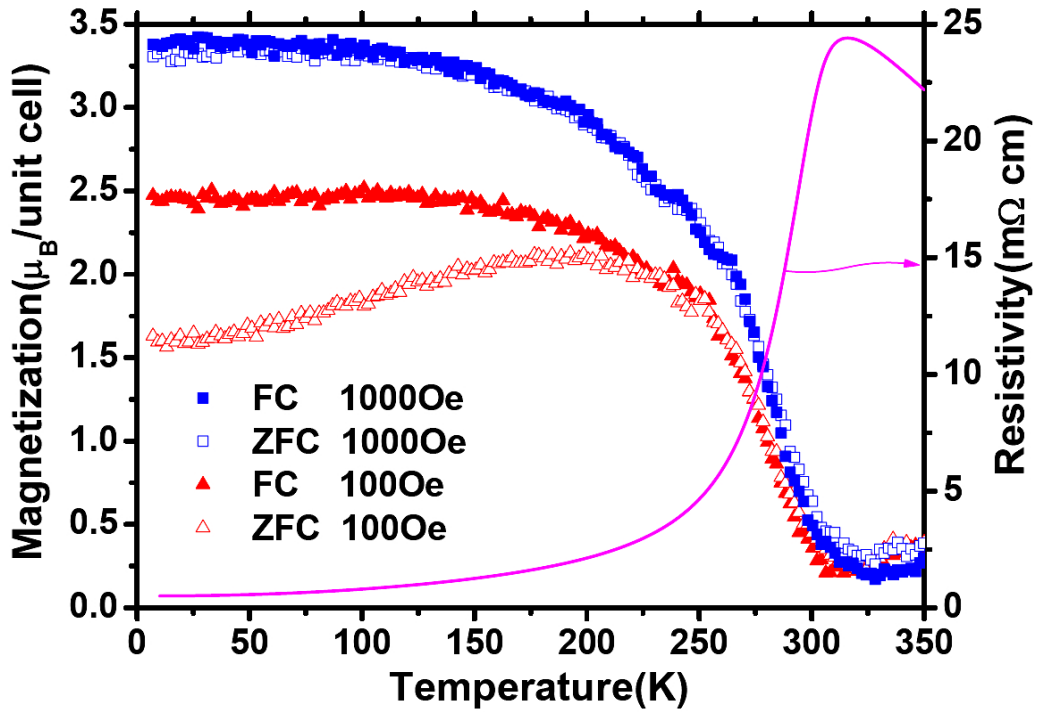
Figure 3.9: The field-cooled and zero-field-cooled temperature-dependent magnetizations measured at 0.1 T and 0.01 T for the PA2 LSnMO film.
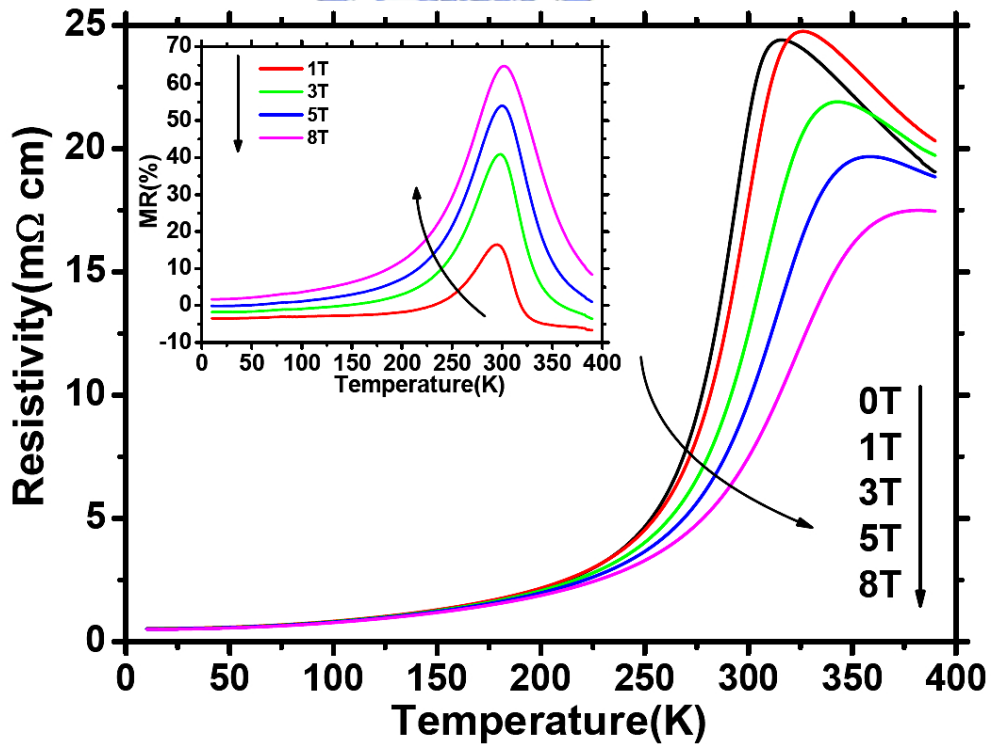

Figure 3.10: $\rho(T)$ as a function of applied field for the PA2 LSnMO film. The inset illustrates the field dependence of MR ratio. Notice that the maximum MR appears around the same temperature (~300K) for all fields.

3.6 The electronic structure

In order to check the effect of Sn-doping on the valence states of Mn ions, x-ray absorption spectra (XAS) measurements were performed at the National Synchrotron Radiation Research Center of Taiwan. As is evident from the results shown in Fig. 3.11, the spectra of Mn-$L_{2,3}$ demonstrate that the present samples indeed displays qualitative characteristics of Mn^{2+}/Mn^{3+} mixed valence state, indicating that Sn-doping does drive Mn^{3+} to Mn^{2+}. In particular, it is most discernible on the Mn-L_3 peak. As marked in Fig. 3.11, the peak position of Mn^{2+}, Mn^{3+}, and Mn^{4+} (obtained from the powder samples of MnO, Mn_2O_3, and MnO_2, respectively) locates at 640 eV, 641.8 eV, and 643.3 eV, respectively. On the other hand, the Mn-L_3 peak of LSnMO is situating between 640-642 eV and that of Mn_2O_3 is locating somewhere around 642-644 eV. It is evident that both the AD- and PA-films are indeed of Mn^{2+}/ Mn^{3+} mixing. On the other hand, for further discussion, the x-ray absorption spectra of Sn-M for LSnMO film are performed together with various reference compounds, as illustrated in Fig. 3.12. It is found that between 490-505eV there are four peaks for SnO_2 (Sn^{4+}) powder. There seem no obvious peaks for the SnS (Sn^{2+}) powder within this photon energy range. The data reveals that the AD LSnMO film presents different characteristic when comparing with PA1 and PA2 LSnMO films, as well as the SnO_2 and SnS powder. The XAS of AD LSnMO presents the hybridization of the Sn^{4+} within the perovskite structure. Nevertheless, the XAS of SnO_2, PA1 and PA2 are very similar suggesting that the valence of Sn in the samples PA1 and PA2 LSnMO are all 4+, at least under the probe length of the XAS (~100nm). The fact of the XAS analogy between PA1 (annealed 4h) and PA2 (annealed 25min) also implies that these annealed LSnMO films revealed the same electronic structure even though the samples were annealed for only 25min. From the results mentioned above, we believe that there are two possible scenarios for the case: one is the valence of Sn in the PA1 and PA2 LSnMO is all 4+

and the samples are all really electron doped manganites. The other case is that the PA1 and PA2 LSnMO are lanthanum deficiency manganites with the formation of SnO_2 clusters. As a result, the samples are all hole doped manganites. We also note that there is noticeable difference between the detailed spectra of AD- and PA-films. Whether or not it is arising from the strain-induced effects is not clear at present. Detailed analyses along this line, including O-XAS, are certainly needed to give a more quantitative account on the exact nature of these Sn-doped manganites.
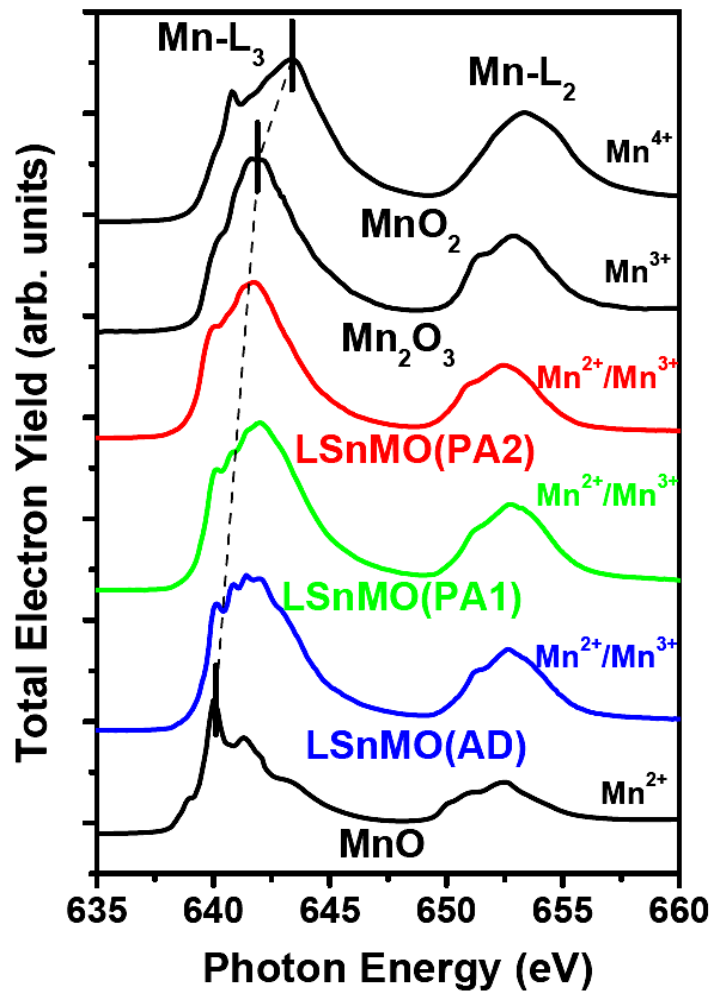

Figure 3.11: The x-ray absorption spectra of Mn-$L_{2,3}$ for LSnMO film and various reference compounds. Notice the evolution of the e_g-band peak as the valence of Mn ions changes from Mn^{4+}, Mn^{4+}/Mn^{3+}, Mn^{3+}, Mn^{3+}/Mn^{2+}, to Mn^{2+}, indicative of electron-doping resulted from the tetravalent Sn-substitutions.
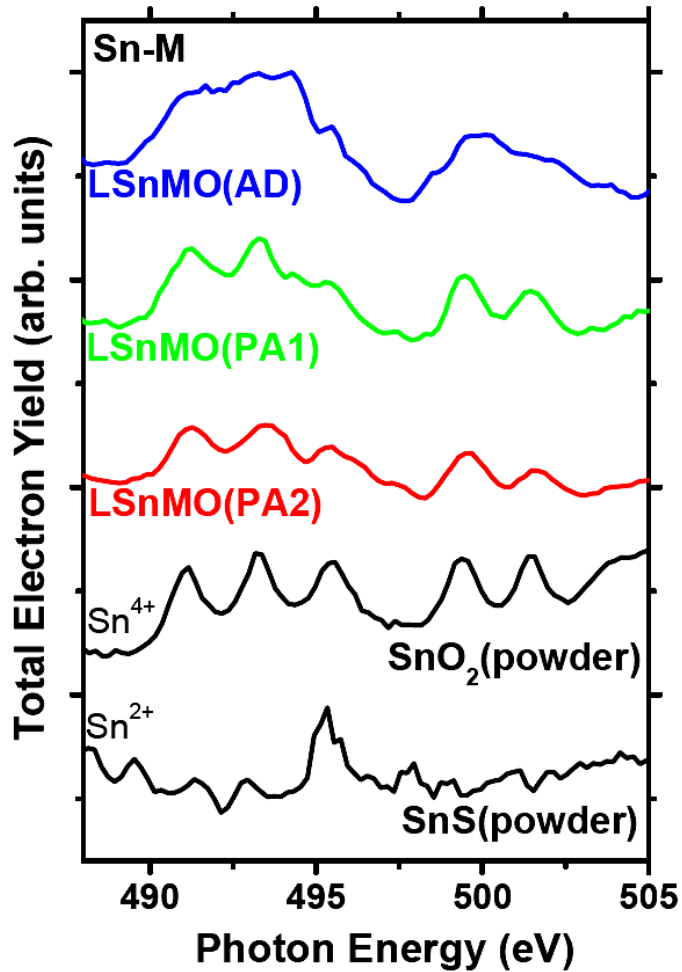
Figure 3.12: The x-ray absorption spectra of Sn-M for LSnMO film and various reference compounds.

3.7 Summary

In summary, we have successfully prepared single phase epitaxial $La_{0.7}Sn_{0.3}MnO_3$ films on $SrTiO_3$ substrates despite the tremendous challenges put forth by the large ionic size difference between La^{3+} and Sn^{4+}. The *ex-situ* post-deposition annealing not only improve the structure of AD-film and gives rise to epitaxial c-axis oriented LSnMO films but also leads to over room temperature CMR effects. Both the as deposited and post annealed LSnMO films display significant features of spin-glass that would need further studies for a fully

understanding. Preliminary Mn L-edge x-ray absorption spectroscopy analysis shows features of Mn^{3+}/Mn^{2+} mixed-valence states, indicating that the tetravalent Sn ions indeed results in electron-doping into e_g band of Mn.

Chapter 4

Magnetotransport properties, electronic structure, and microstructure of La$_{0.7}$Sn$_{0.3}$MnO$_3$ thin films grown on LAO
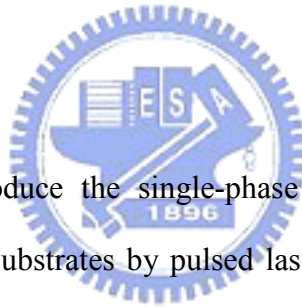
In this chapter, we introduce the single-phase La$_{0.7}$Sn$_{0.3}$MnO$_3$ (LSnMO) thin films fabricated on LaAlO$_3$ (LAO) substrates by pulsed laser deposition (PLD). The as-deposited films, though showed insulating characteristics with no sign of insulator-metal transition (IMT) down to very low temperatures, did display a paramagnetic-ferromagnetic transition (PFT) around 170 K. The x-ray absorption spectroscopy (XAS) of the as-deposited LSnMO films shows signature of Mn^{3+}/Mn^{2+} mixed-valence indicating that tetravalent Sn ions may have resulted in electron-doping into the e_g band of Mn. The transmission electron microscopy (TEM) analyses on the as-deposited LSnMO films further confirmed that the films are epitaxial with uniform composition distributions. It is suggestive that the doping level of $x=0.3$ in La$_{1-x}$Sn$_x$MnO$_3$ can be achieved without disrupting the perovskite structure or any composition inhomogeneity. On the other hand, *ex-situ* annealing in oxygen as well as in argon atmosphere, though both drive the films to display IMT and a marked enhancement in the transition temperature, the preservation of LSnMO phase is somewhat doubtful. In the

oxygen-annealing case, the evidence from the XAS measurements on Sn ions though showed the existence of tetravalent characteristics, the Hall measurements indicated that the obtained LSnMO films are p-type in nature. Furthermore, the TEM analyses also revealed the emergence of the Sn-compounds, which may ultimately drive the obtained films into La-deficient $La_{1-x}MnO_3$ phases.

4.1 The preparation of $La_{0.7}Sn_{0.3}MnO_3$ thin films on $LaAlO_3$ substrates

Sintered LSnMO target was prepared by conventional solid-state reaction technique. LSnMO films were deposited on single crystalline $LaAlO_3(100)$ substrates using a 248 nm KrF excimer laser operating at energy density of 2-3 J/cm^2. The details of the processing conditions can be found elsewhere [102]. The as-deposited films, though displayed usual paramagnetic-ferromagnetic transitions, the typical CMR behaviors of the accompanying insulator-metal transition was, however, absent. Thus, in some cases, subsequent *ex-situ* annealing was carried out at 800°C for 4 hours in 250 Torr of oxygen or argon. The temperature dependences of magnetization ($M(T)$) and magneto-transport properties were measured using a Quantum Design® PPMS system with a maximum applied field strength of 8 Tesla. The crystalline structure of the films was examined by x-ray diffraction (XRD) (θ-2θ scan) and x-ray scattering measurements. For the electronic structure and valence state of Mn and Sn ions, the x-ray absorption near edge spectroscopy (XANES) experiments were performed at the National Synchrotron Radiation Research Center of Taiwan. In order to probe the microstructure, interface between film and substrate, as well as the element

distributions of the LSnMO films, cross-section transmission electron microscopy (TEM) and electron energy loss spectroscopy (EELS) mapping were performed.

4.2 Transport and magnetic behaviors

Fig. 4.1 $-$ 4.3 shows the field-cooled and zero-field-cooled temperature-dependent magnetizations $M(T)$ measured at applied field of 0.1 T and 0.01 T together with the zero-field temperature dependence of resistivity $\rho(T)$ for Fig. 4.1 the as-deposited (AD) and Fig. 4.2 the oxygen-annealed (PA) LSnMO films as well as for Fig. 4.3 the argon-annealed (ArPA) LSnMO film measured at 0.1 T, respectively. We note that in the paramagnetic (PM) state the resistivity of the AD-film is larger than that of the PA-films by nearly two orders of magnitude. While this may originate from the charge localization effects associated with lattice distortion [98, 99], the absence of a temperature-induced T_{IM} in the AD-film can be more subtle and complicated. De Teresa *et al.* [97] argued that it might be related to the absence of long range FM order signified with a manifestation of spin-glass-like behavior at lower temperatures. This would imply that the large epitaxial strain originally existent in the AD-film not only induces enormous charge localization effect but also hinders the formation of long range FM ordering. If this argument is true, one expects to see the opposites for the PA-films. At the first glance, it seems to explain the over 200% enhancement in magnetization and dramatic increase in T_{IM} rather consistently. However, as shown in Fig. 4.1 $-$ 4.3, significant spin-glass-like behavior, characterized by the pronounced irreversibility between the field-cooled (FC) and zero-field-cooled (ZFC) $M(T)$ curves, is evident for both cases. This implies that the insulator-metal transition and spin-glass state are not necessary mutually exclusive. Furthermore, we note that the results shown in Fig. 4.1$-$4.3 also reveal some features deviating from that reported for low-doping LSnMO [92]. In that progressive

suppression of spin-glass-like behavior with increasing Sn-doping was observed. It has been interpreted as a result of increasing Mn^{4+} ions driven by Sn-doping-induced La-vacancies, and the low-doping LSnMO's were essentially regarded as hole-doped manganites. However, according to the XAS results to be presented below, the features of Mn^{2+}/Mn^{3+} mixed-valences indicate that the present AD-films might have effectively doped some electrons to the e_g-band of Mn-3d orbitals. Furthermore, we note that, in our case ($x = 0.3$) the spin-glass-like transition not only emerges at much higher temperature ($T_g \approx 150$ K) than that reported in Ref. 77 (75 K $\rightarrow$ 20 K for $x = 0.04 \rightarrow 0.18$) but also is very sensitive to the applied field. Thus, we suspect that the Sn-doping-induced La-vacancies scenario may not apply to our case. The spin-glass-like behavior and CMR effect observed in the annealed LSnMO here is probably not arising from the divalent doping-enhanced ferromagnetic interaction and magnetic homogeneity but maybe related to the strain relaxation in a subtler manner. The other feature to be noted is the dramatic suppression of the low temperature magnetization for the AD-film when measured at 0.01 T. Since the basic ingredients for spin-glass to occur are disorder as well as the magnetic interaction randomness, anisotropy and frustrations [96], we believe that these factors also account for the dramatic suppression of magnetization in the lower measuring fields for the AD-films. Finally, we note that very recent observations by Valencia et al. [103] have indicated that, in $La_{2/3}Ca_{1/3}MnO_3$ films, the formation of Mn^{2+} ions due to the instability of Mn^{3+} subjected to prolonged air exposure might also lead to charge localization and, hence, the increasing resistivity and reducing magnetization. However, the relevance of this non-ferromagnetic order originated from divalent Mn component to the observed spin-glass-like behaviors discussed above remains to be clarified.

On the other hand, since post annealing by argon is a common practice for preparing the tetravalent-doped CMR materials, it is important to clarify the effect of argon annealing on LSnMO films. The idea behind this practice was that the excessive oxygen may induce hole

doping, and thus, may counteract the expected effect of electron-doped CMR materials. Therefore, annealing in the argon environment may avoid the introduction of holes induced by excess oxygen and could turn out to be a practical method of fabricating electron-doped CMR materials. As illustrated in Fig. 4.3, the M-T of the argon-annealed LSnMO (ArPA LSnMO) film does display a comparable magnetization to that of the PA-LSnMO film. Nonetheless, the zero-field temperature dependent resistivity, $\rho(T)$, is about three times larger than that of the PA-LSnMO film. Since, in contrast to the AD films, both PA- and ArPA-LSnMO films exhibit signatures of typical paramagnetic-insulator (PI) to ferromagnetic-metal (FM) transition, annealing appears to have effects on driving the material from a ferromagnetic insulator to a ferromagnetic metal. However, there exist some differences in the detailed behaviors between the PA- and ArPA-films, as well.
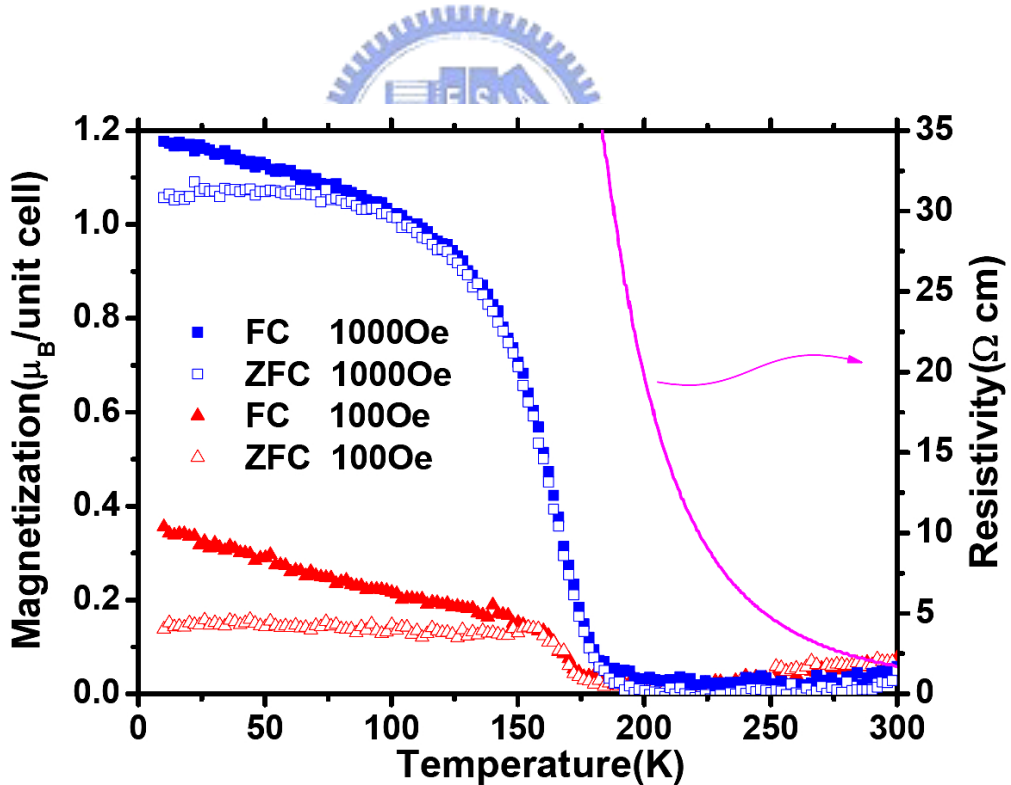

Figure 4.1: The field-cooled and zero-field-cooled temperature-dependent magnetizations ($M(T)$) measured at 0.1 T and 0.01 T for the as-deposited (AD) LSnMO film.
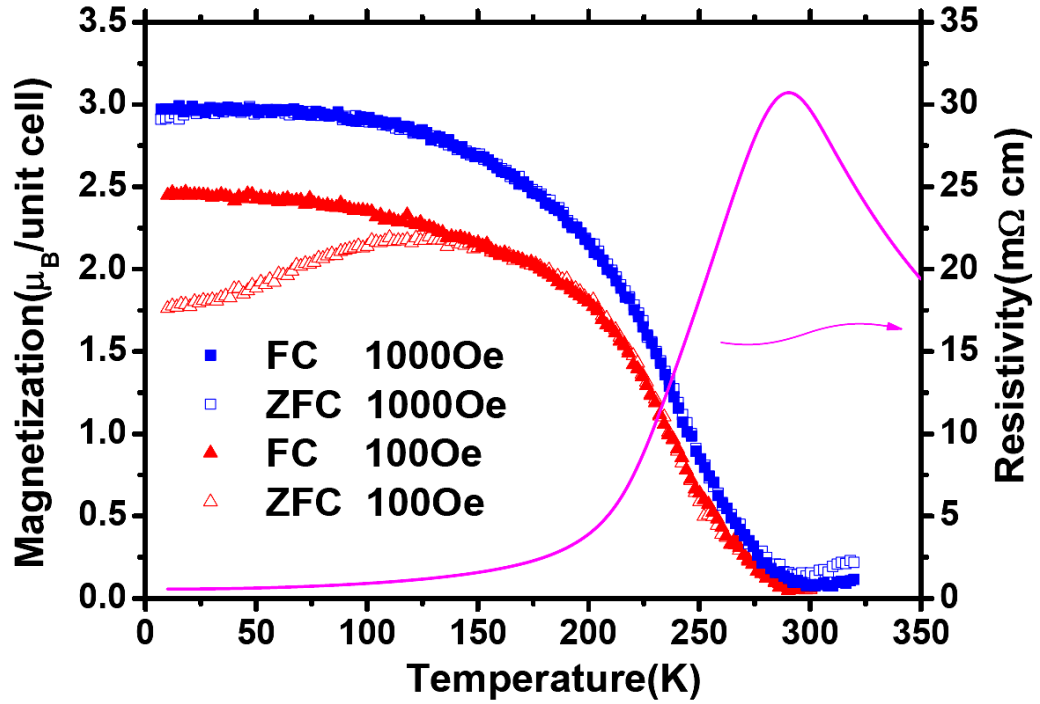
Figure 4.2: The field-cooled and zero-field-cooled temperature-dependent magnetizations ($M(T)$) measured at 0.1 T and 0.01 T for the oxygen-annealed (PA) LSnMO film.
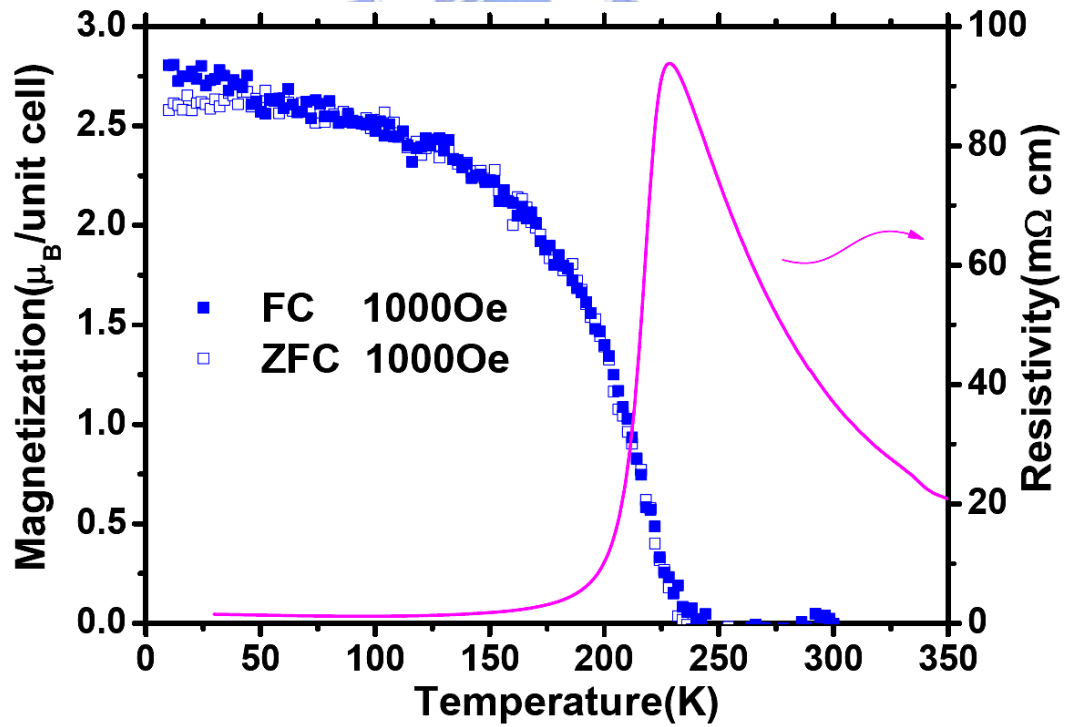

Figure 4.3: The field-cooled and zero-field-cooled temperature-dependent magnetizations ($M(T)$) measured at 0.1 T for the argon-annealed (ArPA) LSnMO film.

Fig. 4.4－4.5 shows $\rho(T)$ as a function of applied field for the PA film and ArPA film, respectively. The resistivity was measured with the field applied parallel to the film surface. For the AD-film, although there exists a typical PM-FM transition with $T_C \approx 190$ K, the $\rho(T)$ increases steeply with decreasing temperature (Fig. 4.1) and has no sign of metallic transition for applied field up to 8 Tesla. On the contrary, for the PA-film, in addition to having a nearly two orders of magnitude reduction in resistivity as compared to the AD-film in the PM state, it also displays the typical CMR behavior with $T_{IM} \sim 300$ K at zero-field. The maximum magnetoresistance (MR) ratio, defined as $\Delta\rho/\rho = (\rho(0) - \rho(H))/\rho(0)$ with $\rho(0)$ and $\rho(H)$ being the resistivity at zero field and at field H, appears around 250 K and reaches about 70% at a field of 8 Tesla. Together with the $M(T)$ results shown in Fig. 4.1－4.3, the results demonstrate that annealing not only significantly enhances the low-temperature magnetization by more than 200% but also changes the magneto-transport properties of the LSnMO films dramatically. Guo $et\ al$. [91], by varying the film thickness in their $La_{0.9}Sn_{0.1}MnO_{3+\delta}$ films, have found similar enhancement in raising T_{IM} with increasing film thickness. However, there was no noticeable change in T_C and low temperature magnetization with film thickness variations, which led them to conclude that the enhancement of T_{IM} was due to strain relaxation instead of formation of new phases introduced by oxygen- or La-deficiency [32－33, 50, 56, 52, 100, 103]. Similarly, Thomas $et\ al$. [101] have attributed the improved magneto-transport properties observed in their high temperature (900°C) annealed $La_{0.7}Ca_{0.3}MnO_3$ films to the massive stress relaxation and improved film crystallinity accompanied with grain growth. However, they did not report how magnetization and T_C were affected by post-annealing. In comparison, for the ArPA-films, although it also displays the typical CMR behavior, the $T_{IM} = 230$ K at zero-field is somewhat lower than that of the PA films. The maximum MR ratio appears around 220 K and reaches nearly about 95% at a field of 8 Tesla. These results are, in fact, very similar to that of some La-deficient CMR materials

[50, 97]. It appears that, from the magneto-transport properties alone, one cannot discern whether the typical CMR behaviors displayed by post-annealed films are indeed the genuine characteristics of electron-doped manganites or they are just manifestations of La-deficient manganites induced by post annealing [74]. In addition, whether the lack of insulating-metallic transition in AD-LSnMO films is correlated to the lattice disorder or to other mechanisms (such as composition change) remains to be clarified. In order to give some further accounts on these issues, we performed further investigations on the electronic structures of the corresponding films by XAS measurements.
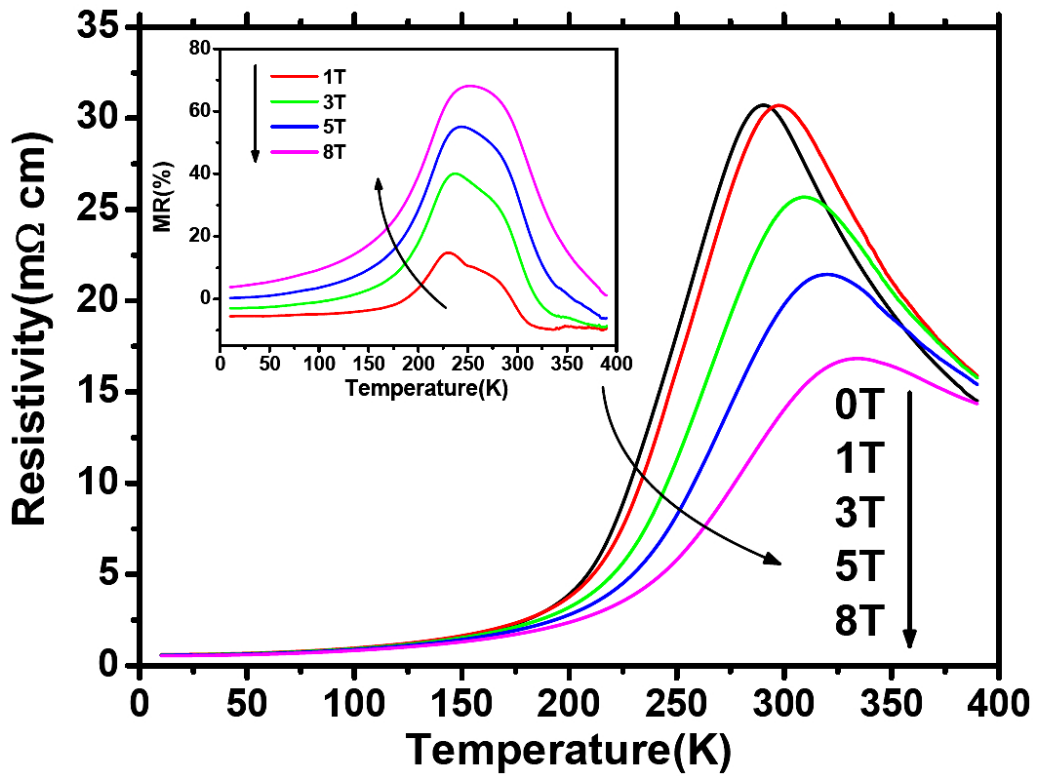

Figure 4.4: $\rho(T)$ as a function of applied field for the PA LSnMO film. The inset illustrates the field dependence of the MR ratio.
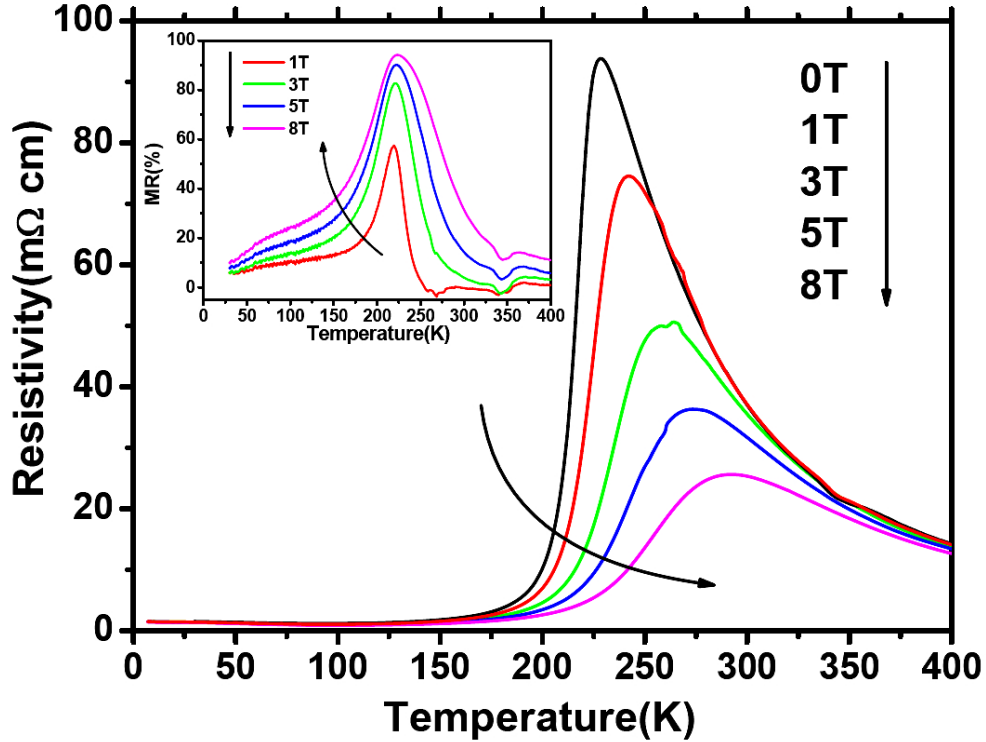
Figure 4.5: $\rho(T)$ as a function of applied field for the ArPA LSnMO film. The inset illustrates the field dependence of the MR ratio.

4.3 Electronic structure

Figure 4.6 shows the XAS results of Mn-$L_{2,3}$ for the AD-, PA-, and ArPA-films together with that of several "standard" powder samples. The results demonstrate that, while the AD-film indeed displays qualitative mixed-valence state characteristics of Mn^{2+}/Mn^{3+}, the valence state of Mn in the PA- and ArPA-films appears to be closer to that of the Mn^{3+}/Mn^{4+} mixed state. The manifestation of Mn^{2+} characteristic revealed in the XAS of the AD-film indicates that the PLD process, though may simultaneously introduce significant structural disorders, does help in retaining the Sn ions in the lattice. On the other hand, both the PA and ArPA processes appear to drive the LSnMO toward the hole-doped regime, except that there is signature of Mn^{2+} (the pre-edge peak around 640 eV) appearing for the AD. In order to

further delineate the possible difference between the electronic structure of PA and ArPA films implied in the magneto-transport results described above, we show, in Fig. 4.7, the XAS of Sn together with that obtained from the standard samples of SnO_2 and SnS powder. We first note that the results essentially dismiss the existence of Sn^{2+} ions in the LSnMO films, despite it has been anticipated that the ionic size of Sn^{2+} (0.96Å) seems to be more favorable than that of Sn^{4+} (0.81Å) in substituting the La^{3+} (1.13Å) ions in the perovskite structure [104]. The XAS data of Sn in the PA-LSnMO (oxygen-annealed) films qualitatively demonstrate the features obtained from the standard SnO_2 samples, indicating that majority of Sn ions are in the valence state of Sn^{4+}. In comparison, the XAS of Sn in the AD film displays a smeared characteristic of Sn^{4+} around the same energy range. This is indicative that the Sn ions are residing on the La-sites and are either affected by the size-mismatch-induced strain or even participating the hybridization between Mn-3d and O-2p orbitals, as in this case most of Sn ions are retained in the La-Sn-Mn-O films (*vide infra*). On the contrary, the XAS data of Sn in the Ar-annealed film do not show the signature of either Sn^{2+} or Sn^{4+}, suggesting that the doped Sn in the initial target material may have been largely missing in the ArPA LSnMO film, at least within the depth probed by the XAS. We, thus, suspect that the magneto-transport properties demonstrated previously might be the manifestations of some La-deficient manganite derived from the argon-annealed process. Besides, the unambiguous Sn^{4+} feature observed in the PA-LSnMO films suggests that either the valence of Sn in LSnMO is really 4+ or there is some SnO_2 or other tin-compounds formed in the LSnMO sample during the oxygen annealing process. Although the high T_C and high T_{IM} exhibited by these films have indicated that the latter is more likely the case, direct evidence is desirable to clarify this issue.
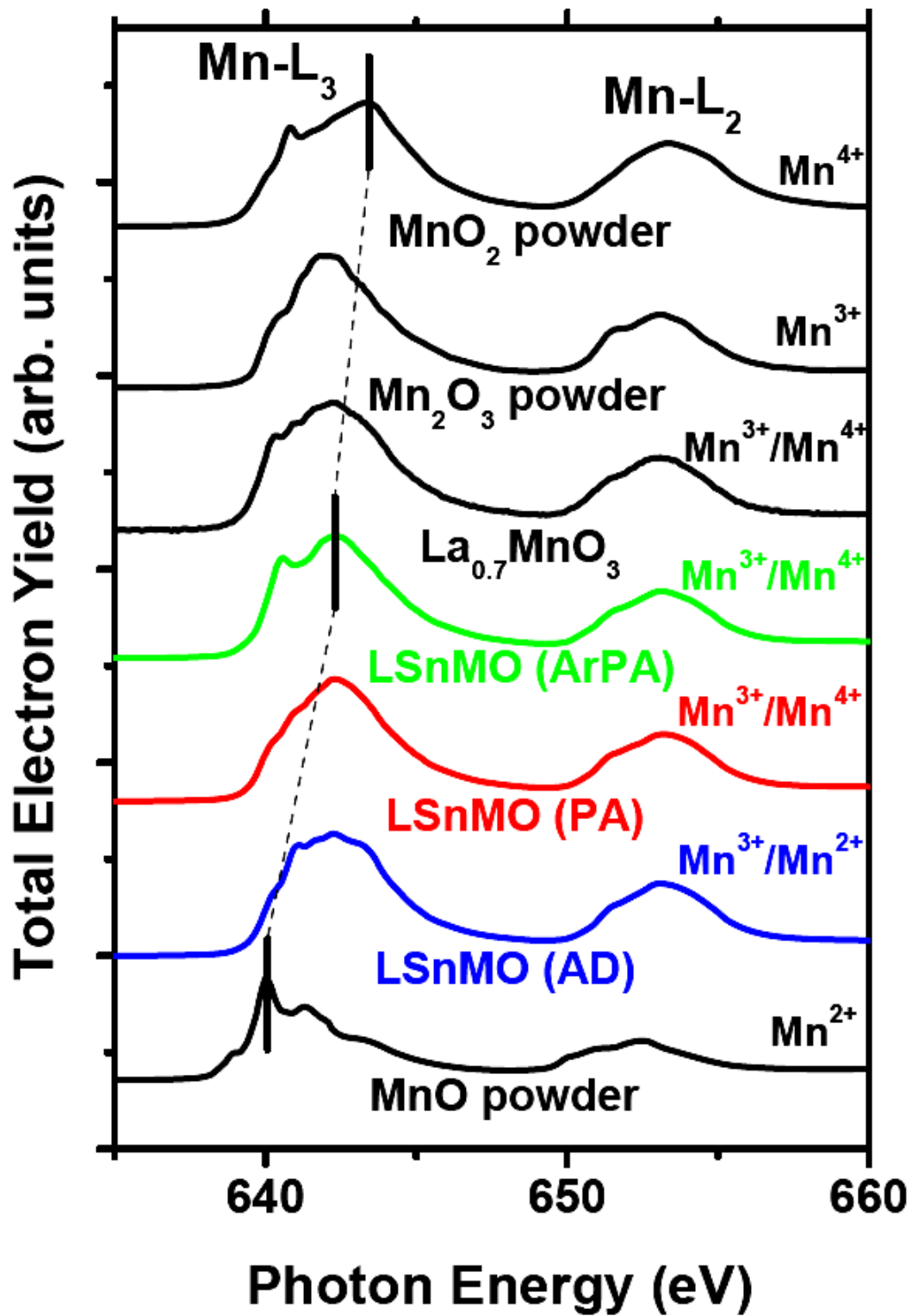
Figure 4.6: The x-ray absorption spectra of Mn-L$_{2,3}$ for LSnMO film. Spectra for various standard reference compounds are also displayed for comparison.
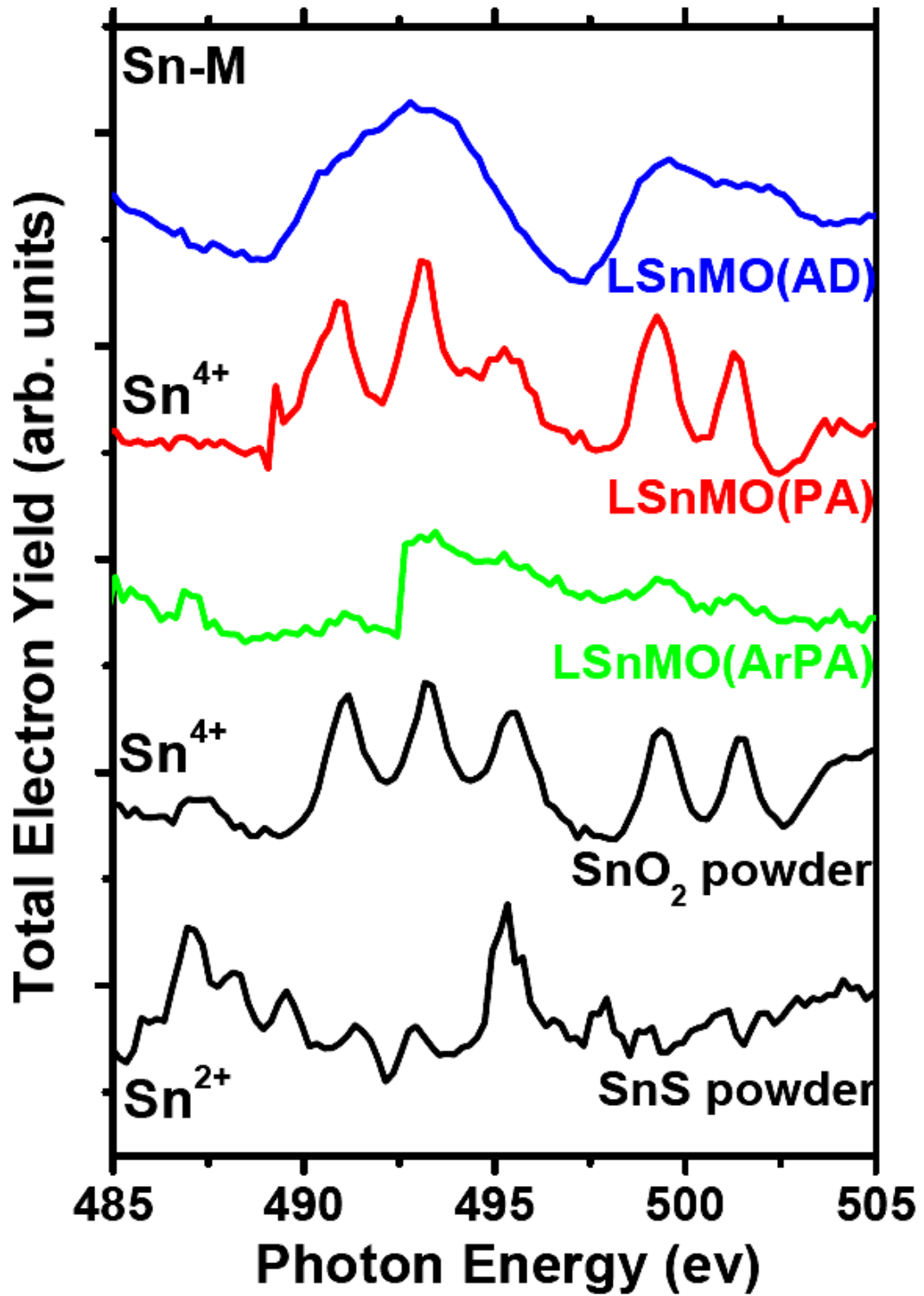
Figure 4.7: The x-ray absorption spectra of Sn-M for LSnMO film. Spectra for various standard reference compounds are also displayed for comparison.

4.4 Microstructure and constituents distribution analysis

The x-ray energy x-ray analysis for AD and PA LSnMO films are illustrated in Fig 4.8. It reveals there are no differences between these two samples, suggesting the amounts of the four elements (La, Sn, Mn, O) do not change after the post annealing process. Fig. 4.9 compares the $\theta-2\theta$ scan of x-ray diffraction (XRD) results for AD, ArPA and PA LSnMO films. It is evident from the results, all the films are c-axis oriented with no observable impurity phases. The slight split of the (00ℓ) peaks between the ArPA and PA-films and the substrates, however, indicates that significant strain relaxation may have occurred after prolonged annealing. To further delineate the possible subtle changes in the film microstructure due to annealing, L-scan and ϕ-scan measurements were performed. The typical results are illustrated in Fig. 4.10$-$4.12, respectively. In Fig. 4.10, it is evident that, in addition to the sharp Bragg peak from the LAO substrate, well-resolved (003)-reflection peaks of the LSnMO films were observed for the AD, ArPA, and PA samples with the correspondent c-axis lattice constant being 3.908Å, 3.893Å and 3.878 Å, respectively. Since the LSnMO film on LAO substrate is expected to experience an in-plane compressive stress due to the smaller substrate lattice constants, the progressive shortening of the c-axis lattice constant exhibited in the ArPA and PA films is indicative of the occurrence of annealing-induced strain relaxation, which in turn drives the film toward its bulk characteristics (The pseudocubic lattice parameter of $La_{1-x}MnO_3$ ranges from 0.3866 nm-0.3880 nm for $x = 0-0.33$ [100, 103]). We note that the in-plane lattice parameters also exhibited noticeable shrinkage upon annealing with a $=$ 3.913Å, 3.907Å and 3.900Å for AD, ArPA, and PA films, respectively. Valencia *et al*. [105] pointed out, in their study of

LCMO/STO films, that the existence of oxygen vacancies compensates the excessive elastic energy in coherently strained films. Thus, the shrinkage of the unit cell volume may reflect the elimination of oxygen vacancies and associated strain energy. The full width at the half maximum (FWHM) of the azimuth L-scan across the {0 −1 3} peak of AD-LSnMO is about 4.4°, which is much larger than that of LAO (103) (0.1°). This can be due to either the strain or fine grain size effects. The in-plane grain size estimated from the line width of L-scan across the LSnMO (0 −1 3) reflection is approximately 100 Å. On the other hand, for the PA film, the FWHM of LSnMO (103) is about 1.9°, which, though still much larger than that of LAO (103) (~0.036°), is significantly smaller than that observed in AD-film. The in-plane grain size as estimated from the line width of the H-scan across the LSnMO (103) reflection is approximately 135Å. This difference strongly suggests the crystallinity of LSnMO films was significantly improved upon annealing while the in-plane epitaxial relationship remains largely intact. The φ-scans were taken across the {0 −1 3} Bragg peaks of the LAO substrate and LSnMO films. It is evident from Figs. 4.11 and 4.12, both AD- and PA-LSnMO films display well-aligned ab-plane epitaxy with the LAO substrate. Again, the FWHM of the diffraction peaks for the AD-film is larger than that of the PA-film consistent with the arguments aforementioned for the XRD results.
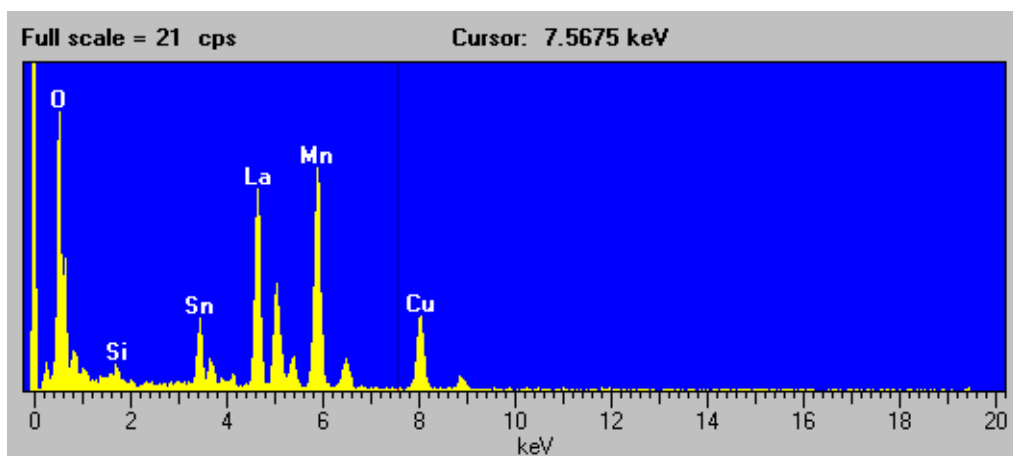

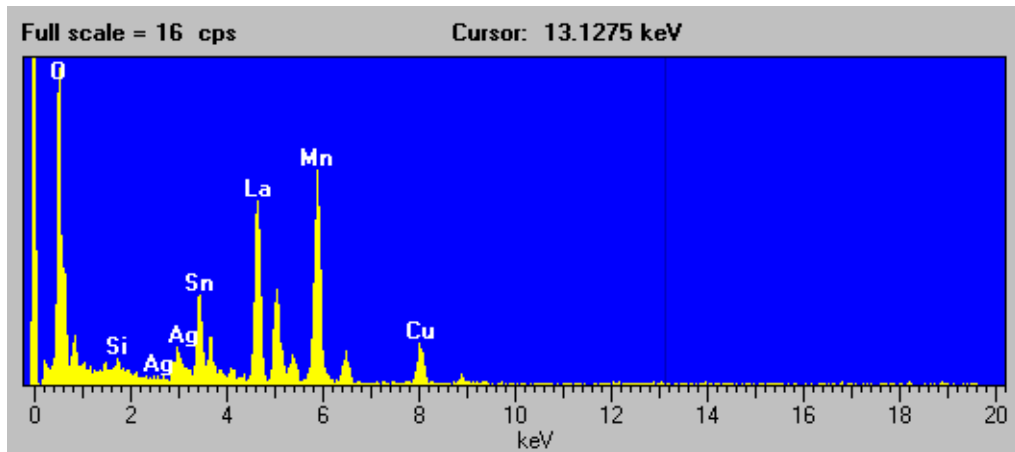Figure 4.8 (a): The energy dispersive x-ray analysis (EDX) for AD LSnMO film.

Figure 4.8 (b): The energy dispersive x-ray analysis (EDX) for PA LSnMO film.
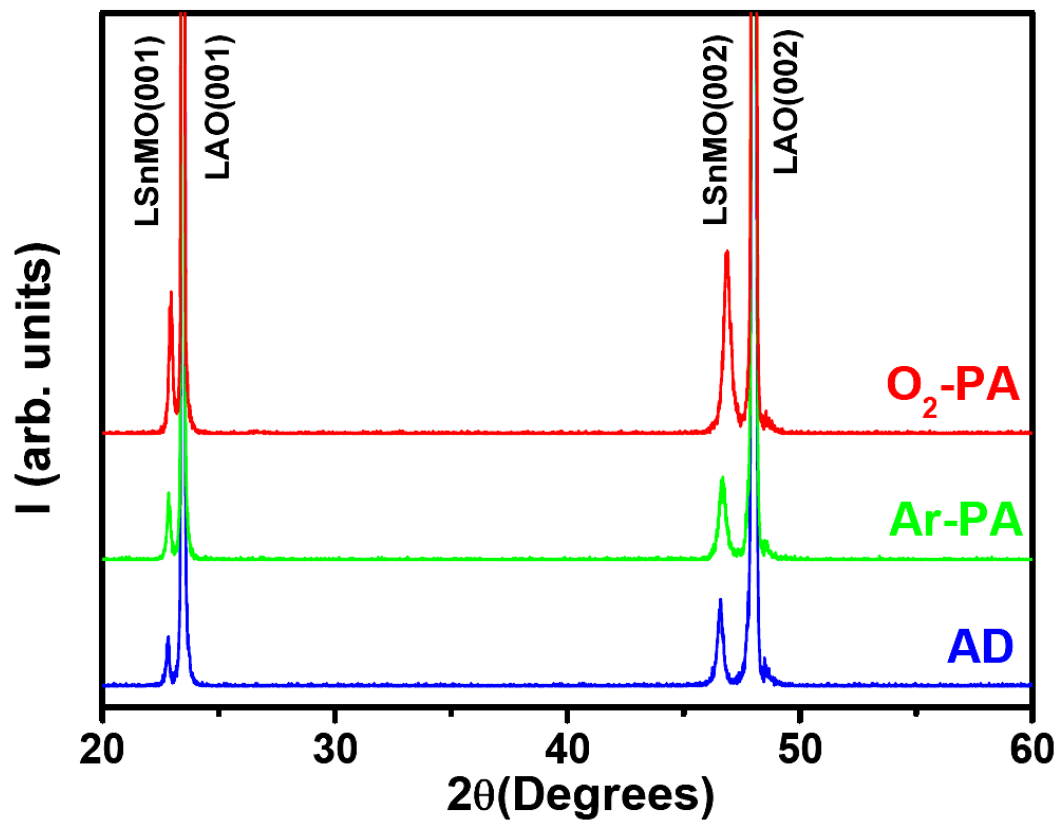

Figure 4.9: XRD results for the as-deposited, Ar-annealed and post-annealed LSnMO films grown on LAO substrates at $T_s = 780^oC$.
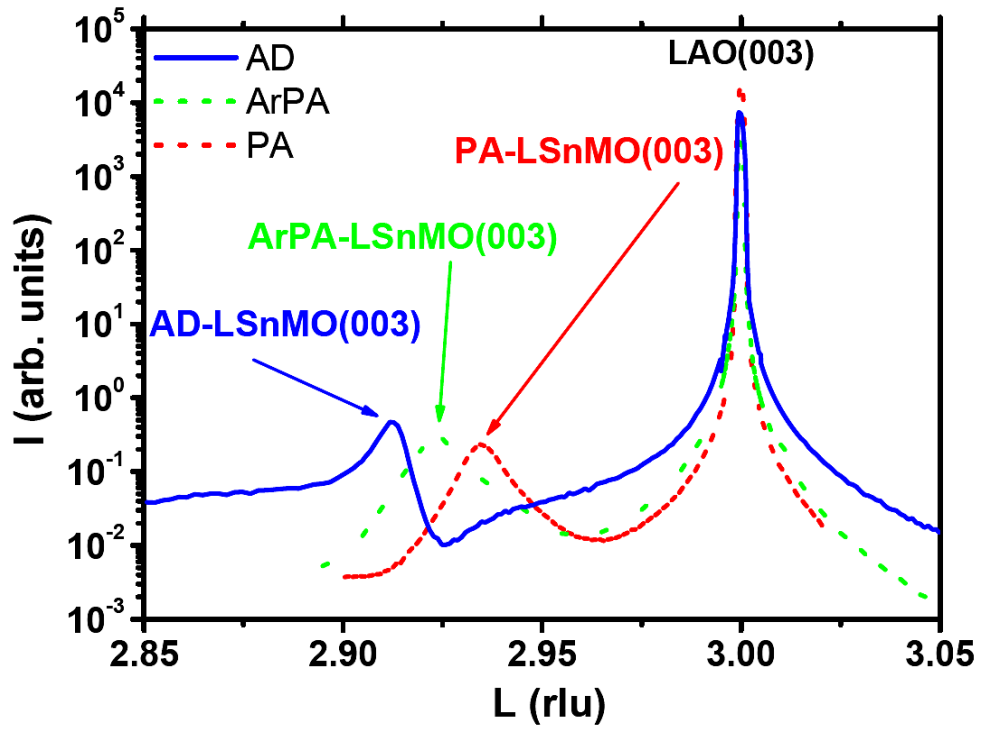
Figure 4.10: L-scan of AD, ArPA and PA films across (003) Bragg peak.
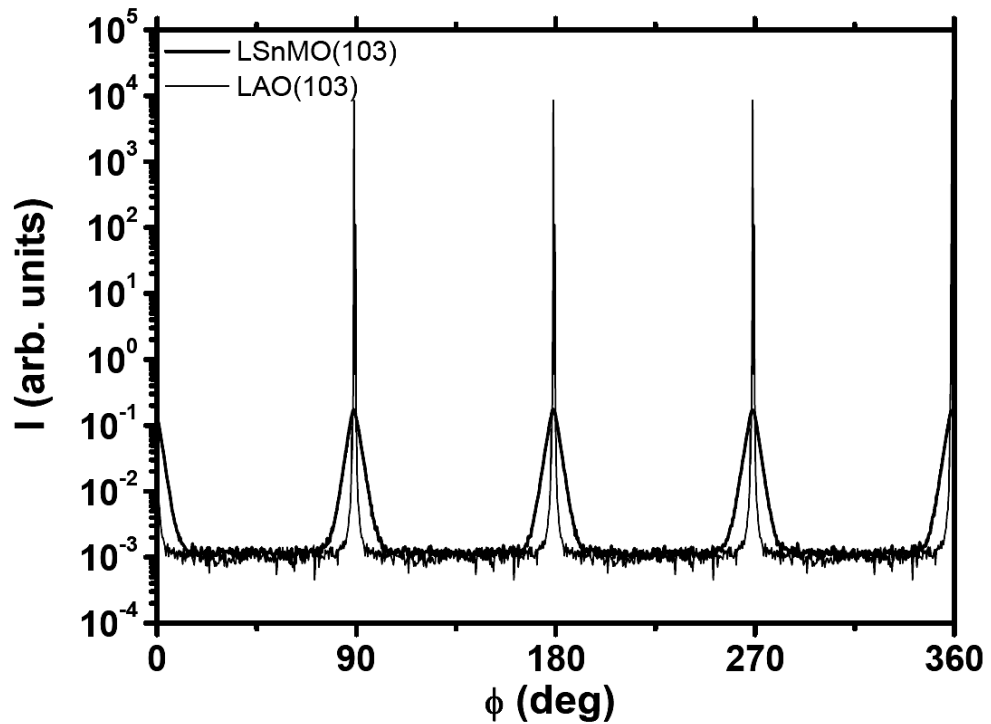

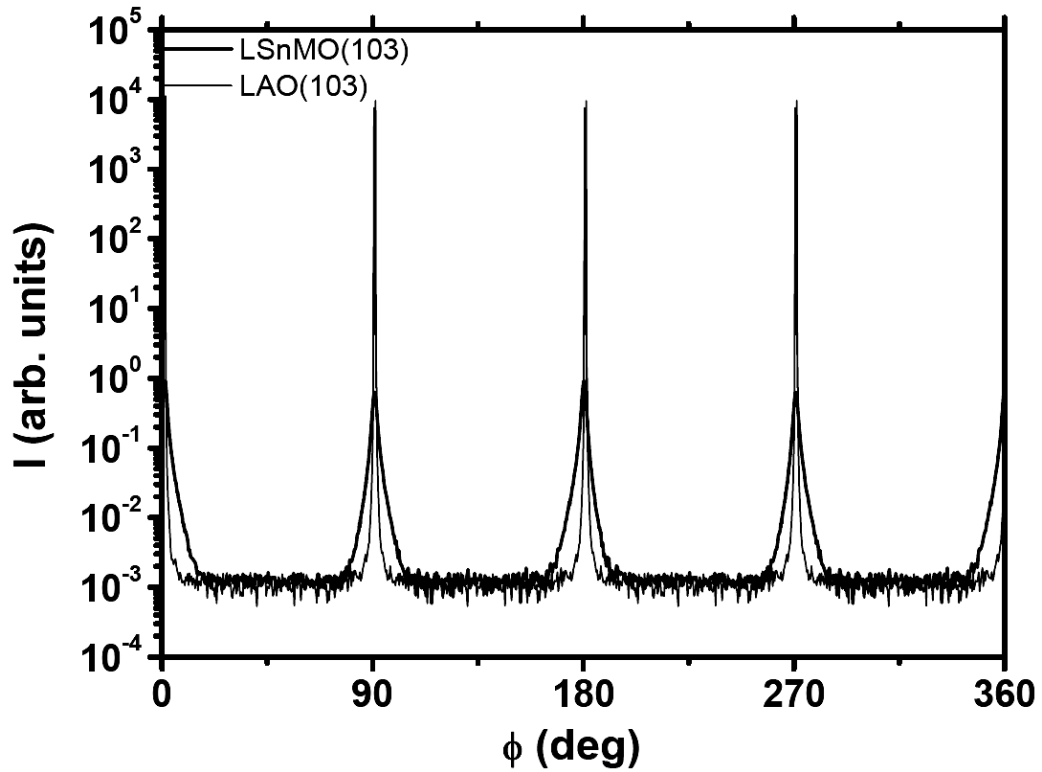Figure 4.11: The ϕ-scans for the LAO (103) and AD LSnMO (103) Bragg peaks, respectively.

Figure 4.12: The φ-scans for the LAO (103) and PA LSnMO (103) Bragg peaks, respectively.

To further delineate the evolving film/substrate relations due to annealing, Fig. 4.13−

4.15 illustrate the reciprocal space maps of AD-, ArPA- and PA-LSnMO films. The decreasing

peak position offset in $q_{\parallel}$ between LAO and LSnMO in the reciprocal space maps clearly

shows the occurrence of strain relaxation effect after annealing process. It is also evident that

the lattice constants of LSnMO are significantly larger than that of LAO, consistent with the

abovementioned results. For comparison, we show, in Fig. 4.16, the similar plot obtained for

the PA LSnMO/STO (001). Since the lattice constant of LSnMO falls between STO and LAO

and is closer to that of STO, LSnMO grown epitaxially on STO and LAO would experience a

tensile/compressive average in-plane strain, respectively. In the case of LSnMO/STO, the

films are fully coherent to the substrate, as indicated by the nearly perfect alignment between

the center of the STO(113) and LSnMO(113) peak contours. Nevertheless, in both bases, we

observe shrinkage of both the *c*-axis lattice constant and unit cell volume of LSnMO upon post-annealing; in LSnMO/STO case, *a-b* remains invariant but in the case of LSnMO/LAO, *a-b* also decreases slightly. It appears that some of the strain, originally compensated by oxygen vacancy incorporation [105], was released through the reduction of average unit cell volume. Alternatively, it is also possible that the change of average lattice parameters upon PA is coupled with change of composition, or even second-phase segregations. In any case, the lattice constant change associated relaxation of the mismatch in the films, though might originate from very different mechanisms, do intimately correlate to the enhanced CMR properties in a consistent manner. Unfortunately, the x-ray analyses seemed inadequate to precisely answer the question about the role played by Sn.
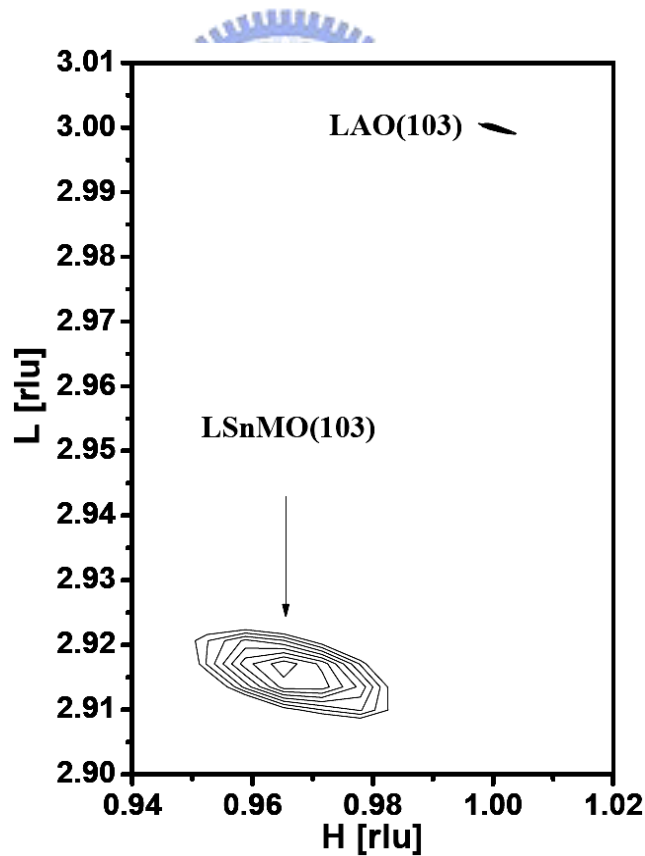

Figure 4.13: Reciprocal space maps of AD LSnMO films grown on LAO substrate.
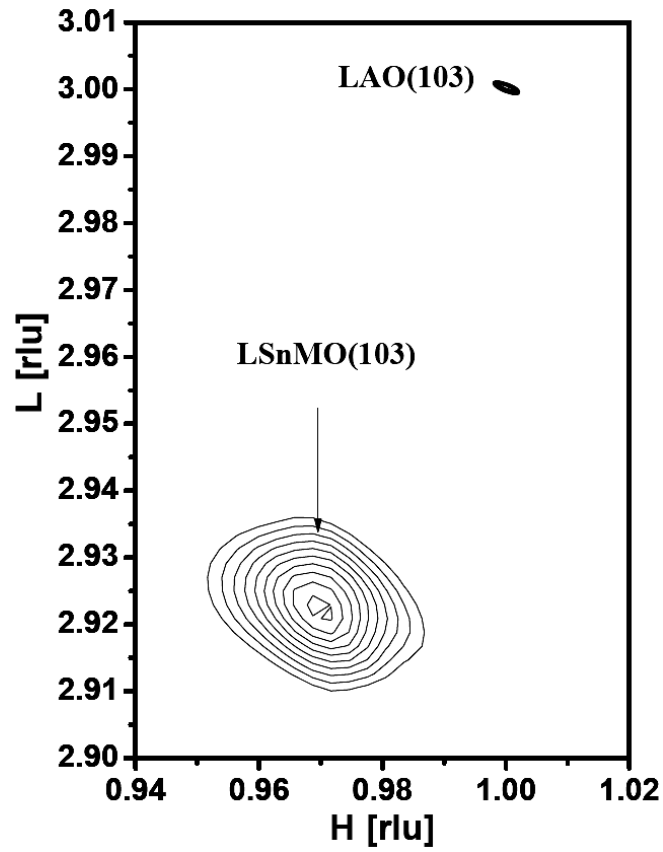
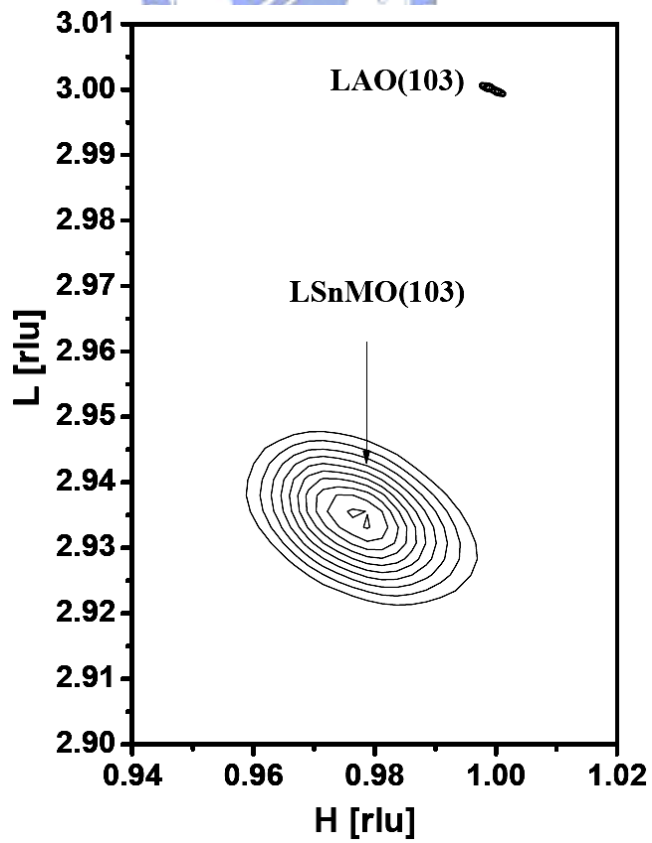Figure 4.14: Reciprocal space maps of ArPA LSnMO films grown on LAO substrate.

Figure 4.15: Reciprocal space maps of PA LSnMO films grown on LAO substrate.
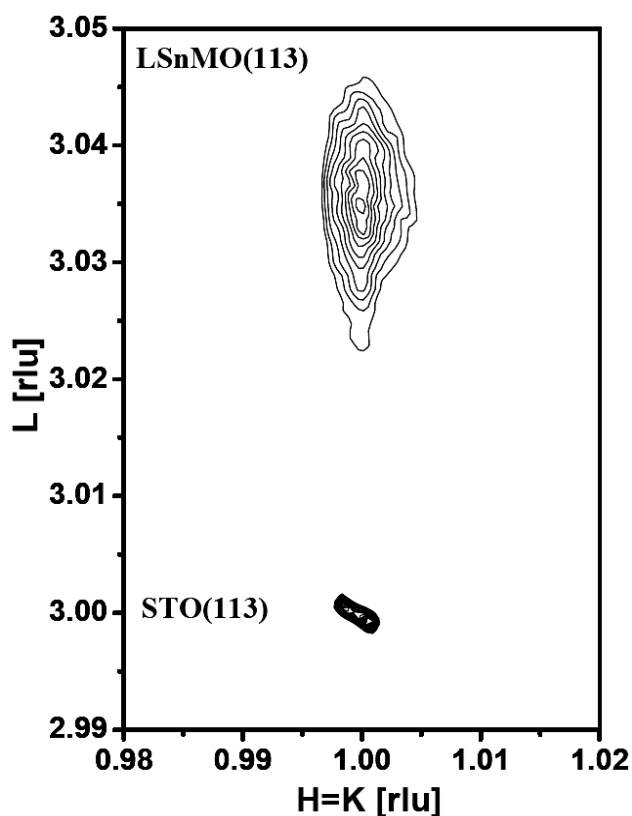
Figure 4.16: Reciprocal space map of PA LSnMO film grown on STO substrate.

In order to further examine the distribution of Sn and the possibly formed Sn-compounds that are not discernable by using x-ray diffraction alone, we performed the cross-sectional transmission electron microscopy (X-TEM) analyses to reveal the microstructure and the element distribution of the LSnMO films. Figures 4.17 and 4.18 show the bright-field TEM images and selective area diffraction (SAD) pattern of AD LSnMO(001) film grown on LAO(001) substrate. As can be seen from Fig. 4.17, the film's microstructure appears to be rather homogeneous and there is no trace of any additional compound existing within the interface of film and substrate. In addition, the absence of extra diffraction spots in Fig. 4.18 indicates that the AD-LSnMO film grown on LAO substrate is indeed single phase with well-organized epitaxial relations. The rod-like diffraction spots and the streaky patterns appeared in the columnar grains of the LSnMO phase suggest that there exists a significant

amount of strain in the film. We believe that both the slight lattice mismatch between the film and substrate and the large ionic size difference between La^{3+} and Sn^{4+} may contribute. For the PA-LSnMO film, however, the results are quite different. Fig. 4.19 and Fig. 4.20 show the bright-field TEM images and SAD pattern of PA LSnMO(001) film grown on LAO(001) substrate. The bright field image apparently displays two somewhat separated regions. The grains in the near surface upper region appear to be more "equi-axial" with much less strain-induced streaky patterns, suggesting significant recrystallization may have occurred due to annealing. In the "lower" region (region close to the substrate interface) the features are more like that observed in the AD-film. Although it is still not obvious to conclude whether or not the recrystallized upper region containing any newly formed phases from the SAD results, it is, nevertheless, interesting to find that the oxygen annealing affects only the upper part of the film. With the about 4 hours of annealing time and 100 nm of the affected depth, the estimated oxygen diffusion rate at 800 °C is about 25 nm/hr.
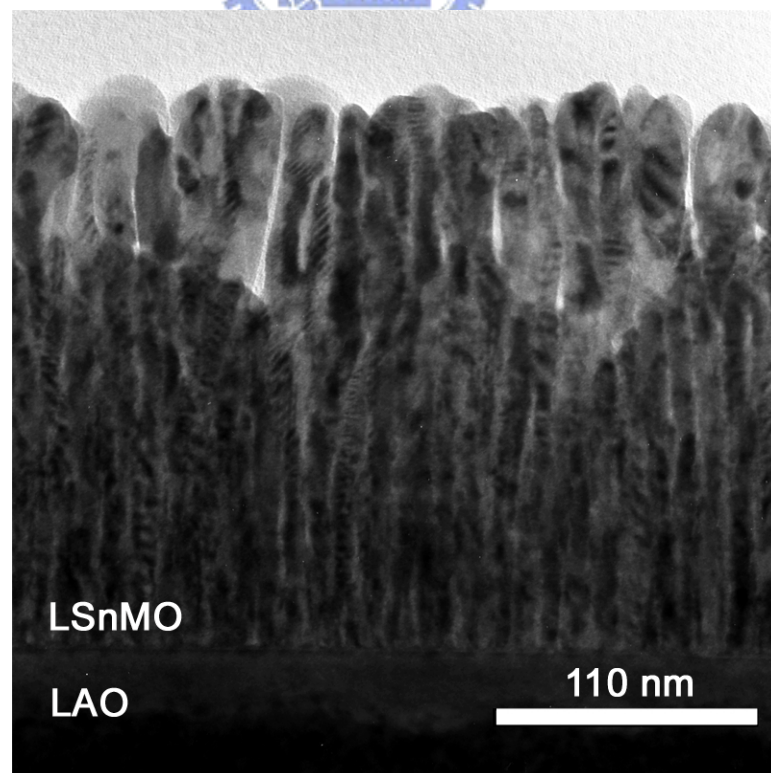

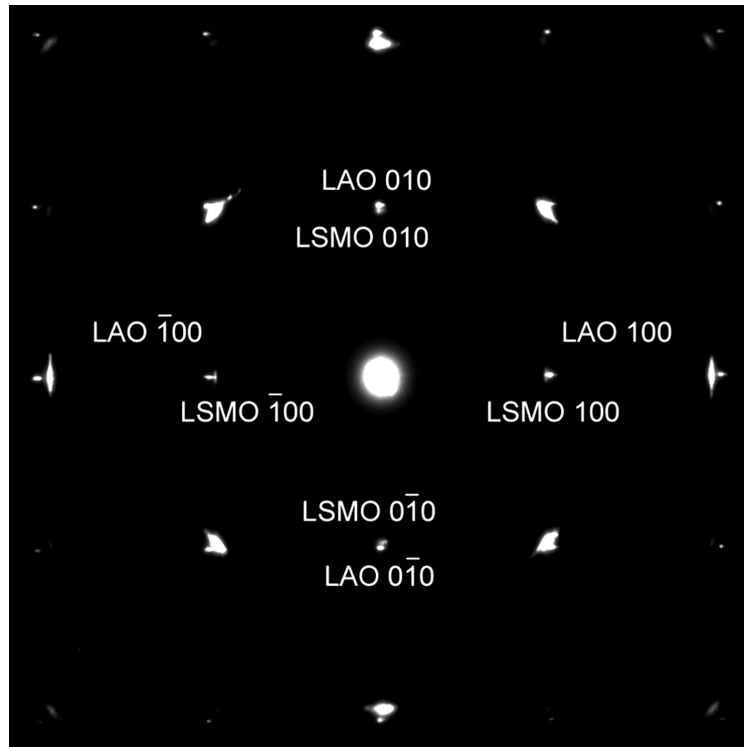Figure 4.17: The bright-field TEM image for the AD LSnMO (001) film.

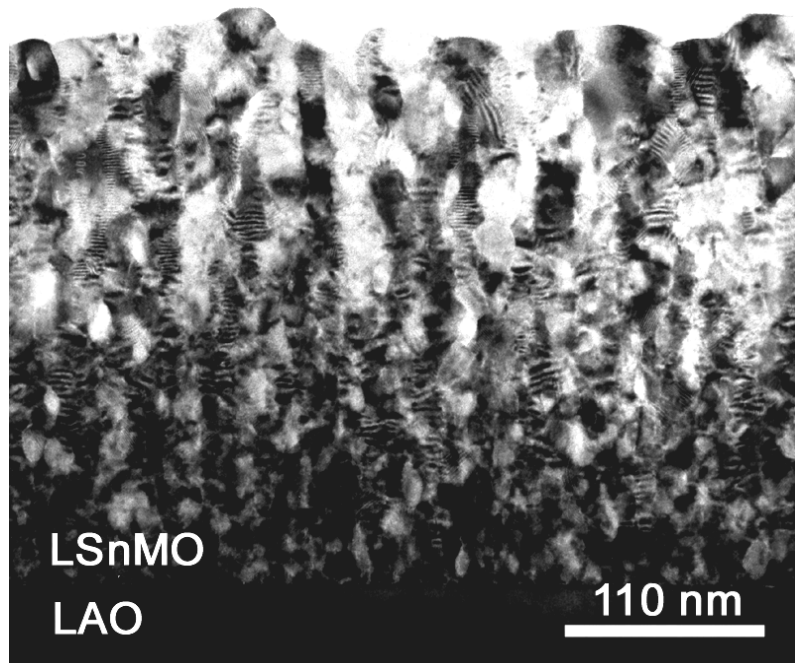Figure 4.18: The electron diffraction pattern for the AD LSnMO (001) film.

Figure 4.19: The bright-field TEM image for the PA LSnMO (001) film. Notice that the near-surface upper part of the PA LSnMO film displays apparent recrystallization signature upon prolonged annealing.
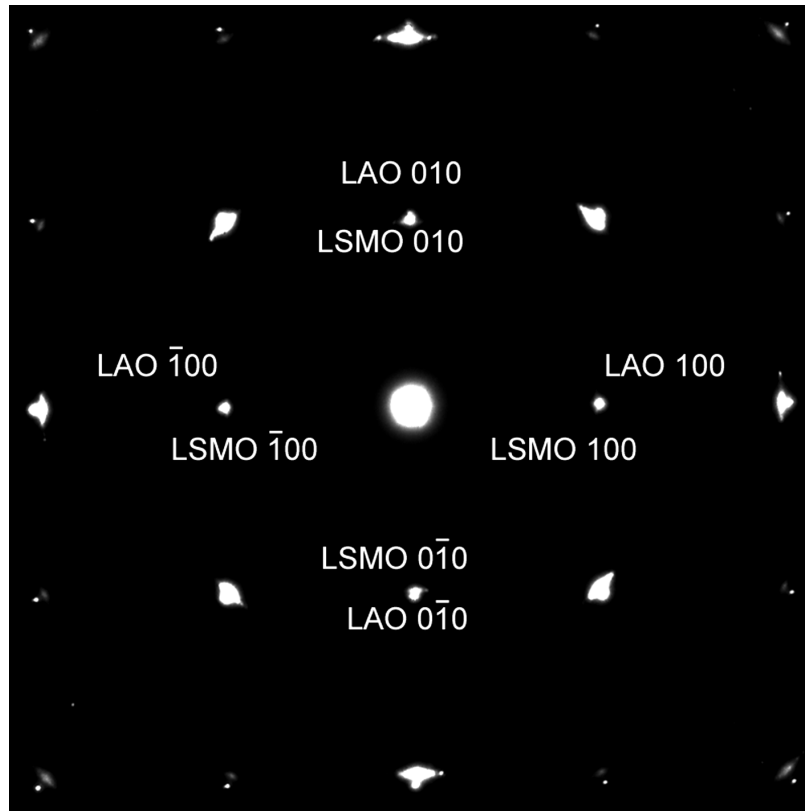
Figure 4.20: The electron diffraction pattern for the PA LSnMO (001) film.

From the above discussion, the strain relaxation effect is consistent with what observed in x-ray diffraction analyses and hence account for part of the magneto-transport properties obtained. The XAS results, however, remain to be clarified. In order to delineate the effect of annealing on the composition distribution of the doped element in the LSnMO film, the electron energy loss spectroscopy (EELS) mapping was performed on the TEM samples. Figures 21(a1)-(a5) show the zero-loss image of the AD-LSnMO film and the elemental maps of La, Sn, Mn, O, respectively. As revealed by the series of the images, the four constituents distribute uniformly over the entire AD-LSnMO film, indicating that they are presumably situated within the parent perovskite structure. The results are largely consistent with the data discussed above. Nevertheless, the elemental maps of the four constituent elements in the PA-LSnMO film display rather different results. As illustrated in Figs. 21(b1)-(b5), there are

clear evidence of local segregation of Sn and O in the "upper" region of the PA-LSnMO film (Fig. 21(b3) and (b5)). More interestingly, in these Sn-O segregated areas, both La and Mn are absent (Fig. 21(b2) and (b4)), indicating that the clusters formed are some kind of Sn-O compound. (From the previous XAS results it should be SnO_2.) This strongly implies that the oxygen annealing affected regions may indeed induce the formation of the La-deficient manganite, which, in turn, accounts for the marked enhancement in T_C and T_{IM} for the PA-LSnMO films described above.
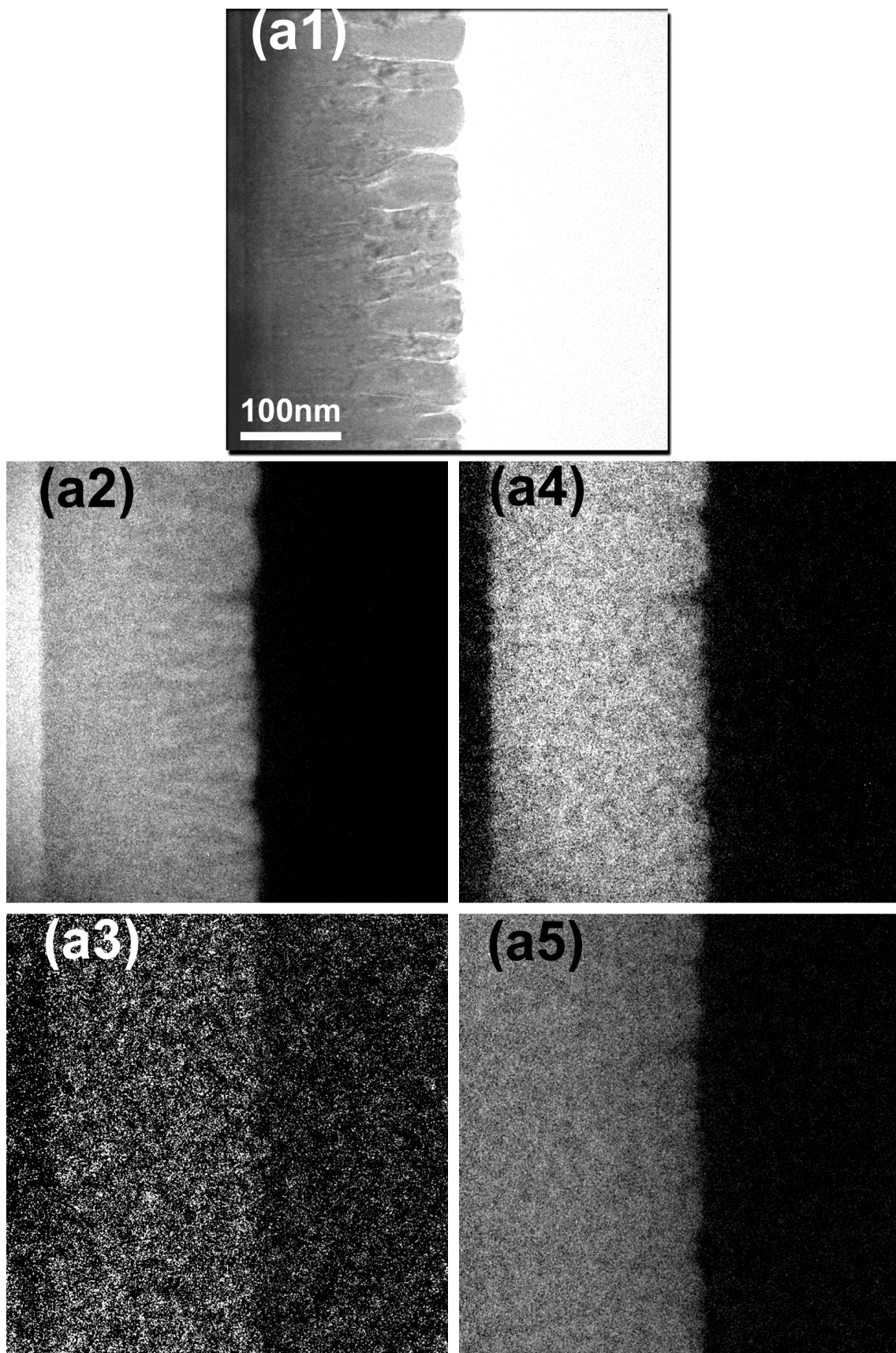
Figure 4.21: (a) The electron energy loss spectroscopy of the zero-loss image (a1) and the elemental maps of La (a2), Sn (a3), Mn (a4), and O (a5) of the AD LSnMO film.
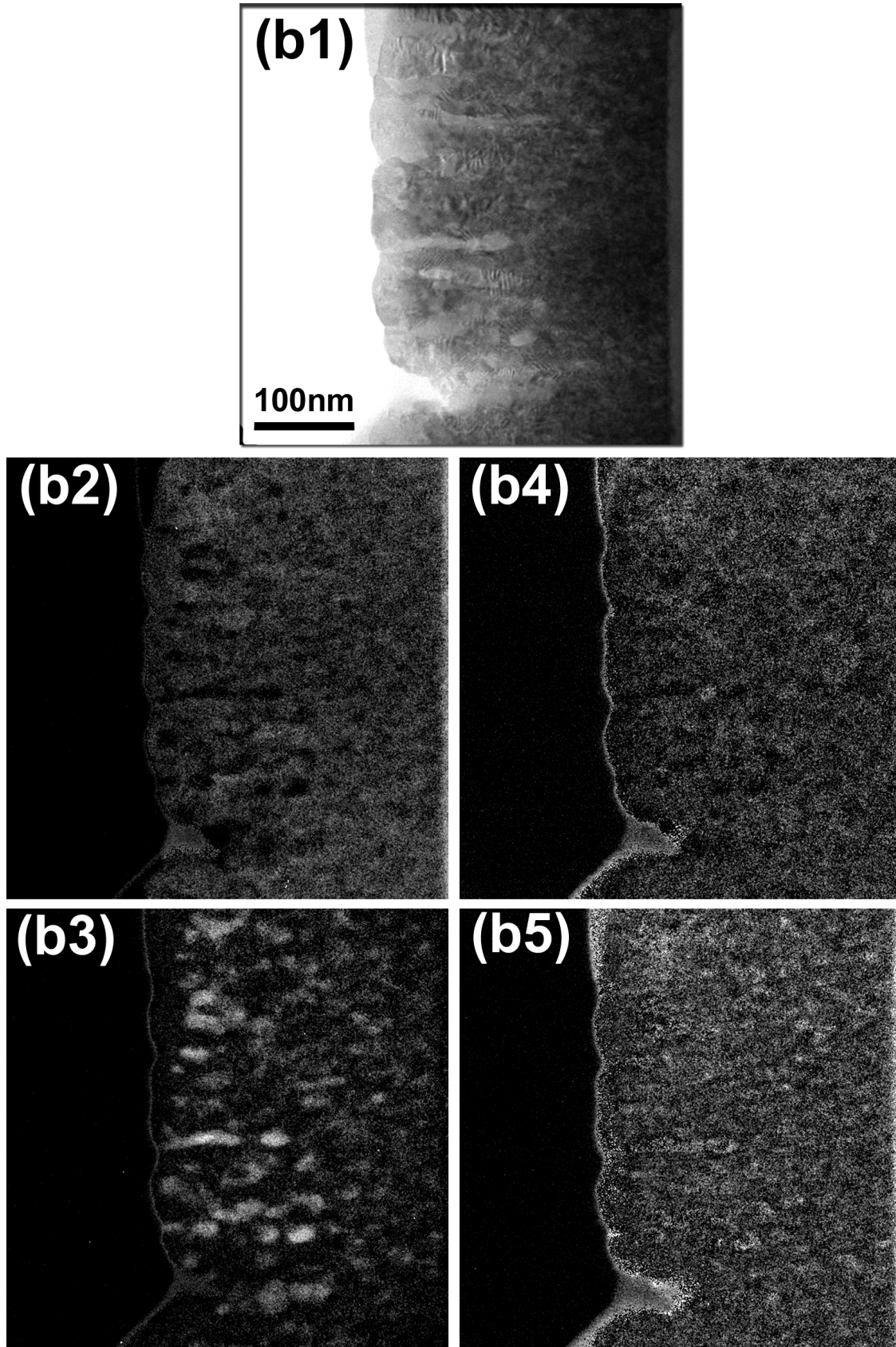
Figure 4.21: (b) The electron energy loss spectroscopy of the zero-loss image (b1) and the elemental maps of La (b2), Sn (b3), Mn (b4), and O (b5) of the PA LSnMO film.

4.5 Discussion

In the following, we try to put the experimental observations presented above together to see if it can reconcil to the outstanding issues about the CMR effects on Sn-doped manganites that we set forth to resolve at the beginning. The very first question to be answered is whether or not Sn-ions can substitute La-sites? The results obtained from the as-deposited films indicated that the substitution of the tetravalent Sn into the La site does prevail and result in a ferromagnetic-insulating manganite. The unexpected insulating behavior thus suggests either the lack of itinerant carriers or a fundamentally different exchange mechanism in the electron-doped regime. In the former scenario, similar double-exchange mechanism as in the hole-doped manganites gives rise to the paramagnetic-ferromagnetic transition and the existence of Mn^{2+} due to tetravalent doping of Sn^{4+} should result in enhancement of saturation magnetization below T_C owing to contributions from extra e_g electrons. However, due to the charge localization effects associated with strain-induced lattice distortion, the lack of itinerant electrons not only has hindered effective transport but also is responsible for the absence of long range FM order as manifested in the dramatic reduction of saturation magnetization and marked spin-glass-like behavior displayed in Fig. 4.1－4.3. The large epitaxial strain originally existent in the AD-film as revealed by the x-ray and X-TEM analyses seemed to give consistent support. On the other hand, the existence of Mn^{2+} in as-deposited and prolonged air exposure LCMO films was found to yield charge localization, and hence increasing resistivity and reducing magnetization, as well [103]. However, the effects of Mn^{2+}-induced charge localization seemed too modest to drive it into ferromagnetic insulator. Another possibility for explaining why our AD LSnMO films present as a ferromagnetic insulator is that the doping level ($x＝0.3$) is too low to drive the LSnMO into

n-type manganite. Chang *et al.* [73] indicated that the one of the main effects of doping Ce (up to $x = 0.3$) into LaMnO$_3$ was to dramatically shrink the hole-pockets near the Fermi level, instead of providing itinerant electrons and driving LCeMO into a n-type manganite. We believe that, from the evidence exhibited by XAS (especially on Sn ion) and EELS of XTEM analyses, for AD-LSnMO films, effective doping is obtained. However, the tetravalent- doping-induced hole-pocket shrinkage effects similar to that observed in Ce-doped manganites [73] may also happen in the present AD-LSnMO films. Together with the influences of the coherent strain and, possibly larger ion-size effect, thus resulted in the ferromagnetic insulating as well as spin-glass-like behaviors displayed by the AD-LSnMO films.

On the other hand, although post annealing under oxygen or argon is usually practiced in the fabrication of the "electron-doped" manganites, our experimental results demonstrate that it may not work as expected. According the XAS of Sn, we are tempted to rule out the existence of Sn^{2+} ions in the LSnMO films. The XAS of Sn for the PA-LSnMO film evidently shows the characteristics of Sn^{4+} valence. On the contrary, the same spectrum for the Ar-annealed film does not show the characteristics of either Sn^{2+} or Sn^{4+}, suggesting that the doped Sn in the initial target material may have been largely missing in the ArPA-LSnMO film. The question is how these spectrum results correlate to the magneto-transport properties displayed by the respective films? The TEM microstructure analyses and the EELS elemental map of PA-LSnMO film evidently showed that there is some kind of Sn-O compound formed during the post-annealing. The unambiguous Sn^{4+} feature of XAS results strongly implies that within the oxygen annealing affected regions it may have indeed induced the formation of the La-deficient manganite with SnO$_2$ clusters. The significant improvement of the CMR effects, including high T_C, T_{IM}, low resistivity and relatively large magnetization at low temperatures, is naturally explained within the context of this scenario. Finally, for the ArPA-LSnMO films, although also exhibit transitions from paramagnetic insulator to ferromagnetic metal albeit at

a significantly lower temperature with higher resistivity, the detailed mechanism may be fundamentally different from the oxygen-annealed PA-LSnMO films. In particular, the XAS of Sn for this film showed most of the Sn was missing after annealing. Thus, although the reduced average unit-cell volume for the ArPA- and PA-LSnMO films is indicative of strain relaxation, it is doubtful to attribute it as the sole reason for the obtained enhancement on the magneto-transport properties. It is quite possible that the change of average lattice parameters upon annealing is also coupled with change of composition, or even segregation of second phases. In this scenario, the excessive oxygen presumably present in the PA-LSnMO films would provide more itinerant carriers and Mn^{4+} content [105], and is responsible for the improvement of electrical transport and magnetic properties. While Ar-annealing, though may induce the loss of Sn and hence result in La-deficient manganite, it may also provoke the formation of non-ferromagnetic Mn^{2+} component and give rise to charge localization-induced increase in resistivity and reduction in saturated magnetization [103].

Finally, we make a brief comparison between LSnMO and LCeMO, the two representative "electron-doped" manganites. The primary distinction of these two materials is the ionic size difference of Sn^{4+} (0.81Å) and Ce^{4+} (0.97Å) [104]. One of the instant effects resulted from this was the low temperature saturation magnetization obtained from the as-deposited films with $M_{LCeMO} \sim 1.4\mu_B$/Mn-site [75] and $M_{LSnMO} \sim 0.4\mu_B$/Mn-site measured under T＝10K, H＝100Oe. This may be easily attributed to more severe structure disorder originated from the larger ionic size difference between Sn^{4+} and La^{3+} (0.32Å) than that between Ce^{4+} and La^{3+} (0.16Å). However, as the films were annealed under oxygen environment, both LSnMO and LCeMO exhibit similar magneto-transport properties. The existence of SnO_2 or CeO_2 [75] seemed to indicate that both films tend to turn into La-deficient manganites after annealing. However, for as-deposited PLD LCeMO films, there are still some discrepancies on the magneto-transport properties reported in the literature remained to be clarified [71－75].

4.6 Conclusion

In summary, we have presented systematic investigations on one of the highly anticipated electron-doped CMR materials. Single-phase $La_{0.7}Sn_{0.3}MnO_3$ (LSnMO) thin films were grown on $LaAlO_3$ substrates by pulsed laser deposition. The as-deposited LSnMO films are ferromagnetic insulators with typical Curie temperature around 150 K. Both the electronic structure revealed by the x-ray absorption spectra (XAS) and the detailed TEM analyses indicate that in this case the doped Sn-element is indeed acting as the tetravalent ion uniformly distributed in the $LaMnO_3$ parent compound. The large internal strain originated from the marked ion size difference between the doped Sn^{4+} and substituted La^{3+} ions, however, is believed to hinder the long-range itinerancy of the carriers, hence preventing it from becoming metallic. Unfortunately, due to the insulating nature of these as-deposited LSnMO films, it is not clear whether it is indeed "n-type" electron-doped manganite. *Ex-situ* annealing in oxygen and argon both drive the films to exhibit insulator-metal transition with hole-doped characteristics when becoming ferromagnetic. The transition temperatures, however, are different for films annealed in different environments, presumably due to the final phase and compositions obtained. From the results of magnetoresistance measurements and XAS, it is suggestive that LSnMO films annealed in argon causes the significant loss of Sn and results in La-deficient phase. Whereas those annealed in oxygen appeared to form some kind of Sn-O compound, turning the films into La-deficient manganite, albeit with some excessive oxygen. We emphasize that the existence of tetravalent Sn from x-ray absorption spectroscopy (XAS) should not be taken as the sole evidence of achieving electron-doped manganite. As being clearly demonstrated in this study, it may just reveal the emergence of SnO_2.

Chapter 5

Phase diagram and magnetic properties of La$_{1-x}$Sn$_x$MnO$_3$ manganites

In this chapter, we report the magnetic properties and electronic structure of electron doped manganites La$_{1-x}$Sn$_x$MnO$_3$ (x＝0.1~0.5) thin films fabricated by pulsed laser deposition (PLD) method. The as-deposited films were all ferromagnetic insulators with no sign of insulator-metal transition (IMT). It is believed that the structural disorder may have obstructed the long range magnetic ordering and resulted in ferromagnetic-insulator characteristics. Moreover, it is found that with the increasing doping level of Sn, the crystalline structure of the as-deposited films becomes worse and the magnetic properties get deteriorated. The x-ray absorption spectroscopy (XAS) of the as-deposited LSnMO films showed signatures of Mn^{3+}/Mn^{2+} mixed-valence indicating that tetravalent Sn ions indeed have resulted in electron-doping into the e_g band of Mn. In order to deliberate the solubility of Sn in the LaMnO$_3$ parent compound and to delineate the origin of the additional magnetic transition near 44K, systematic investigation of x-ray diffraction (XRD) and transmission electron microscopy (TEM) were carried out. The phase diagram of the La$_{1-x}$Sn$_x$MnO$_3$ reveals that the properties of the electron-doped manganites are not symmetric to their hole-doped

counterparts.

5.1 Motivation

Recently, the colossal magnetoresistance (CMR) manganites have attracted much attention due to their intriguing physical properties and great application possibilities [2, 3]. The study of the hole-doped manganites manifested by a paramagnetic-ferromagnetic transition at the Curie temperature (T_C) accompanied by a dramatic decrease in resistivity around a similar temperature (T_{IM}) was attributed to the charge-spin interaction of mixed-valence Mn^{3+}/ Mn^{4+} ions under the framework of Zener's double-exchange (DE) mechanism [14]. On the other hand, it is also heuristic to study the related magneto-transport properties of the "electron-doped" manganites by substituting La^{3+} with tetravalent ions. It was found that the investigations of the electron-doping system revealed that CMR behavior could occur in these systems of a mixed valence state of Mn^{3+}/Mn^{2+}, despite there are no exact evidences to expound and prove that the dominated conduction carriers in the "electron-doped" manganites are indeed "electrons". Consequently, if the electron-doped manganites (*n*-type) are integrated with hole-doped manganites (*p*-type), the achievement of the CMR $p-n$ junction could be realized. It will bring about plentiful physical interest and great application potential in the technology development [68].

In this respect, CMR effect has been observed in LSnMO [92−95, 102, 106], albeit the single-phase samples were hardly obtainable by the solid-state reaction technique and only limited doping ($x=0.1-0.3$) has been achieved in thin film form. Since the relatively large ion size mismatch between Sn^{4+} and La^{3+}, it is desirable to perform systematic studies on LSnMO system with higher doping to explore the prominent roles played by lattice degree of

freedom in giving rise to both CMR [96] effect and phase-coexistence [50] phenomena. In this chapter, we report the results of extending the doping level of Sn to $x \sim 0.5$ in $La_{1-x}Sn_xMnO_3$ (LSnMO) by carefully adjusting the process conditions in preparing the LSnMO films. The magnetic properties of the films were used to construct a phase diagram of the system, which should provide prominent information for understanding the underlying mechanism of these materials.

5.2 The preparation of $La_{1-x}Sn_xMnO_3$ thin films on $LaAlO_3$ substrates

Sintered LSnMO targets were prepared by conventional solid-state reaction technique. La_2O_3 and SnO_2 were first calcined at $800^{\circ}C$ for 8 h. The calcined products were then mixed and ground with stoichiometric (with nominal $x=0.1-0.5$) amount of $MnCO_3$ and sintered at $1200^{\circ}C$ for 30 h. After repeating the process three times, it was pressed into pellet and sintered at $1200^{\circ}C$ for 72 h. $L_{1-x}Sn_xMnO_3$ films were fabricated at $780^{\circ}C-830^{\circ}C$ on single crystalline LAO (100) substrates using by PLD. The temperature dependence of magnetization (M(T)) was measured using a Quantum Design® SQUID system with a maximum applied field strength of 7 Tesla. The film structure was examined by x-ray diffraction (XRD). For the electronic structure revealing the valence state of Mn ion, the x-ray absorption near edge spectroscopy (XANES) experiment was performed at the National Synchrotron Radiation Research Center of Taiwan. The cross-section transmission electron microscopy (TEM) and selected area diffraction (SAD) were applied to investigate the microstructure and inspect the possible impurity phase.

5.3 The structure characterization

Fig. 5.1 compares the XRD results for as-deposited $La_{1-x}Sn_xMnO_3$ films obtained at $T_s =$ 780℃ $(x = 0.1-0.3)$, 800℃ $(x = 0.4)$ and 830℃ $(x = 0.5)$, respectively. Except for the $L_{0.5}Sn_{0.5}MnO_3$ sample, the other four samples reveal all c-axis oriented perovskite structure with no discernible impurity phase within the resolution of our XRD system. It is also evident that the crystallinity of the film degrades with increasing the amount of doped Sn. We believe that the structural degradation is mainly due to the existence of large strain resulting from the ionic size misfit between Sn^{4+} and La^{3+}. Figure 5.2 revealed that there exhibit no feature of LSnMO perovskite structure for the $L_{0.5}Sn_{0.5}MnO_3$ thin film, and the occurrence of the significantly impurity phase $(2\theta = 28.9)$ may not be obviated, suggesting that it may be difficult to substitute the La ions by 50% Sn in the $LaMnO_3$ parent compound, and the doping level of $L_{1-x}Sn_xMnO_3$ may be limited to $x = 0.4$. More experimental evidence concerned this argument will be presented thereinafter and discussed in section 5.5.
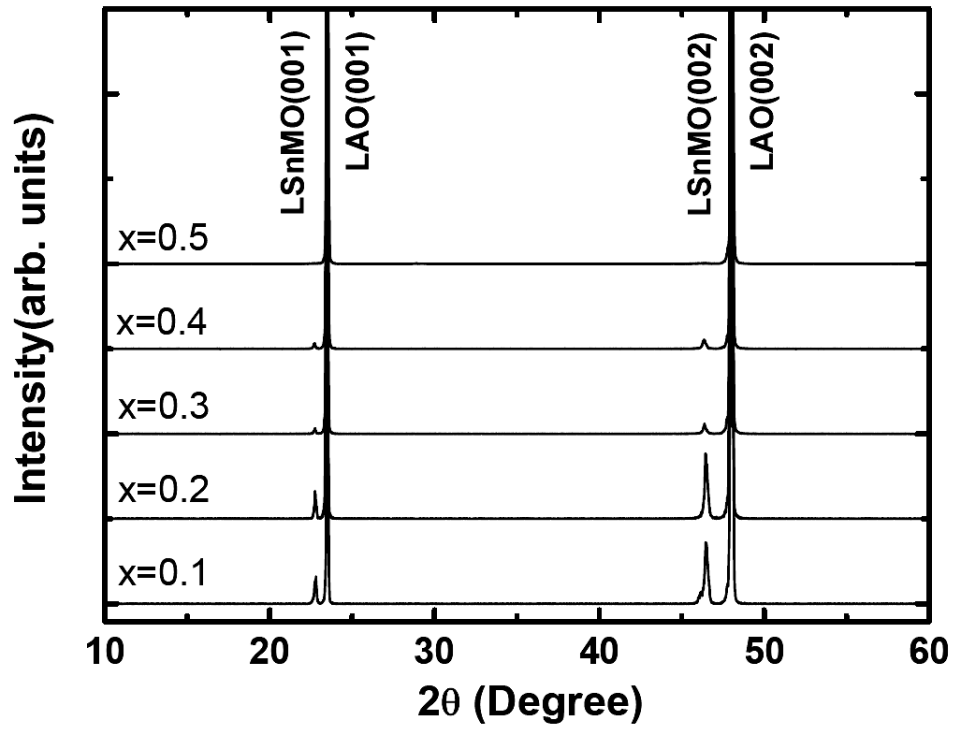
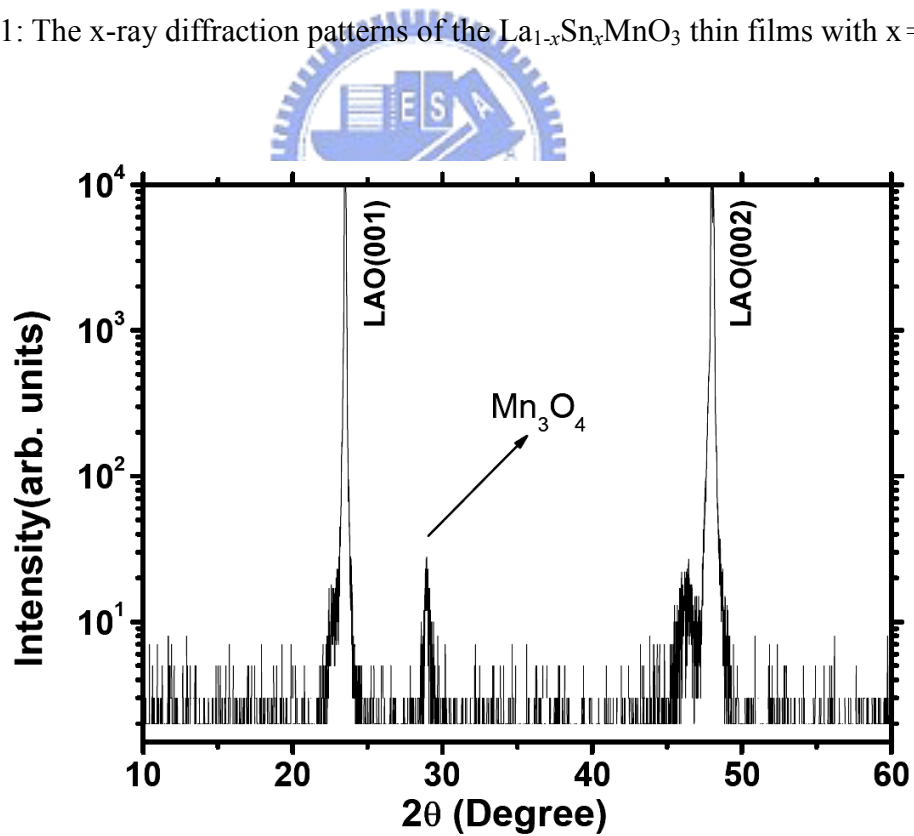Figure 5.1: The x-ray diffraction patterns of the $La_{1-x}Sn_xMnO_3$ thin films with x＝0.1~0.5.

Figure 5.2: The x-ray diffraction pattern of the $La_{0.5}Sn_{0.5}MO_3$ thin film.

5.4 The magnetic properties

Fig. 5.3 shows the magnetization of the LSnMO films as a function of temperature and applied magnetic field. We can find the suppression of the magnetization for the LSnMO films with higher doping level when measured at 0.01 T. With the increase of Sn content, the Curie temperature (T_C) decrease. We believed the LSnMO present large local lattice distortion and the magnetic dilution are considered to be responsible for the present observations. Another interesting phenomenon is the appearance of the additional magnetic transition at about 44K under 0.01T applied magnetic field. This might be ascribed to the contribution of some lower T_C ferromagnetic phase, which was related to the emergence of manganite oxides [50, 107－108]. Another possibility is the depinning of magnetic domain walls at specific temperature and magnetic field, and the pinning is due to some disorders at the wall [82, 109－110]. The magnetic phase separation results in the presence of remnant ferromagnetic phase below T_C, which may encounter a magnetic phase transition at lower temperature. Nevertheless, it seems that the appearance of the subtle additional magnetic transition is related to the deposition environments of the LSnMO thin films, as well as the solubility of Sn in the perovskite LaMnO$_3$ structure. We will return to this point in section 5.5.

In addition, the magnetic hysteresis measurement ($M(H)$) of the LSnMO films were performed at 50K with the magnetic field applied parallel to the plane of the films, as shown in Fig. 5.4. The coercive fields H_c for these samples are as displayed in Table 5.1. The magnetic field needed to saturate the magnetization is about 4KOe. All the experimental evidences indicate that the films are indeed ferromagnetic. The *M-H* relationships of La$_{0.5}$Sn$_{0.5}$MnO$_3$ film were carried out at different temperatures (10K, 30K, 50K, 170K), as illustrated in Fig. 5.5. It revealed that the sample exhibits no sign of ferromagnetism at *T*=170K since the Curie temperature of the sample is nearly 170K. The occurrence of the

hysteresis loop is due to the formation of ferromagnetic ordering as the temperature decreases. However, the largest hysteresis loop can be observed at T=30K, which even larger than the one at T=10K. Here, we believe there may be the contribution of another magnetic ordering beyond the pure $La_{1-x}Sn_xMnO_3$ manganites.
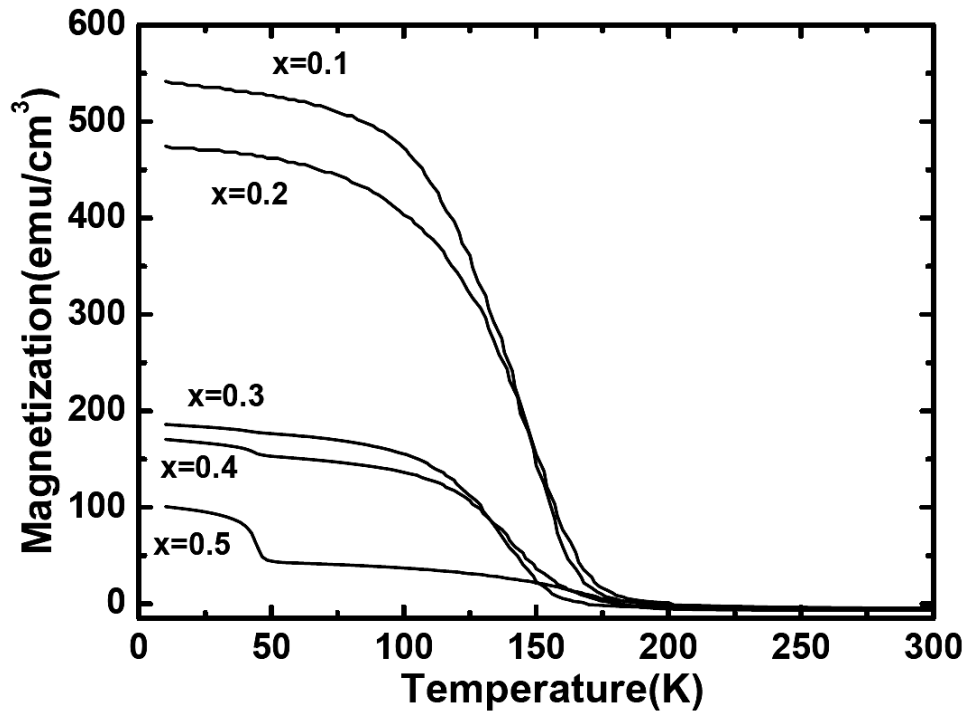

Figure 5.3: The field-cooled and zero-field-cooled temperature-dependent magnetizations ($M(T)$) measured at 0.1 T for LSnMO thin films.
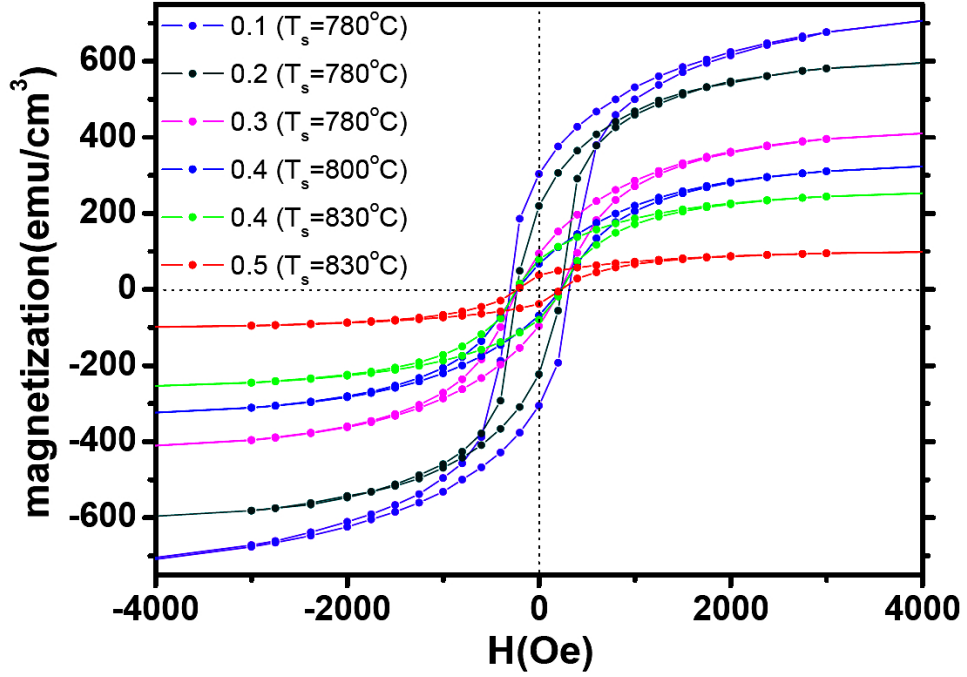
Figure 5.4: The magnetic hysteresis measurements ($M(H)$) of the LSnMO films were performed at 50K with the magnetic field applied parallel to the plane of the films.

La$_{1-x}$Sn$_x$MnO$_3$	x=0.1	x=0.2	x=0.3	x=0.4	x=0.4	x=0.5
H_c(Oe)	300	227	217	218	230	212
T_s(℃)	780	780	780	800	830	830

Table 5.1: The coercive fields H_c of La$_{1-x}$Sn$_x$MnO$_3$ (x=0.1~0.5) samples deposited at various temperature.
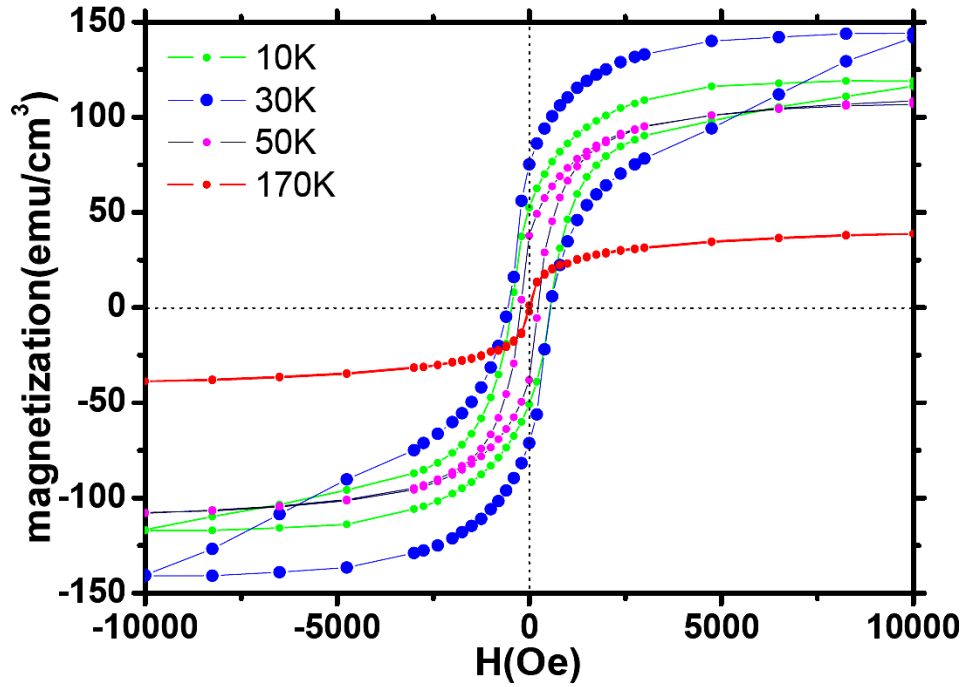
Figure 5.5: The *M-H* relationships of $La_{0.5}Sn_{0.5}MnO_3$ film measured at different temperature (10K, 30K, 50K, and 170K).

5.5 The solubility of Sn in the LaMnO$_3$ perovskite

From the discussion in section 5.4, one notable phenomenon on the magnetic properties is the presence of an additional upturn at $T \approx 45K$ in the result of $M(T)$ for $x \geqq 0.4$ LSnMO samples. Morales *et al* [107, 116−118] reported the phase formation of Sn doped LaMnO$_3$ perovskite in the polycrystals La-Sn-Mn-O system and concluded that the magnetic signal around 45 K is assumed to correspond to the ferrimagnetic Mn$_3$O$_4$, albeit there appears no direct evidences other than the result of $M(T)$ to demonstrate the existence of Mn$_3$O$_4$. Here we present the effort to keep the issue in depth and try to delineate the possible mechanism. The field-cooled and zero-field-cooled temperature-dependent magnetizations ($M(T)$) measured at 0.1 T for $La_{1-x}Sn_xMnO_3$ ($x = 0.1 − 0.5$) thin films deposited at various temperature are

proposed. The $La_{0.9}Sn_{0.1}MnO_3$ and $La_{0.8}Sn_{0.2}MnO_3$ samples were prepared at $T_s = 780℃$, 800℃, and 830℃, respectively, as shown in Fig.5.6 − 5.7. It was observed that the magnetization of these three samples were comparable and there were no sign of additional magnetic transition near $T = 44K$ even for the $La_{0.9}Sn_{0.1}MnO_3$ and $La_{0.8}Sn_{0.2}MnO_3$ samples prepared at $T_s = 830℃$. However, as we discuss the $La_{0.7}Sn_{0.3}MnO_3$ samples were prepared at $T_s = 780℃ − 830℃$, respectively, as shown in Fig.5.8. It was observed that although the magnetization of the samples were comparable but there were additional magnetization transition for the $La_{0.7}Sn_{0.3}MnO_3$ samples preparation at $T_s > 800℃$. The results reveal the solubility of Sn in the $LaMnO_3$ perovskite may be limited to $x = 0.3$, when $T_s > 800℃$. Moreover, an additional magnetic transition was observed in the $La_{0.6}Sn_{0.4}MnO_3$ and $La_{0.5}Sn_{0.5}MnO_3$ samples, as shown in Fig. 5.9 − 10. The occurrence of this additional magnetic transition may be due to either the inhomogeneity of the components distribution in the LSnMO samples, or some impurity phase with lower T_C. Since the transition is rather sharp, the former is believed to be more unlikely reason.
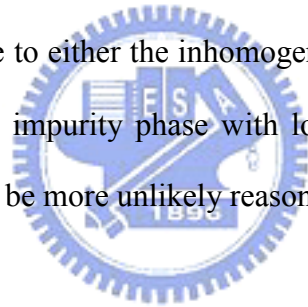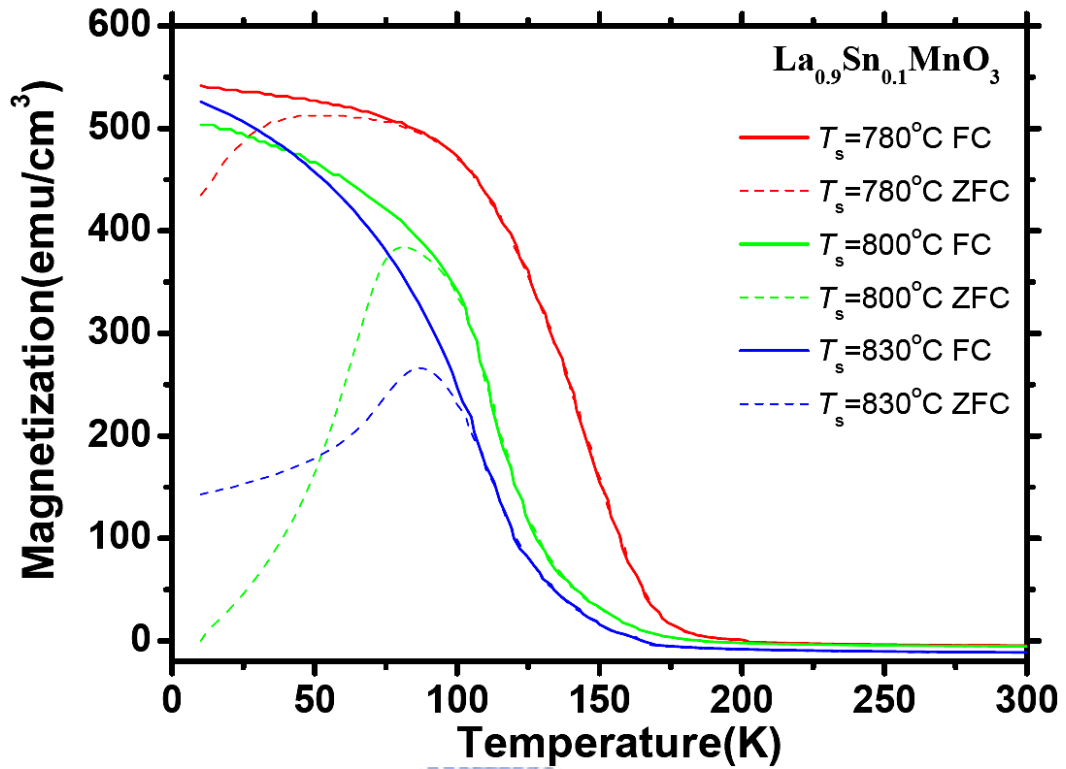
Figure 5.6: The field-cooled and zero-field-cooled temperature-dependent magnetizations ($M(T)$) measured at 0.1 T for $La_{0.1}Sn_{0.9}MnO_3$ thin films deposited at various temperature.
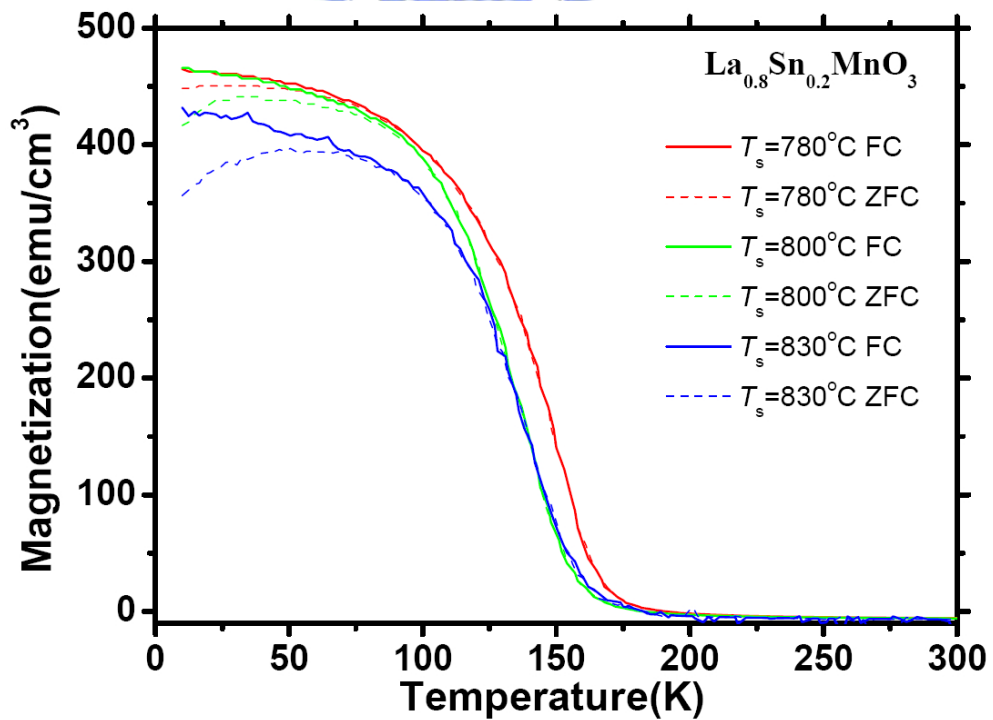

Figure 5.7: The field-cooled and zero-field-cooled temperature-dependent magnetizations ($M(T)$) measured at 0.1 T for $La_{0.2}Sn_{0.8}MnO_3$ thin films deposited at various temperature.

Figure 5.8: The field-cooled and zero-field-cooled temperature-dependent magnetizations ($M(T)$) measured at 0.1 T for $La_{0.3}Sn_{0.7}MnO_3$ thin films deposited at various temperature.
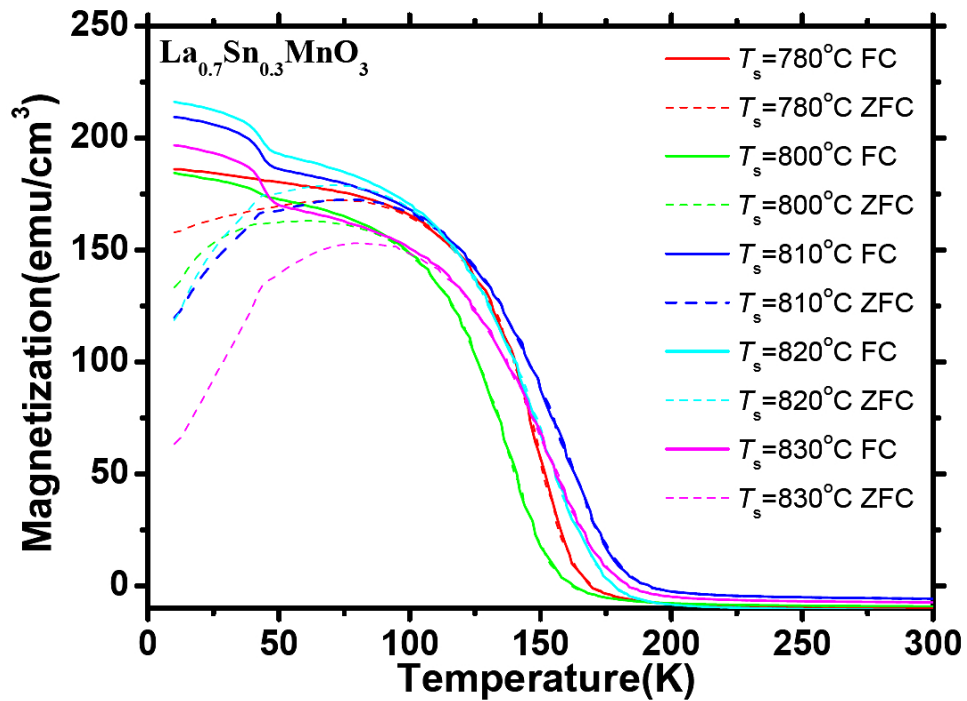

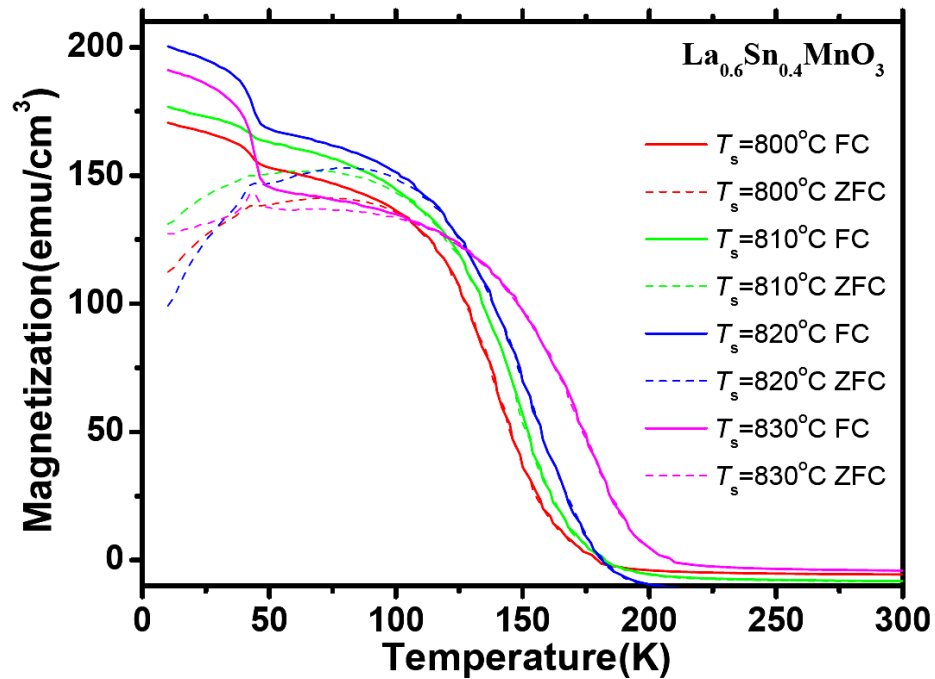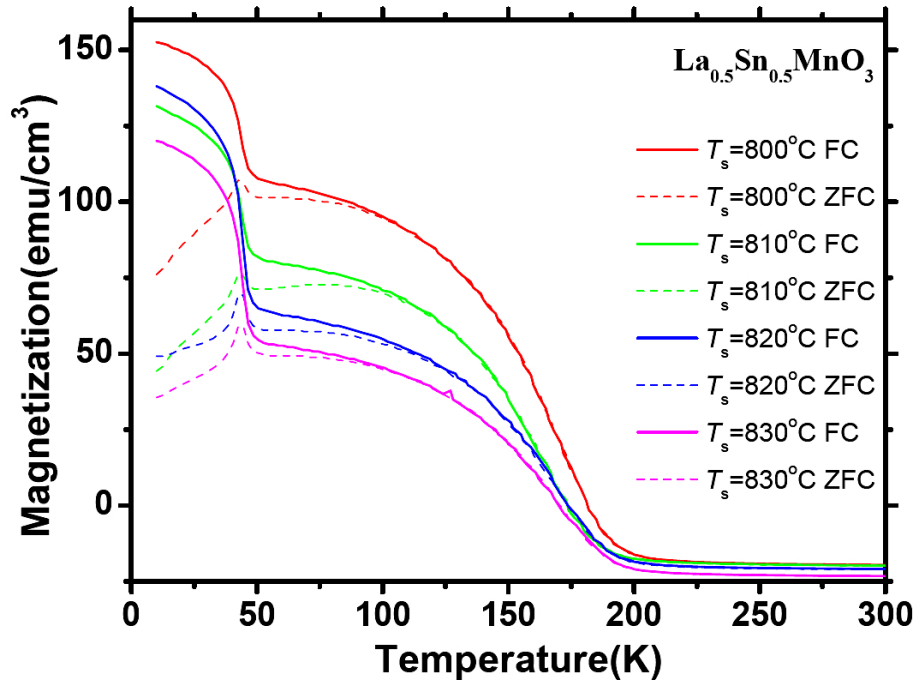Figure 5.9: The field-cooled and zero-field-cooled temperature-dependent magnetizations ($M(T)$) measured at 0.1 T for $La_{0.4}Sn_{0.6}MnO_3$ thin films deposited at various temperature.

Figure 5.10: The field-cooled and zero-field-cooled temperature-dependent magnetizations ($M(T)$) measured at 0.1 T for $La_{0.5}Sn_{0.5}MnO_3$ thin films deposited at various temperature.

On the other hand, from the discussion mentioned above, the similar additional magnetic transition near 44K were found for the $La_{1-x}Sn_xMnO_3$ (x＝0.3－0.5) samples deposited at T_s＞800℃, suggesting the origin of the additional magnetic transition may be the same for these samples. From the XRD data of the $La_{0.5}Sn_{0.5}MnO_3$ film, a second phase (2θ＝28.9) of Mn_3O_4 was observed and with no obvious sign of perovskite structure. Thus, the additional magnetic transitions near 44K could be ascribed to the contribution of the Mn_3O_4 [50, 107, and 108]. Moreover, Fig. 5.11 and Fig. 5.12 illustrated the bright-field TEM images for the $La_{0.5}Sn_{0.5}MnO_3$ film deposited at 830℃ .and $La_{0.7}Sn_{0.3}MnO_3$ (001) film deposited at 780℃, which exhibit different features. The microstructure of the $La_{0.7}Sn_{0.3}MnO_3$ film appears to be rather homogeneous and there is no trace of any additional compound existing within the interface of film and substrate, while the microstructure of the $La_{0.5}Sn_{0.5}MnO_3$ film exhibit quite inhomogeneous distribution even though the sample thickness was merely about 50nm.

The columnar structures of the $La_{0.5}Sn_{0.5}MnO_3$ film, unlike the $La_{0.7}Sn_{0.3}MnO_3$ film, consisted of several different grains in one column, indicating that the growth might have been accompanied by significant stress relaxation. In addition, the electron diffraction pattern for the $La_{0.5}Sn_{0.5}MnO_3$ film deposited at 830℃ reveals no apparent diffraction points for LSnMO phase, as shown in Fig. 5.13, some impurity diffraction points were found, identified as that of Mn_3O_4. Therefore, from the evidences of XRD, $M(T)$ and TEM, the observation of the additional magnetic transition near 44K in $M(T)$ is attributed to the magnetic contribution of Mn_3O_4. Unfortunately, the attempt of preparing $La_{0.5}Sn_{0.5}MnO_3$ film at lower T_s (780℃) has been unsuccessful; the as-deposited films did not show sign of magnetism. On the other hand, second phase was usually noticed for $La_{0.5}Sn_{0.5}MnO_3$ films prepared at $T_s = 800$℃. Therefore, the doping level of the $La_{1-x}Sn_xMnO_3$ may have been limited to $x = 0.4$. The results indicate that the large ionic size mismatch between La^{3+} and Sn^{4+} and deposition temperature (T_s) are the dominating factors in limiting the solubility of Sn in the $LaMnO_3$ perovskite.
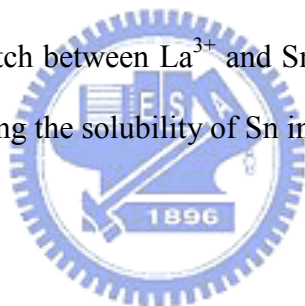
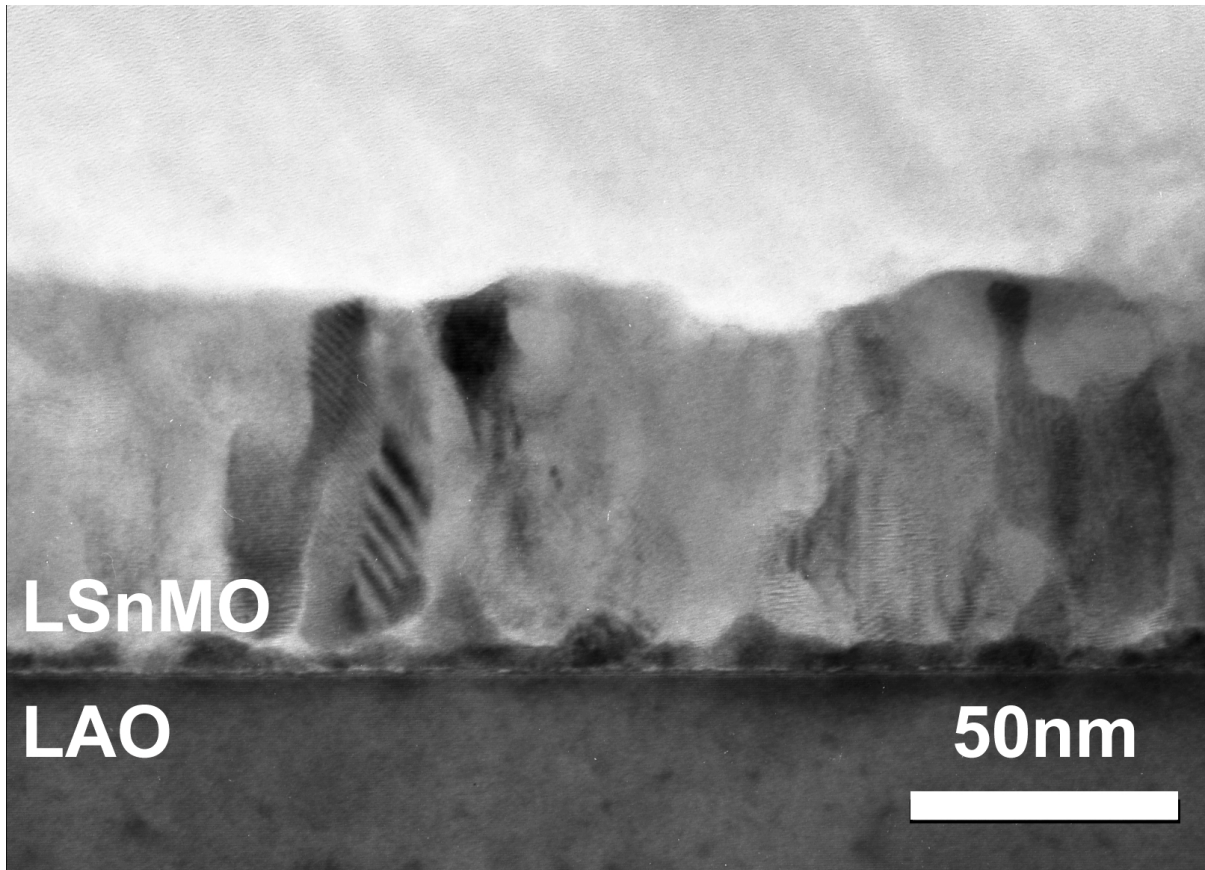Figure 5.11: The bright-field TEM image for the $La_{0.5}Sn_{0.5}MnO_3$ film deposited at 830℃.
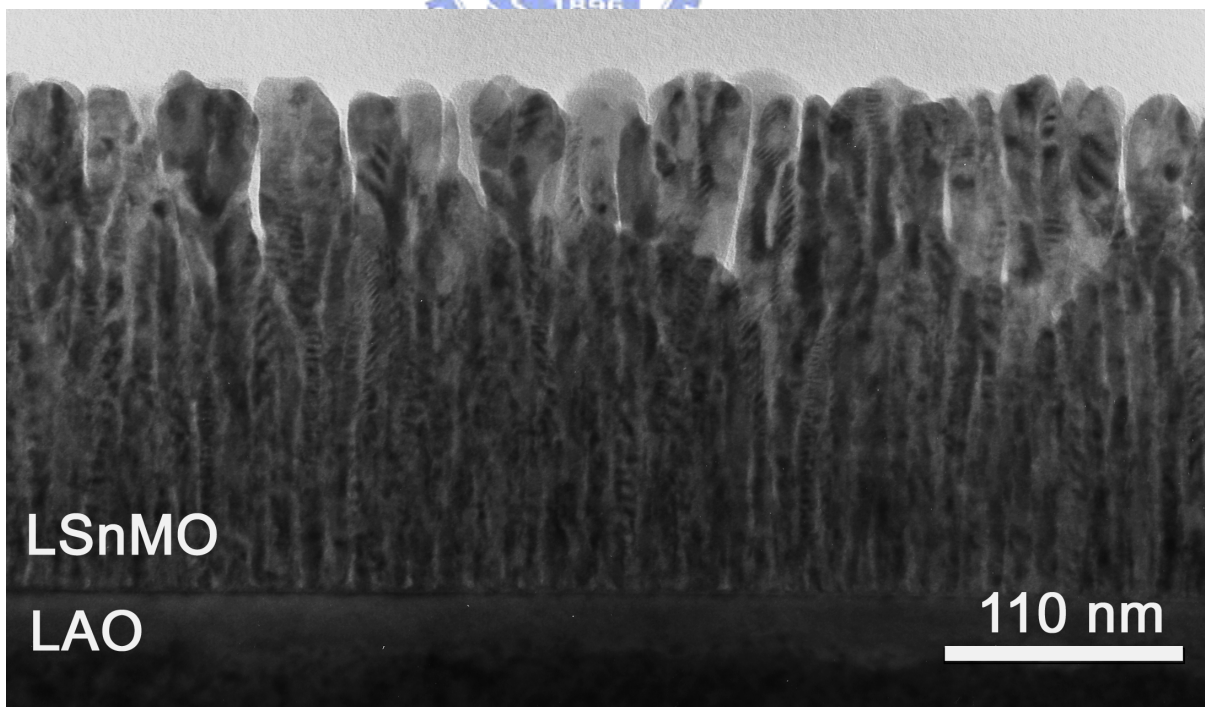
Figure 5.12: The bright-field TEM image for the $La_{0.7}Sn_{0.3}MnO_3$ (001) film deposited at 780℃.
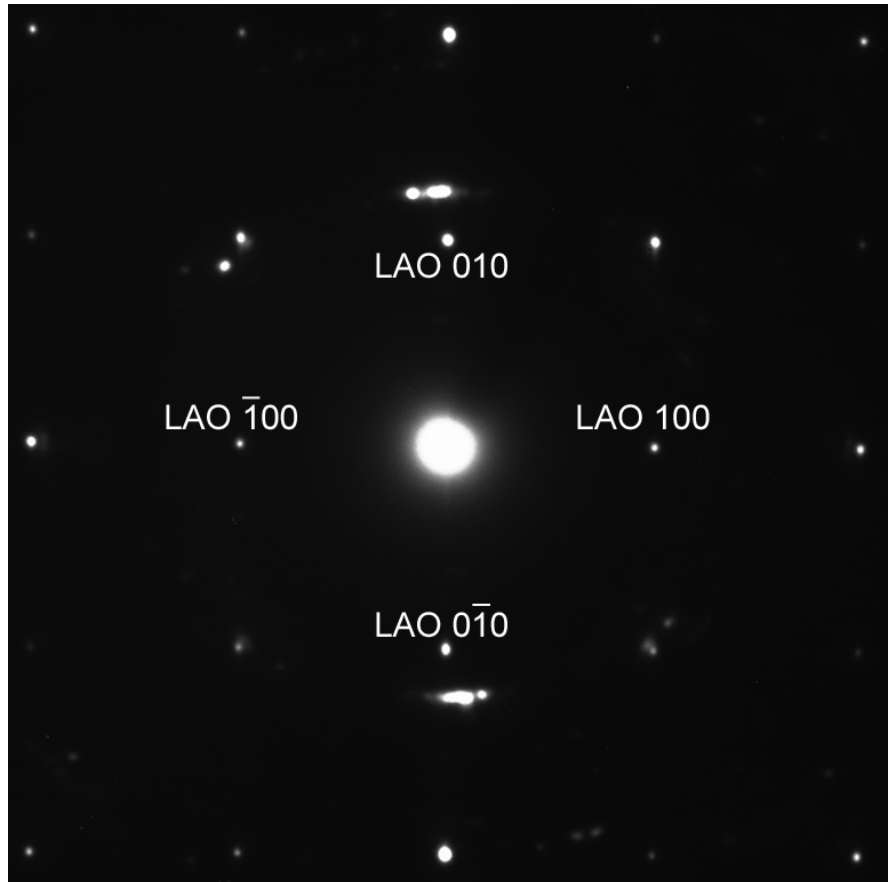
Figure 5.13: The electron diffraction pattern for the $La_{0.5}Sn_{0.5}MnO_3$ film deposited at 830℃.

5.6 Electronic structure of $La_{1-x}Sn_xMnO_3$ ($x=0.1-0.4$)

In order to check the effect of Sn-doping on the valence states of Mn ions, x-ray absorption near edge spectroscopy (XANES) measurements were measured at the National Synchrotron Radiation Research Center (NSRRC) of Taiwan. Fig. 5.14 shows the results of Mn-$L_{2,3}$ obtained for $x=0.1-0.4$ films. It demonstrates that the present samples indeed displays qualitative characteristics of Mn^{2+}/Mn^{3+} mixed valence state, indicating that Sn-doping does drive Mn^{3+} into Mn^{2+}. From the XAS of Mn, it reveals the amount of Mn^{2+}

characteristics is increasing at the higher Sn doping level. It suggests that the electronic structure can be controlled by the arrangement of the Sn doping level. In addition, the study of the XAS of Sn is also important, as illustrated in Fig. 5.15. The results revealed the similar characteristics of the five Sn-doped LaMnO$_3$ manganites, which are in sharp contrast to that of SnS and SnO$_2$. However, as shown in Fig. 5.16, the characteristics of Sn in the LSnMO samples prepared at high temperature ($T_s \geqq 800℃$) are presented particular XAS characteristics in addition to the samples prepared at $T_s \leqq 800℃$, as well as the two standard reference compounds (SnO$_2$ and SnS).
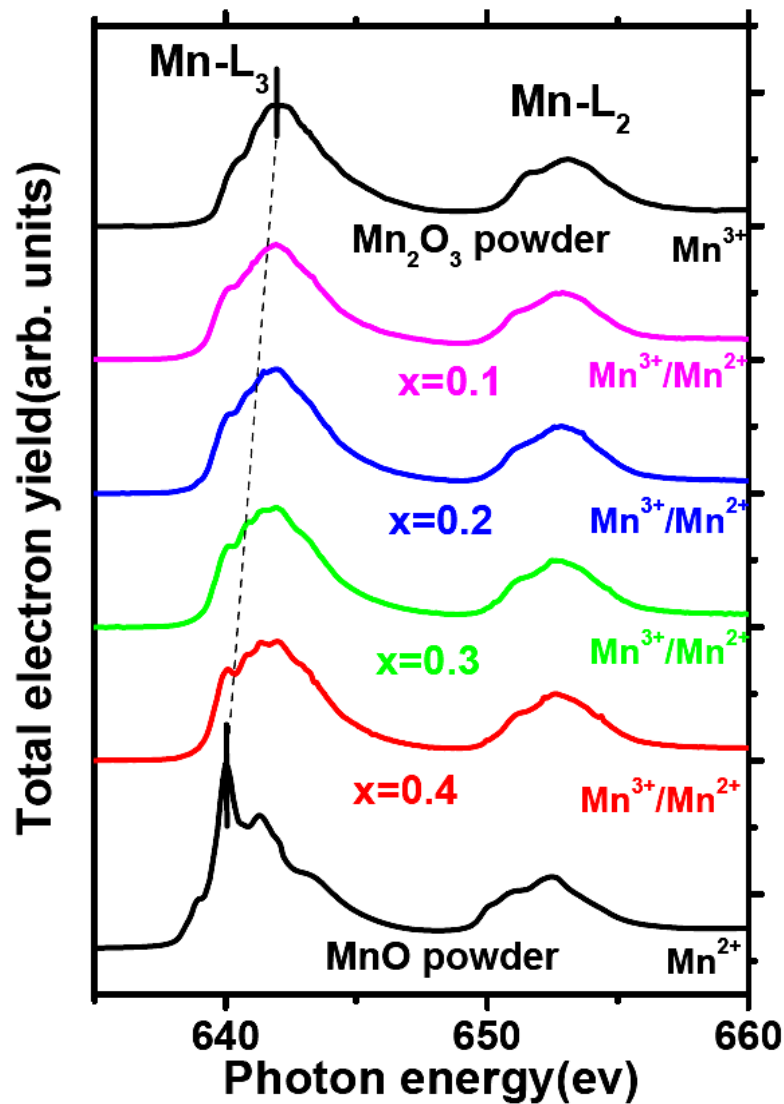

Figure 5.14: The x-ray absorption spectra of Mn-L$_{2,3}$ for LSnMO films. Spectra for various standard reference compounds are also displayed for comparison.
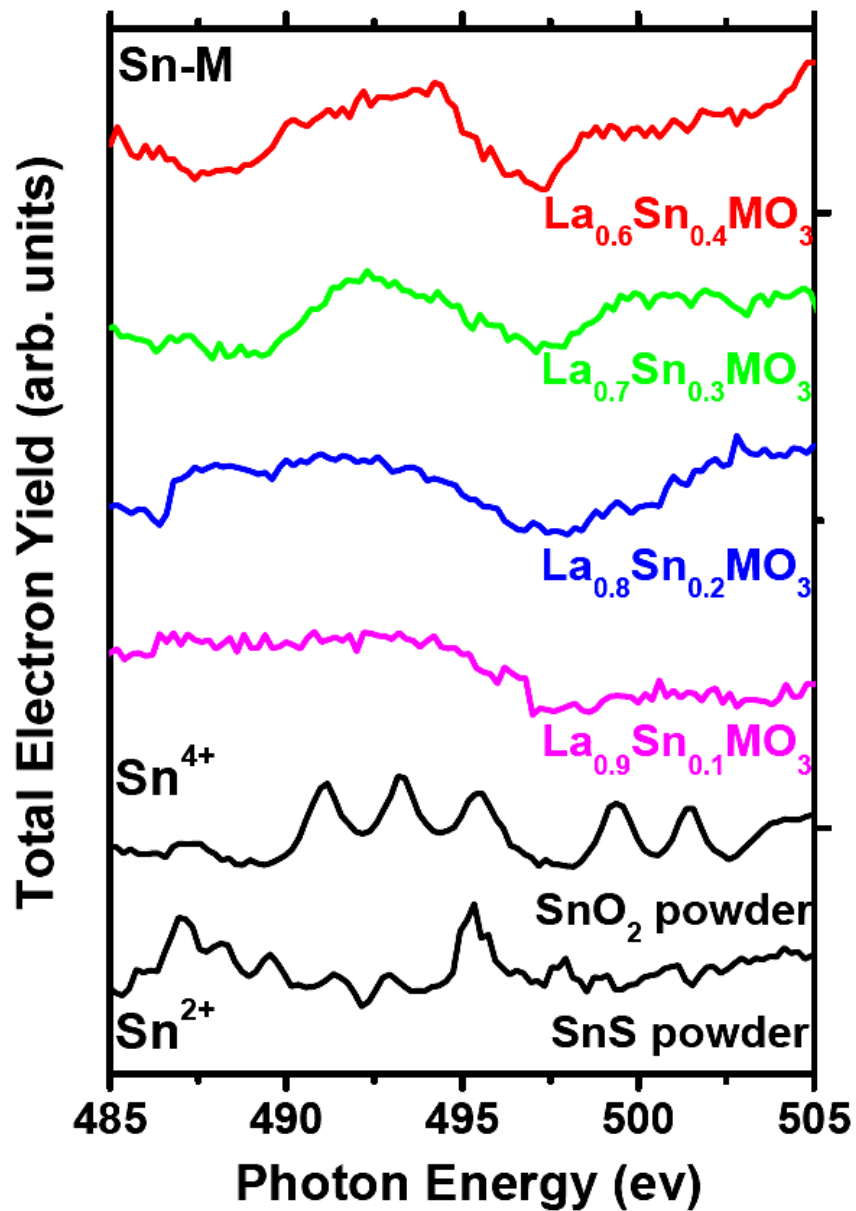
Figure 5.15: The x-ray absorption spectra of Sn for $La_{1-x}Sn_xMnO_3$ ($x=0.1-0.4$) films. These four samples were all prepared at $T_s \leqq 800℃$. Spectra for various standard reference compounds are also displayed for comparison.
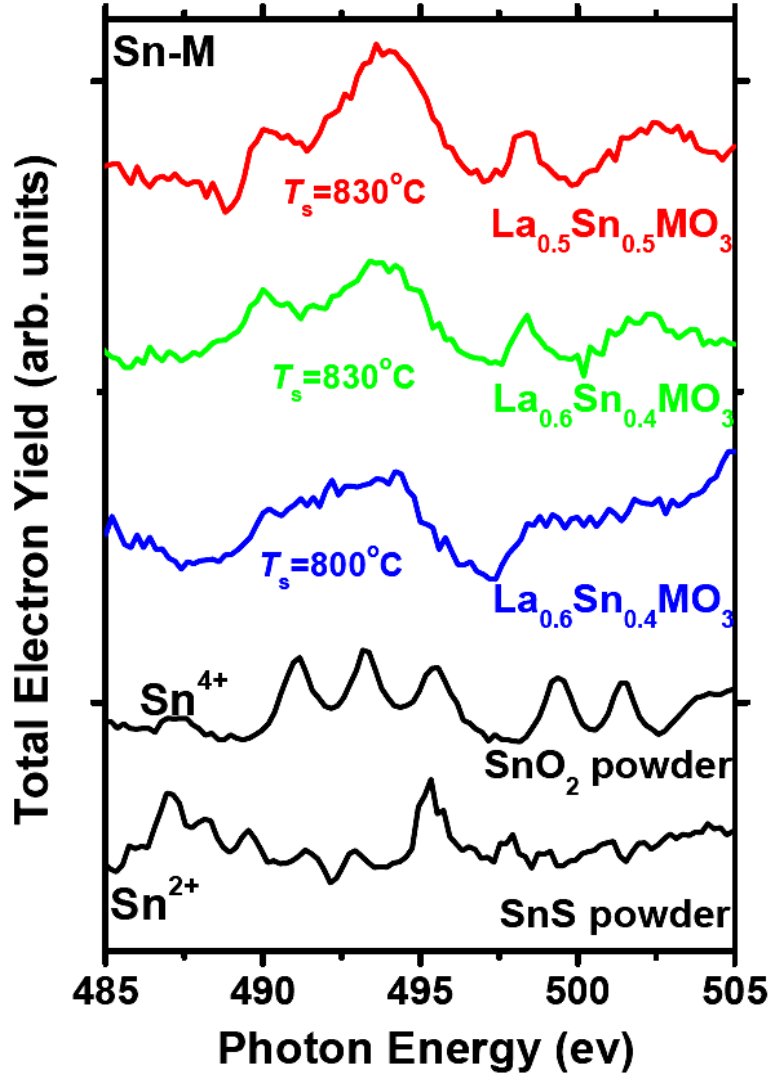
Figure 5.16: The x-ray absorption spectra of Sn for $La_{1-x}Sn_xMnO_3$ ($x=0.4-0.5$) films. These three samples were all fabricated at $T_s \geqq 800°C$.

Fig. 5.17 displayed the x-ray absorption fluorescence yield spectra of $La_{0.9}Sn_{0.1}MnO_3$, $La_{0.7}Ce_{0.3}MnO_3$, and $La_{0.7}Ca_{0.3}MnO_3$ measured at 30K [73], respectively. It revealed that the hole concentration is drastically decreased even for the case of $La_{0.9}Sn_{0.1}MnO_3$ when comparing with $La_{0.7}Ce_{0.3}MnO_3$ and $La_{0.7}Ca_{0.3}MnO_3$. The suppression of hole concentration may be suggestive of the achievement of electron doping via replace the La^{3+} ions by the Sn^{4+} ions. However, it would need further studies to pin down the real physical mechanism.
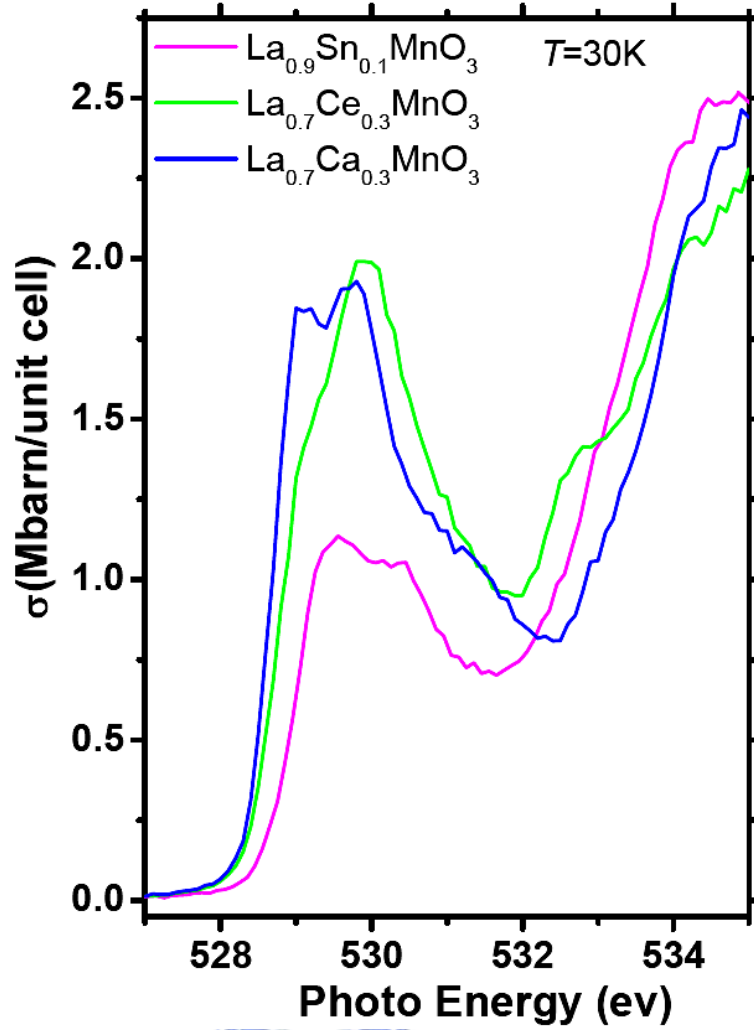
Fig. 5.17: Comparison of the x-ray absorption fluorescence yield spectra of $La_{0.9}Sn_{0.1}MnO_3$, $La_{0.7}Ce_{0.3}MnO_3$, and $La_{0.7}Ca_{0.3}MnO_3$ measured at 30K, respectively (reproduced from Ref. [73]).

The x-ray absorption fluorescence yield spectra with the self-absorption correction were carried out for the LSnMO samples for the further investigation. There are three main peaks observed over the range of $525-555$ eV. The first peak at about 529.7 eV is assigned to be associated with O $2p$-Mn $3d$ hybridization, the second one at about 535.5 eV is associated with O $2p$-La $5d$ and O $2p$-Sn $3d$ hybridization, and the third one at about 543.4 eV comes from O $2p$-Mn $4sp$ hybridization. The first peak is generally believed to be the one dominating the electric transport and magnetic properties, since the O $2p$-Mn $3d$ coupling is

intimately related to the double-exchange mechanism [25]. Park *et al.* [111－113] proposed that, in the case of $La_{0.7}Sr_{0.3}MnO_3$, the $e_{g\uparrow}$ state and $t_{2g\downarrow}$ state will split, as shown in Fig. 5.18, as a result of the double exchange interaction at low temperature. However, the x-ray absorption fluorescence yield spectra of the LSnMO films obtained at $T=300$ K and 30 K, as illustrated in Fig. 5.19－5.22, do not display obvious splitting at either $T=300$ K or $T=30$ K .Whether this is due to the lack of DE interaction for this system or other physics remains to be clarified. The x-ray absorption fluorescence yield spectra of $La_{1-x}Sn_xMnO_3$ ($x=0.1\sim0.4$) taken in the ferromagnetic state (30K) are plotted together for comparison. Despite that the LSnMO samples all exhibit no sign of metal insulator transition, the unoccupied state (hole) are decreased with the increasing doping amount of Sn, suggesting that the electron doping did prevail as expected.
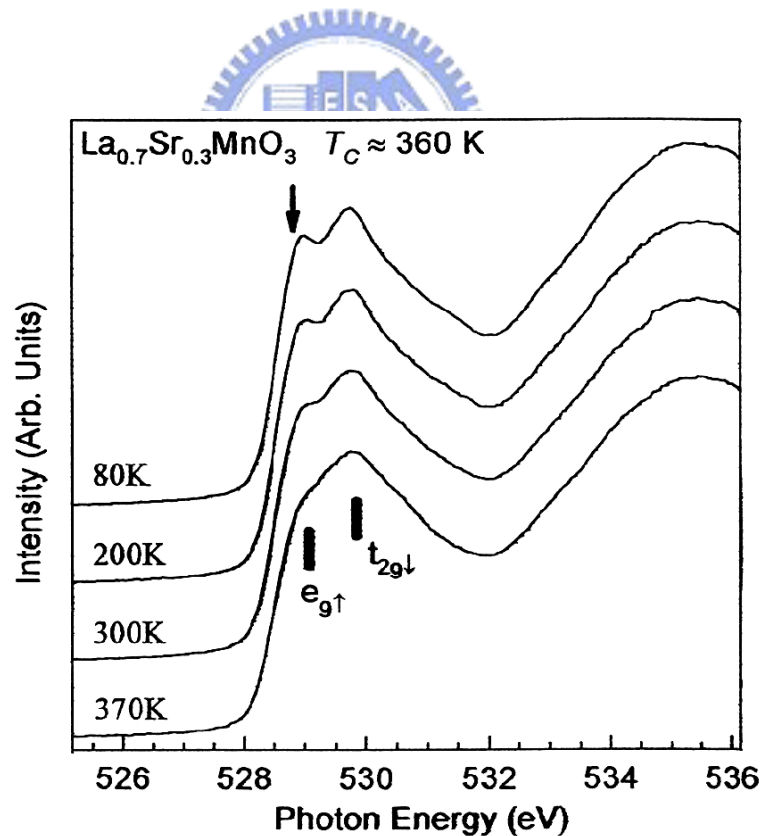
Fig. 5.18: Temperature-dependent O 1*s* XAS spectra of the $La_{0.7}Sr_{0.3}MnO_3$ on STO substrate (reproduced from Ref. [113]).
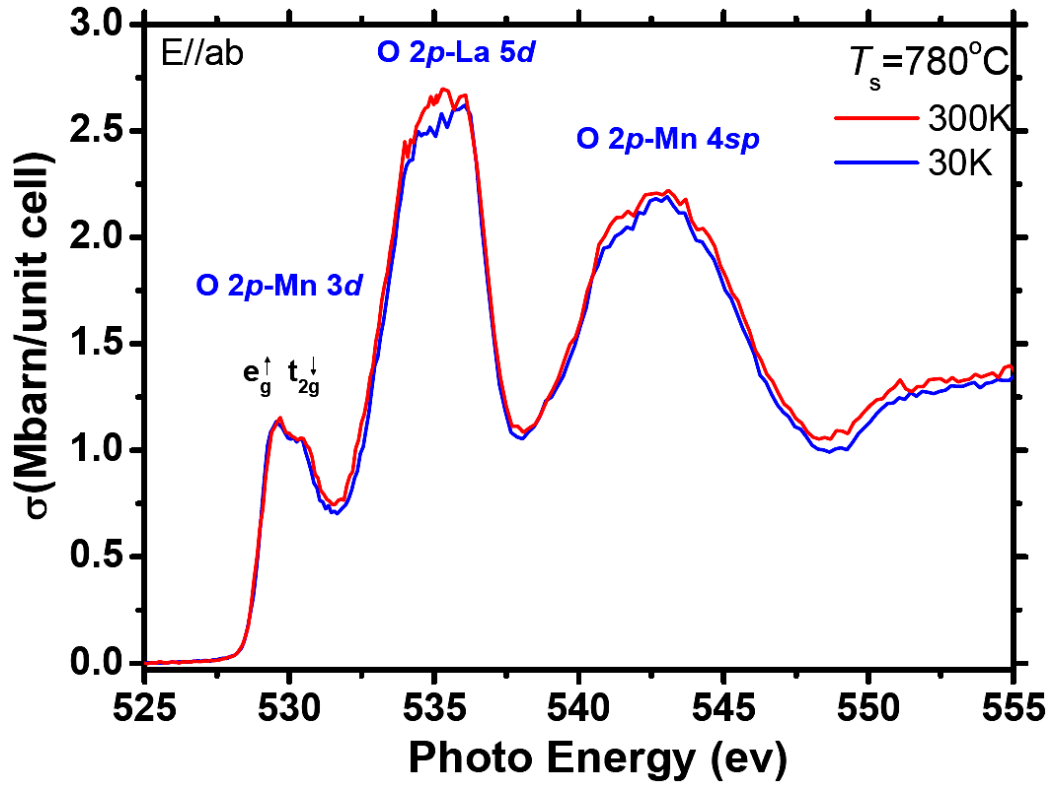
Figure 5.19: The O K-edge XAS taken at 300 K and 30 K for $La_{0.9}Sn_{0.1}MnO_3$ films deposited at $T_s=780℃$.
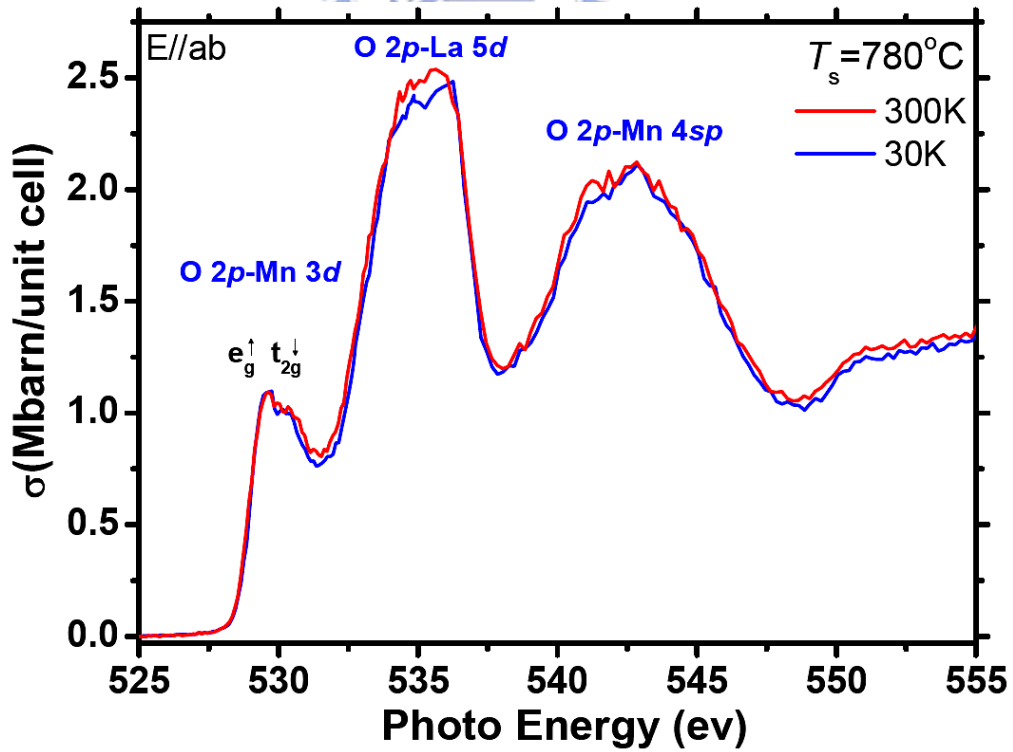
Figure 5.20: The O K-edge XAS taken at 300 K and 30 K for $La_{0.8}Sn_{0.2}MnO_3$ films deposited at $T_s=780℃$.
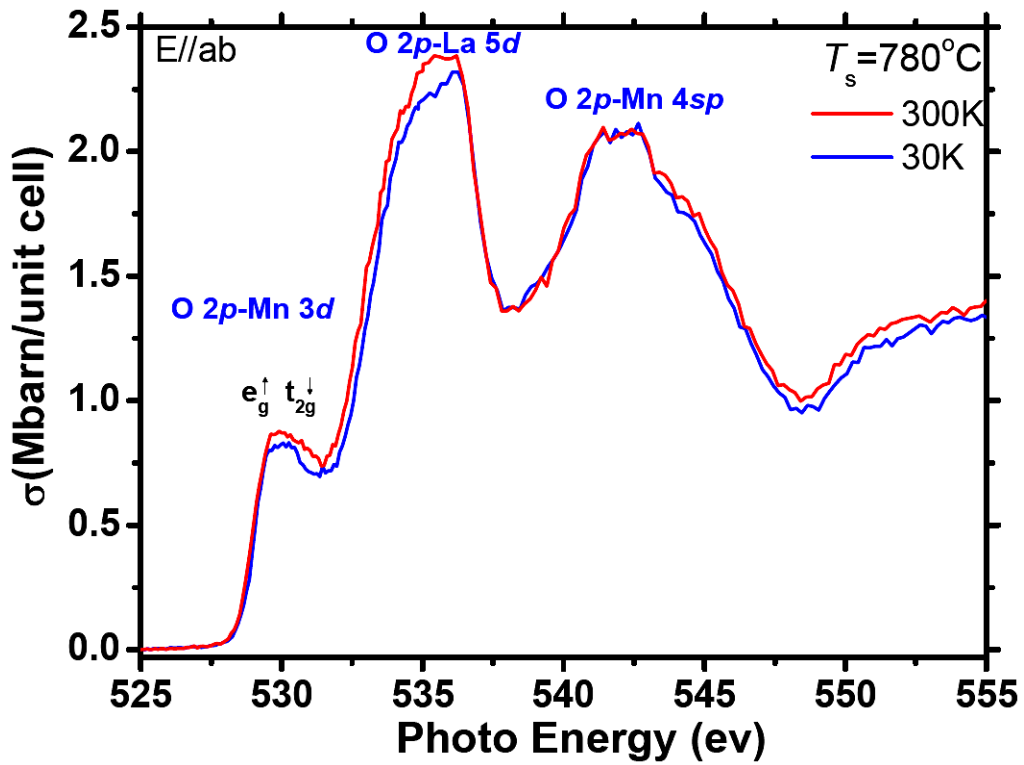
Figure 5. 21: The O K-edge XAS taken at 300 K and 30 K for $La_{0.7}Sn_{0.3}MnO_3$ films deposited at T_s=780℃.
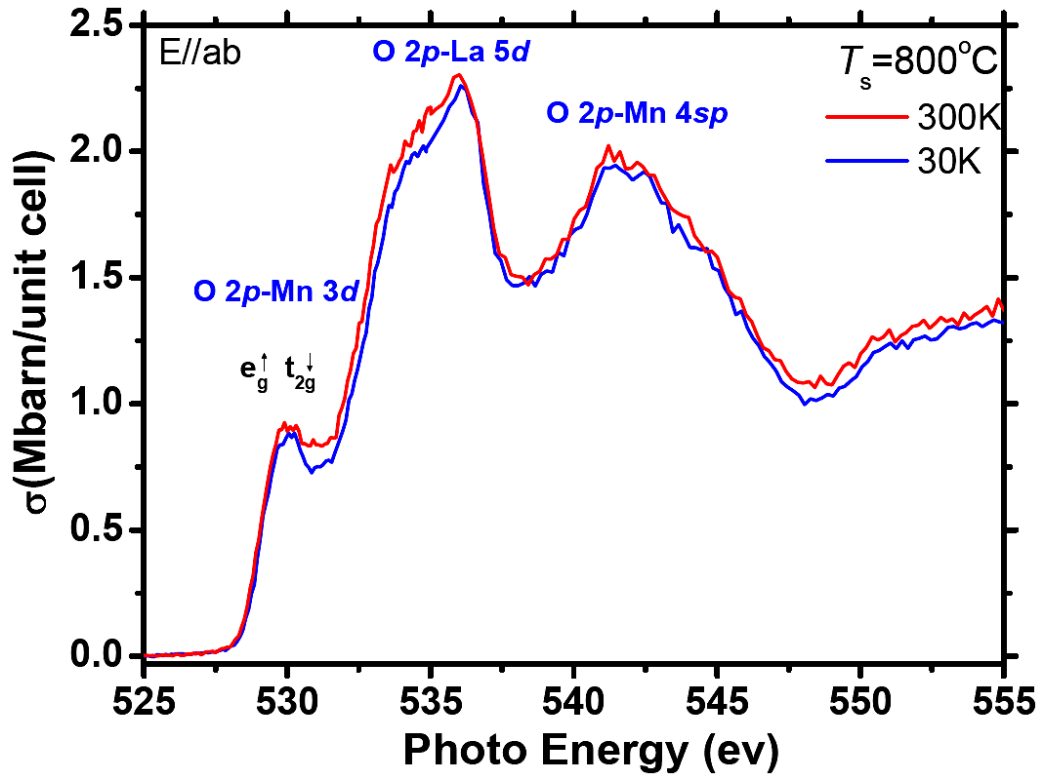
Figure 5.22: The O K-edge XAS taken at 300 K and 30 K for $La_{0.6}Sn_{0.4}MnO_3$ films deposited at T_s=800℃.
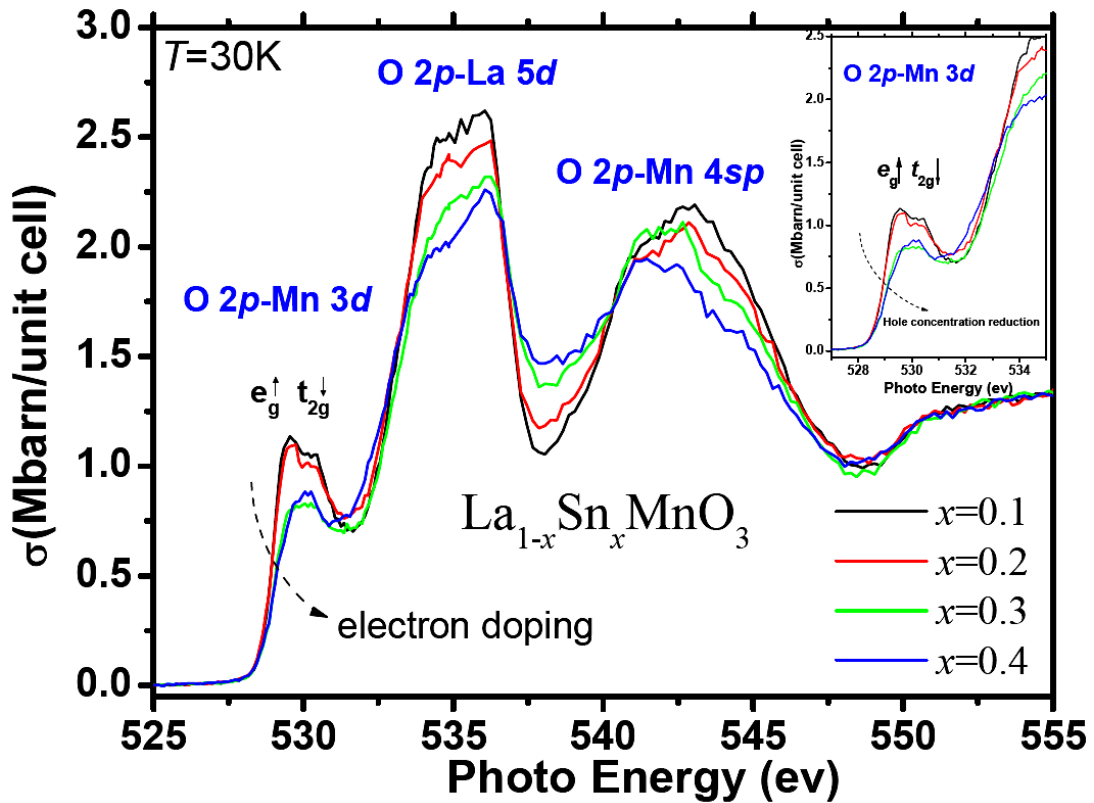
Figure 5.23: The x-ray absorption fluorescence yield spectra of $La_{1-x}Sn_xMnO_3$ (x=0.1~0.4) in the ferromagnetic phase taken at 30 K.

5.7 Phase diagram of $La_{1-x}Sn_xMnO_3$

In this section, we would like to discuss about the magnetic phase diagram of LSnMO and the comparison with other CMR manganites. Fig. 5.24 displays the phase diagram of magnetic transition as a function of Sn doping for $La_{1-x}Sn_xMnO_3$ (x=0.1~0.4) prepared on $LaAlO_3$ substrates. The LSnMO thin films all exhibit ferromagnetic insulator behavior. We believe that the insulator behavior is resulted from the large ionic size mismatch between La^{3+} and Sn^{4+}, leading to severe structure disorder and hindering the long range magnetic ordering [106]. Recently, the family of Pr-doped manganite $La_{1-x}Pr_xMnO_3$ ($0 \leq x \leq 1$) has been systematically investigated by Dyakonov *et al*. [114]. They claimed that a decrease of the

A-site cation radius would stabilize the static Jahn-Teller distortions and lead to a weakening of ferromagnetic coupling. For ABO_3-type manganites, the canted spin phase was found to be stabilized more rebustly for the A-site with smaller radius [115]. The concept addressed by Dyakonov *et al.* may represent another hint of the possible mechanism of the ferromagnetic-insulator behavior in our LSnMO thin films. However, if this argument is true, the achievement of the "real" electron-doped manganites would be very difficult since the ionic size tetravalent ions are always much smaller than that of trivalent ions, leading to the A-site with smaller radius.

For further discussion, the other electron doping manganites investigated by many other researchers are listed in Table 5.2 for comparison. The correspondent phase diagram is depicted in Fig. 5. 25. It is evident that the results of electron doping manganites $La_{1-x}A_xMnO_3$ (A＝Ce, Sn, Te, Pr) appeared to have serious discrepancy. In addition, attempts to anneal the samples all led to the increasing of T_C, with behaviors resembling that La-deficient La_xMnO_3 systems (see the solid red symbols in Fig. 5. 25). Fig. 5.26 displays the magnetic phase diagrams of $La_{1-x}Sn_xMnO_3$ and $La_{1-x}Ca_xMnO_3$ together for comparison. The results show that, unlike that in the hole-doped side, the Sn-doped manganites exhibit a monotonous ferromagnetic insulator behavior up to $x＝0.4$. It will be interesting to see if the lack of ferromagnetic metal is inherent in systems with severely disrupted double-exchange interactions.
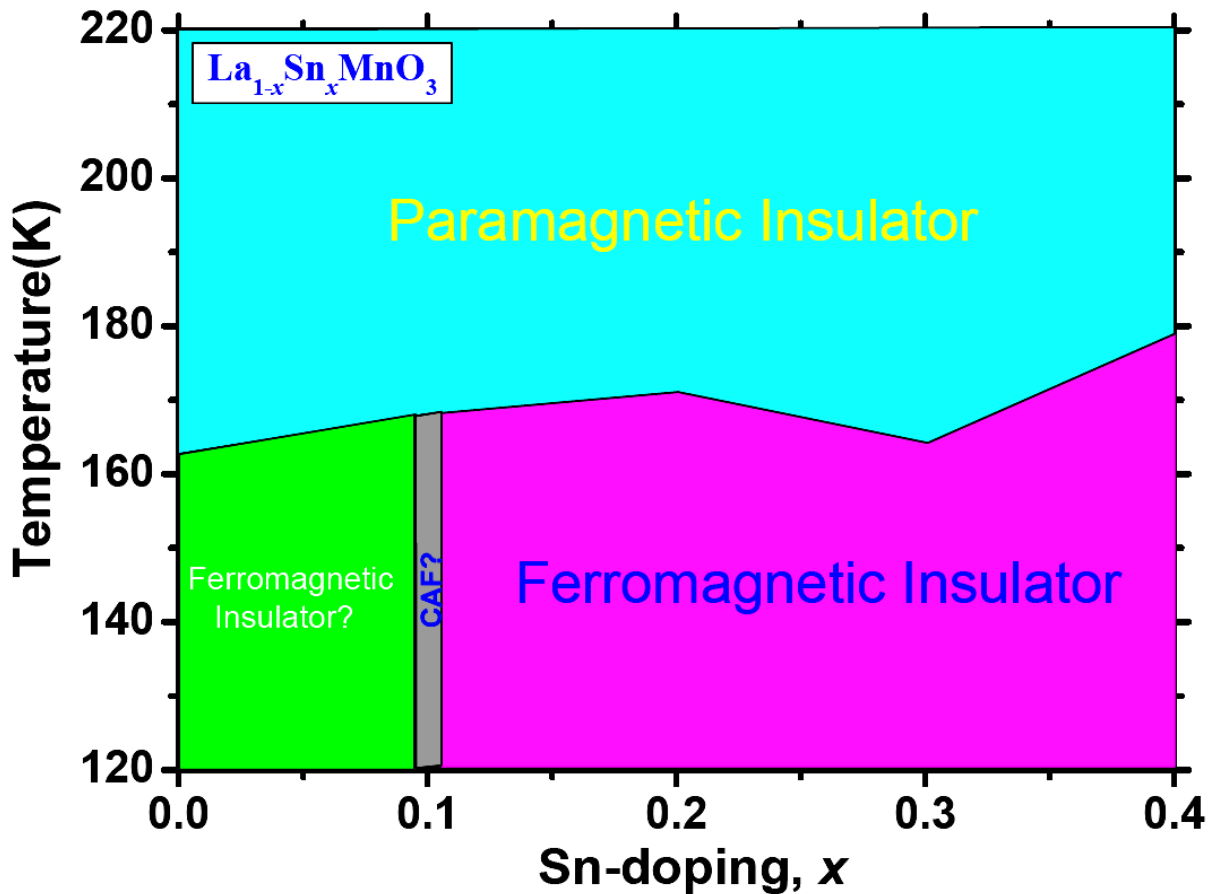
Figure 5.24: The magnetic phase diagram of LSnMO prepared on LaAlO$_3$ substrates. The

LSnMO thin films all reveal ferromagnetic insulator behavior.

Electron-doping manganites	Doping level (x); Curie temperature(T_C); Phases(FM, FI)				
L$_{1-x}$Ce$_x$MnO$_3$	$x=0.05$	$x=0.10$	$x=0.15$	$x=0.20$	$x=0.30$
Mitra *et al.*	$T_C=109$ K	$T_C=148$ K	$T_C=195$ K	$T_C=231$ K	$T_C=269$ K
(film)[66]	**FM**	**FM**	**FM**	**FM**	**FM**
L$_{1-x}$Ce$_x$MnO$_3$		$x=0.1$			$x=0.30$
Kawai *et al.*	✕	$T_C=188$ K	✕	✕	$T_C=174$ K
(film)[75$-$76]		**FI**			**FI**

$L_{1-x}Ce_xMnO_3$			$x=0.30$		
Chang *et al.*	✕	✕	$T_C=260$ K	✕	(film)
[72−73, 116]			**FM**		
$L_{1-x}Sn_xMnO_3$	$x=0.1$	$x=0.2$	$x=0.3$	$x=0.4$	$x=0.5$
our work	$T_C=168$ K	$T_C=171$ K	$T_C=164$ K	$T_C=179$K	Mixed
(film on LAO)	**FI**	**FI**	**FI**	**FI**	phase
$L_{1-x}Sn_xMnO_3$	$x=0.1$	$x=0.2$	$x=0.3$		
our work	$T_C=150$ K	$T_C=165$ K	$T_C=175$ K	✕	✕
(film on STO)	**FI**	**FI**	**FI**		
*$L_{1-x}Sn_xMnO_3$	$x=0.04$	$x=0.07$	$x=0.11$	$x=0.18$	
Guo *et al.*	$T_C=219$ K	$T_C=275$ K	$T_C=296$ K	$T_C=325$ K	(film)
[92]	**FM**	**FM**	**FM**	**FM**	
*$L_{1-x}Te_xMnO_3$	$x=0.04$	$x=0.1$	$x=0.15$	$x=0.20$	
Tan *et al.*	$T_C=201$ K	$T_C=240$ K	$T_C=255$ K	$T_C=255$ K	(bulk)
[77−79]	**FM**	**FM**	**FM**	**FM**	
*$L_{1-x}Te_xMnO_3$		$x=0.1$	$x=0.15$		
Tan *et al.*	✕	$T_C=249$ K	$T_C=254$ K	✕	(film)
[80]		**FM**	**FM**		
**$L_{1-x}Pr_xMnO_3$			$x=0.3$		
Chen *et al.*	✕	✕	$T_C=210$ K	✕	(bulk)
[82]			**FM**		

Table 5.2: The comparisons of the electron-doping manganites on the doping level (x), Curie temperature (T_C), and phases. FM: ferromagnetic metal. FI: ferromagnetic insulator; ✕: not available. *Post-annealed in O_2; **Post-annealed in Ar.
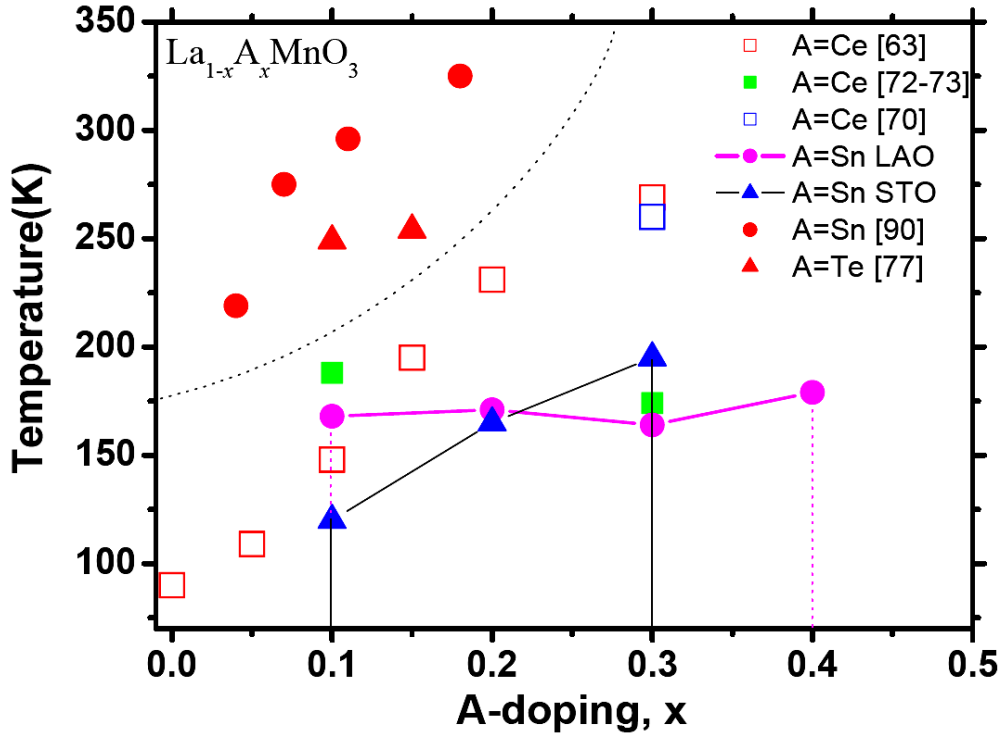
Figure 5.25: The magnetic phase diagram of our LSnMO prepared on LaAlO$_3$ and SrTiO$_3$ substrates. The electron doped manganites proposed by other researchers are reproduced for comparison.
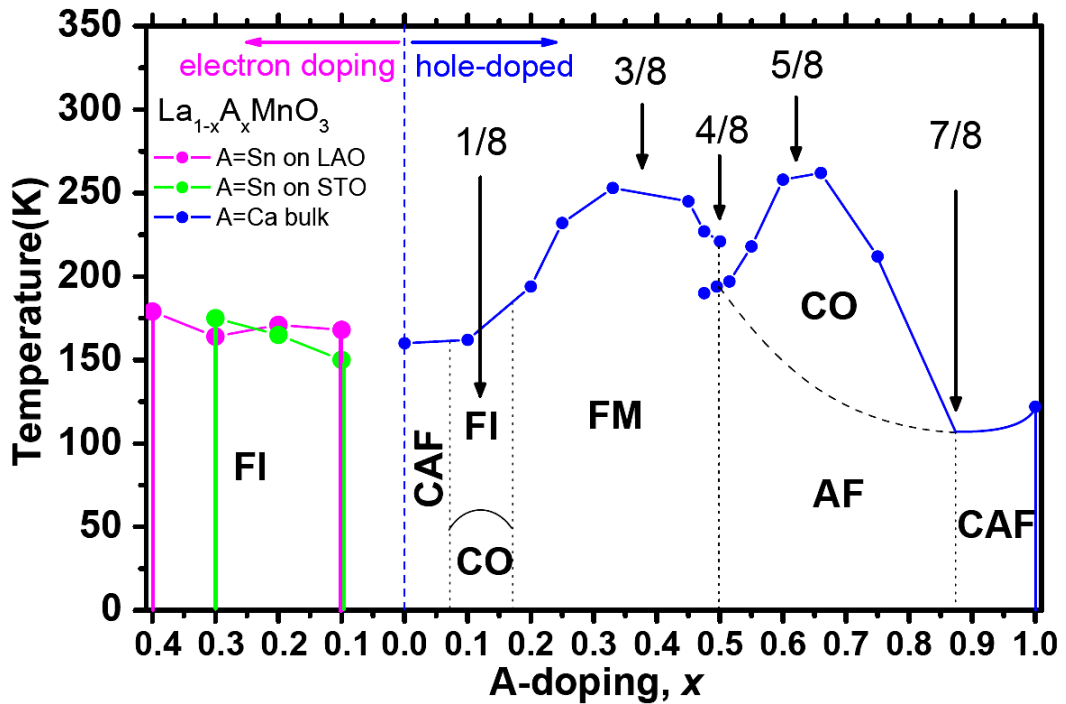
Figure 5.26: The magnetic phase diagram of La$_{1-x}$Sn$_x$MnO$_3$ compare with La$_{1-x}$Ca$_x$MnO$_3$.

5.8 Summary

In summary, we have systematically prepared Sn doped manganites $La_{1-x}Sn_xMnO_3$ ($x=$ 0.1~0.5) films despite the tremendous challenges put forth by the large ionic size difference between La^{3+} and Sn^{4+}. The additional magnetic transition near 44K though has been attributed to depinning of magnetic domain walls at specific temperature and magnetic field or the magnetic contribution of the off-stoichiometry perovskite manganites, we argue, from the evidences of XRD, $M(T)$ and TEM, that it is very likely a result of Mn_3O_4 phase formed at high deposition temperature and/or high Sn-doping level. Consequently, the limit of doping level achievable in single-phase $La_{1-x}Sn_xMnO_3$ can only be up to $x=0.4$. We believed that the ionic size between La^{3+} and Sn^{4+} and deposition temperature (T_s) are playing an important role in this matter. The Mn L-edge x-ray absorption spectroscopy analysis shows features of Mn^{3+}/Mn^{2+} mixed-valence states, as well as the elimination of the unoccupied state observed from the O K-edge XAS, suggesting the realization of electron-doping effect. The phase diagram of the $La_{1-x}Sn_xMnO_3$ reveals that the properties of the electron-doped manganites are not symmetric to their hole-doped counterparts, indicating the prominent role of double-exchange interaction in obtaining ferromagnetic-metal state in manganites.

Chapter 6

Summary

In this dissertation, the magnetotransport properties, electronic structure, and microstructure of tin-doped manganite films have been systematically investigated. Some eminent issues in the regime of the substitutions of the La^{3+} by the tetravalent ions manganites have also been clarified. The experimental results indeed supply some conclusive evidences for the further understanding of this field.

We have successfully prepared single phase epitaxial $La_{0.7}Sn_{0.3}MnO_3$ films on $SrTiO_3$ substrates despite the tremendous challenges put forth by the large ionic size difference between La^{3+} and Sn^{4+}. The *ex-situ* post-deposition annealing not only improve the structure of AD-film and gives rise to epitaxial c-axis oriented $La_{0.7}Sn_{0.3}MnO_3$ films but also leads to over room temperature CMR effects. Both the as deposited and post annealed $La_{0.7}Sn_{0.3}MnO_3$ films display significant features of spin-glass that would need further studies for a full understanding. Mn L-edge x-ray absorption spectroscopy analysis shows features of Mn^{3+}/Mn^{2+} mixed-valence states, indicating that the tetravalent Sn ions indeed results in electron-doping into e_g band of Mn.

In addition, we also presented systematic investigations on one of the highly anticipated electron-doped CMR materials. Single-phase $La_{0.7}Sn_{0.3}MnO_3$ thin films were grown on

LaAlO$_3$ substrates by pulsed laser deposition. The as-deposited La$_{0.7}$Sn$_{0.3}$MnO$_3$ films are ferromagnetic insulators with typical Curie temperature around 150 K. Both the electronic structure revealed by the x-ray absorption spectra (XAS) and the microstructure observed by detailed TEM analyses indicate that in this case the doped Sn-element is indeed acting as the tetravalent ion uniformly distributed in the LaMnO$_3$ parent compound. The large internal strain originated from the marked ion size difference between the doped Sn^{4+} and substituted La^{3+} ions, however, is believed to hinder the long-range itinerancy of the carriers, hence preventing it from becoming metallic. Unfortunately, due to the insulating nature of these as-deposited La$_{0.7}$Sn$_{0.3}$MnO$_3$ films, it is not clear whether it is indeed "n-type" electron-doped manganite. *Ex-situ* annealing in oxygen and argon both drive the films to exhibit insulator-metal transition with hole-doped characteristics when becoming ferromagnetic. The transition temperatures, however, are different for films annealed in different environments, presumably due to the final phase and compositions obtained. From the results of magnetoresistance measurements and XAS, it is suggestive that La$_{0.7}$Sn$_{0.3}$MnO$_3$ films annealed in argon causes the significant loss of Sn and results in La-deficient phase. Whereas those annealed in oxygen appeared to form some kind of Sn-O compound, turning the films into La-deficient manganite, albeit with some excessive oxygen. We emphasize that the existence of tetravalent Sn from XAS should not be taken as the sole evidence of achieving electron-doped manganite. As being clearly demonstrated in this study, it may just reveal the emergence of SnO$_2$.

Furthermore, we have systematically prepared Sn doped manganites La$_{1-x}$Sn$_x$MnO$_3$ (x＝ 0.1－0.5) films despite the tremendous challenges put forth by the large ionic size difference between La^{3+} and Sn^{4+}. The additional magnetic transition might be due to depinning of magnetic domain walls at specific temperature and magnetic field or the magnetic contribution of the off-stoichiometry perovskite manganites. Furthermore, from the results of

XRD, $M(T)$ and TEM, the observation of the additional magnetic transition near 44K in $M(T)$ is evidenced to be resulted from the magnetic contribution of Mn_3O_4. Therefore, the doping level of the $La_{1-x}Sn_xMnO_3$ may only be up to $x=0.4$. We believed that the ionic size between La^{3+} and Sn^{4+}, deposition temperature (T_s) and Sn doping content (x) are playing an important role in the solubility of Sn in the $LaMnO_3$ perovskite. The Mn L-edge x-ray absorption spectroscopy analysis shows features of Mn^{3+}/Mn^{2+} mixed-valence states, as well as the elimination of the unoccupied state observed from the O K-edge XAS, suggesting the realization of electron-doping effect. The phase diagram of the $La_{1-x}Sn_xMnO_3$ reveals that the properties of the electron-doped manganites are not symmetric to their hole-doped counterparts.

Reference

[1] G. H. Jonker and J. H. van Santen, Physica **16**, 337 (1950).

[2] Y. Tokura and N. Nagaosa, Science **288**, 462 (2000).

[3] E. Dagotto, "*Nanoscale Phase Separation and Colossal Magnetoresistance*" (Springer, 2003).

[4] Y. Shimakawa, Y. Kubo, and T. Manako, Nature **379**, 53 (1996).

[5] P. Schiffer, A. P. Ramirez, W. Bao, and S.-W. Cheong, Phys. Rev. Lett. **75**, 3336 (1995).

[6] K. Ghosh, R. L. Greene, S. E. Lofland, S. M. Bhagat, S. G. Karabashev, D. A. Shulyatev, A. A. Arsenov, and Y. Mukovskii, Phys. Rev. B **58**, 8206 (1998).

[7] H. L. Ju, J. Gopalakrishnan, J. L. Peng, Qi Li, G. C. Xiong, T. Venkatesan, and R. L. Greene, Phys. Rev. B **51**, 6143 (1995).

[8] A. Urushibara, Y. Moritomo, T. Arima, A. Asamitsu, G. Kido, and Y. Tokura, Phys. Rev. B **51**, 14103 (1995).

[9] J. M. De Teresa, M. R. Ibara, J. Blasco, J. Garcia, C. Marquina, P. A. Algarabel, Z. Arnold, K. Kamenev, C. Ritter, and R. von Helmolt, Phys. Rev. B **54**, 1187 (1996).

[10] M. Rajeswari, R. Shreekala, A. Goyal, S. E. Lofland, S. M. Bhagat, K. Ghosh, R. P. Sharma, R. L. Greene, R. Ramesh, T. Venkatesan, and T. Boettcher, Appl. Phys. Lett. **73**, 2672 (1998).

[11] R. von Helmolt, J. Wecker, B. Holzapfel, L. Schultz, and K. Samwer, Phys. Rev. Lett. **71**, 2331 (1993).

[12] S. Jin, T. H. Tiefel, M. McCormack, R. A. Fastnacht, R. Ramesh, and L.H. Chen, Science **264**, 413 (1994).

[13] J. M. D. Coey, M. Viret, L. Ranno, and K. Ounadjela, Phys. Rev. Lett. **75**, 3910 (1995).

[14] C. Zener, Phys. Rev. **82**, 403 (1951).

[15] P. W. Anderson, and H. Hasegawa, Phys. Rev. **100**, 675 (1955).

[16] A. J. Millis, P. B. Littlewood, and B. I. Shraiman, Phys. Rev. Lett. **74**, 5144 (1995).

[17] H. Y. Hwang, S.-W. Cheong, P. G. Radaelli, M. Marezio, and B. Batlogg, Phys. Rev. Lett. **75**, 914 (1995).

[18] T. Kanki, H. Tanaka, and T. Kawai, Solid State Commun. **114**, 267 (2000).

[19] T. Kanki, H. Tanaka, and T. Kawai, Phys. Rev. B **64**, 224418 (2001).

[20] T. Kanki, H. Tanaka, and T. Kawai, J. Appl. Phys. **93**, 4718 (2003).

[21] T. Kanki, L. Run-Wei, Y. Naitoh, H. Tanaka, T. Matsumoto, and T. Kawai, Appl. Phys. Lett. **83**, 1184 (2003).

[22] T. Kanki, Y. G. Park, H. Tanaka, and T. Kawai, Appl. Phys. Lett. **83**, 4860 (2003).

[23] H. Tanaka, J. Zhang, and T. Kawai, Phys. Rev. Lett. **88**, 027204 (2002).

[24] J. Zhang, H. Tanaka, T. Kanki, J.-H. Choi, and T. Kawai, Phys. Rev. B **64**, 184404 (2001).

[25] S. J. Liu. "The magnetoresistive and transport properties of CrO_2 and $La_{2/3}(Sr,Ca)_{1/3}MnO_3$ films". Ph.D. thesis, Department of Electrophysics, National Chiao Tung University, 1001 Ta Hsueh Rd., Hsinchu, Taiwan 30050 (2002).

[26] R. B. Praus, B. Leibold, G. M. Gross, and H.-U. Habermeier, Appl. Surf. Sci. **138**, 40 (1999).

[27] T. Y. Koo, S. H. Park, K.-B. Lee, and Y. H. Jeong, Appl. Phys. Lett. **71**, 977 (1997).

[28] P. Murugavel, J. H. Lee, Jong-Gul Yoon, T. W. Noh, J.-S. Chung, M. Heu and S. Yoon, Appl. Phys. Lett. **82**, 1908 (2003)

[29] C. Ritter, M. R. Ibarra, J. M. De Teresa, P. A. Algarabel, C. Marquina, J. Blasco, J. Garcı´a, S. Oseroff , and S-W. Cheong, Phys. Rev. B **56**, 8902 (1996).

[30] V. L. Joseph Joly, P. A. Joy, and S. K. Date, J. Magn. Magn. Mater. **247**, 316 (2002).

[31] S. Das and P. Mandal, Z. Phys. B **104**, 7 (1997); P. Mandal and S. Das, Phys. Rev. B **56**, 15073 (1997).

[32] A. Gupta, T. R. McGuire, P. R. Duncombe, M. Rupp, J. Z. Sun, W. J. Gallagher, and

Gang Xiao, Appl. Phys. Lett. **67**, 3494 (1995).

[33] S. Pingard, H. Vincent, J. P. Senateur, J. Pierre, and A. Abrutis, J. Appl. Phys, **82**, 4445 (1997).

[34] C. Zener, Phys. Rev. **81**, 440 (1951).

[35] C. Zener, Phys. Rev. **83**, 299 (1951).

[36] P. G. de Genes, Phys. Rev. **118**, 141 (1960).

[37] Elbio Dagotto, Takashi Hotta, and Adriana Moreo, Physics Reports **344**, 153 (2001).

[38] Yoshinori Tokura. (Ed.), "*Colossal Magnetoresistance Oxides*", (Gordon & Breach, London, 2000).

[39] A. J. Millis, Boris I. Shraiman, and R. Mueller, 77, 175 (1996).

[40] G. H. Jonker and J. H. Van Santen, Physica (Amsterdam) **16**, 337 (1950); G. H. Jonker, *ibid.* **17**, 707 (1956).

[41] E. O. Wollan and W. C. Koehler, Phys. Rev. **100**, 545 (1955).

[42] H. L. Yakel, Jr., Acta Crystallogr. **8**, 394 (1955).

[43] J. B. A. A. Elemans, B. Van Laar, K. R. Van Der Veen, and B. O. Loopstra, J. Solid State Chem. **3**, 238 (1971).

[44] B. C. Tofield and W. R. Scott, J. Solid State Chem. **10**, 183 (1974).

[45] J. A. M. van Roosmalen, E. H. P. Cordfunke, R. B. Helmholdt, and H. W. Zandbergen, J. Solid State Chem. **110**, 100 (1994).

[46] V. Ferris, L. Brohan, M. Ganne, and M. Tournoux, Eur. J. Solid State Inorg. Chem. **32**, 131 (1995).

[47] J. W. Lynn, R. W. Erwin, J. A. Borchers, Q. Huang, A. Santoro, J. L. Peng, and Z. Y. Li, Phys. Rev. Lett. **76**, 4046 (1996).

[48] Q. Huang, A. Santoro, J. W. Lynn, R. W. Erwin, J. A. Borchers, J. L. Peng, and R. L. Greene, Phys. Rev. B **55**, 14987 (1997).

[49] F. Moussa, M. Hennion, J. Rodriguez-Carvajal, H. Moudden, L. Pinsard, and A.

Revcolevschi, Phys. Rev. B **54**, 15149 (1996).

[50] S. de Brion, F. Ciorcas, G. Chouteau, P. Lejay, P. Radaelli, and C. Chaillout, Phys. Rev. B **59**, 1304 (1999).

[51] J. Z. Sun, L. Krusin-Elbaum, A. Gupta, Gang Xiao, and S. S. P. Parkin, Appl. Phys. Lett. **69**, 1002 (1995).

[52] S. Pignard, H. Vincent, J. P. Se´nateur, K. Fröhlich, and J. Šouc, Appl. Phys. Lett. **73**, 999 (1998).

[53] T. R. McGuire, A. Gupta, P. R. Duncombe, M. Rupp, J. Z. Sun, R. B. Laibowitz, W. J. Gallagher, and Gang Xiao, J. Appl. Phys, **79**, 4549 (1996).

[54] R. Suryanarayanan, J. Berthon, I. Zelenay, B. Martinez, X. Obradors, S. Uma and E. Gmelin, J. Appl. Phys, **83**, 5264 (1998).

[55] Y. G. Zhao, M. Rajeswari, R. C. Srivastava, A. Biswas, S. B. Ogale, D. J. Kang, W. Prellier, Zhiyun Chen, R. L. Greene, and T. Venkatesan, J. Appl. Phys, **86**, 6327 (1999).

[56] Sam Jin Kim, Chul Sung Kim, Seung-Iel Park, and Bo Wha Lee, J. Appl. Phys, **89**, 7416 (2001).

[57] Q. Qian, T. A. Tyson, C. Dubourdieu, A. Bossak, J. P. Se´nateur, M. Deleon, J. Bai, G. Bonfait, and J. Maria, J. Appl. Phys, **92**, 4518 (2002).

[58] Keikichi Nakamura, and Keiichi Ogawa, J. Appl. Phys, **92**, 6684 (2002).

[59] P A Joy, C Raj Sankar and S K Date, J. Phys.: Condens. Matter **14**, 4985 (2002).

[60] P A Joy, C Raj Sankar and S K Date, J. Phys.: Condens. Matter **14**, L663 (2002).

[61] Bjørn C. Hauback, Helmer Fjellvåg, and Natsuko Sakai, J. Solid State Chem. **124**, 43 (1996).

[62] Anthony Arulraj, R. Mahesh, G. N. Subbanna, R. Mahendiran, A. K. Raychaudhuri, and C. N. R. Rao, J. Solid State Chem. **124**, 87 (1996).

[63] F. Prado, R. D. SaH nchez, A. Caneiro, M. T. Causa, and M. Tovar, J. Solid State Chem. **146**, 418 (1999).

[64] A. Urushibara, Y. Moritomo, T. Arima, A. Asamitsu, G. Kido, and Y. Tokura, Phys. Rev. B 51, 14103 (1995).

[65] A. P. Ramirez, P. Schiffer, S-W. Cheong, C. H. Chen, W. Bao, T. T. M. Palstra, P. L. Gammel, D. J. Bishop, and B. Zegarski, Phys. Rev. Lett. **76**, 3188 (1996).

[66] P. Raychaudhuri, C. Mitra, P. D. A. Mann, and S. Wirth, J. Appl. Phys. **93**, 8328 (2003).

[67] C. Mitra, Z. Hu, P. Raychaudhuri, S. Wirth, S. I. Csiszar, H. H. Hsieh, H.-J. Lin, C. T. Chen, and L. H. Tjeng, Phys. Rev. B **67**, 092404 (2003).

[68] C. Mitra, P. Raychaudhuri, K. Dörr, K.-H. Müller, L. Schultz, P. M. Oppeneer, and S. Wirth, Phys. Rev. Lett. **90**, 017202 (2003).

[69] C. Mitra, G. Köbernik, K. Dörr, K.-H. Müller, L. Schultz, P. Raychaudhuri, R. Pinto, and E. Wieser, J. Appl. Phys. **91**, 7715 (2002).

[70] C. Mitra, P. Raychaudhuri, G. Köbernik, K. Dörr, K.-H. Müller, L. Schultz, and R. Pinto, Appl. Phys. Lett. **79**, 2408 (2001).

[71] C. Mitra, P. Raychaudhuri, J. John, S. K. Dhar, A. K. Nigam, and R. Pinto, J. Appl. Phys. **89**, 524 (2001).

[72] W. J. Chang, C. C. Hsieh, J. Y. Juang, K. H. Wu, T. M. Uen, Y. S. Gou, C. H. Hsu, and J.-Y. Lin, J. Appl. Phys. **96, 4357** (2004).

[73] W. J. Chang, J. Y. Tsai, H.-T. Jeng, J.-Y. Lin, Kenneth Y.-J. Zhang, H. L. Liu, J. M. Lee, J. M. Chen, K. H. Wu, T. M. Uen, Y. S. Gou, and J. Y. Juang, Phys. Rev. B **72**, 132410 (2005).

[74] T. Yanagida, T. Kanki, B. Vilquin, H. Tanaka, and T. Kawai, Solid State Comm. **129**, 785 (2004).

[75] Takeshi Yanagida, Teruo Kanki, Bertrand Vilquin, Hidekazu Tanaka, and Tomoji Kawai, Phys. Rev. B **70**, 184437 (2004).

[76] Takeshi Yanagida, Teruo Kanki, Bertrand Vilquin, Hidekazu Tanaka, and Tomoji Kawai, J. Appl. Phys.**97**, 033905 (2005)

[77] G. T. Tan, S. Dai, P. Duan, Y. L. Zhou, H. B. Lu, and Z. H. Chen, Phys. Rev. B **68**, 014426 (2003).

[78] G. T. Tan, P. Duan, S. Y. Dai, Y. L. Zhou, H. B. Lu, and Z. H. Chen, J. Appl. Phys. **93**, 5480 (2003).

[79] G. T. Tan, S. Y. Dai, P. Duan, Y. L. Zhou, H. B. Lu, and Z. H. Chen, J. Appl. Phys. **93**, 9920 (2003).

[80] Guotai Tan ,X. Zhang, and Zhenghao Chen, J. Appl. Phys. **95**, 6322 (2004).

[81] J. Yang, W. H. Song, R. L. Zhang, Y. Q. Ma, B. C. Zhao, Z. G. Sheng, G. H. Zheng, J. M. Dai, and Y. P. Sun, Solid State Comm. **131**, 393 (2004).

[82] Ping Duan, Zhenghao Chen, Shouyu Dai, Yueliang Zhou, Huibin Lu, Kuijuan Jin, and Bolin Cheng, Appl. Phys. Lett. **84**, 4741 (2004).

[83] S. Dai, Z. W. Li, A. H. Morrish, X. Z. Zhou, J. G. Zhao, and X. M. Xiong, Phys. Rev. B **55,** 14125 (1997).

[84] Z. W. Li, A. H. Morrish, and J. Z. Jiang, Phys. Rev. B **60,** 10284 (1999).

[85] A. Caneiro, L. Morales, F. Prado, D. G. Lamas, R. D. Sanchez, and A. Serquis, Phys. Rev. B **62,** 6825 (2000).

[86] A. H. Morrish, Z. W. Li, S. Dai, X. Z. Zhou, J. G. Zhao, and X. M. Xiong, Hyp. Interact. 113, 485－492 (1998).

[87] A. I. Shames, E. Rozenberg, G. Gorodetsky, B. Revzin, D. Mogilyanski, J. Pelleg, and I. Felner, J. Magn. Magn. Mater. **203**, 259－261 (1999).

[88] B. Revzin, E. Rozenberg, G. Gorodetsky, J. Pelleg, and I. Felner, J. Magn. Magn. Mater. **215－216**, 204－206 (2000).

[89] Run-Wei Li, Ji-Rong Sun, Zhi-Hong Wang, Shao-Ying Zhang, and Bao-Gen Shen, J. Phys. D: Appl. Phys. **33**, 1982–1984 (2000).

[90] Y. Q. Wang, X. F. Duan, Z. H. Wang, J. R. Sun, and B. G. Shen, Appl. Phys. Lett. **78**, 2479 (2001).

[91] Xiangxin Guo, Shouyu Dai, Yueliang Zhou, Guozhen Yang, and Zhenghao Chen, Appl. Phys. Lett. **75**, 3378 (1999).

[92] X. Guo, Z. Chen, S. Dai, Y. Zhou, R. Li, H. Zhang, B. Shen, and H. Cheng, J. Appl. Phys. **88**, 4758 (2000).

[93] Xiangxin Guo, Zhenghao Chen, Dafu Dui, Yueliang Zhou, H. Z. Huang, H. X. Zhang, Fengqin Liu, Kurash Ibrahim, and Haijie Qian, J. Crystal Growth **219**, 404－408 (2000).

[94] Xiangxin Guo, Shouyu Dai, Yueliang Zhou, Zhenghao Chen, Guozhen Yang, Fengqin Liu, Kurash Ibrahim, and Haijie Qian, Mater. Sci. Eng. B **76**, 18－21 (2000).

[95] J. Gao, S. Y. Dai, and T. K. Li, Phys. Rev. B **67**, 153403 (2003).

[96] J. A. Mydosh, "*Spin Galsses: an Experimental Introduction*", Taylor & Francis, London, 1993.

[97] J. M. De Teresa, M. R. Ibarra, J. García, J. Blasco, C. Ritter, P.A. Algarabel, C. Marquina, and A. del Moral, Phys. Rev. Lett. **76**, 3392 (1996).

[98] M. R. Ibarra, P. A. Algarabel, C. Marquina, J. Blasco, and J. García, Phys. Rev. Lett. **75**, 3541 (1995).

[99] P. G. Radaelli, D. E. Cox, M. Marezio, S.-W. Cheong, P. E. Schiffer, and A.P. Ramirez, Phys. Rev. Lett. **73**, 4488 (1995).

[100] G. J. Chen, Y. H. Chang, and H. W. Hsu, J. Magn. Magn. Mater. **219**, 317 (2000).

[101] K. A. Thomas, P. S. I. P. N. de Silva, L. F. Cohen, A. Hossain, M. Rajeswari, T. Venkateson, R. Hiskes, and J. L. MacManus-Driscoll, J. Appl. Phys. **84**, 3939 (1998).

[102] T. Y. Cheng, C. C. Hsieh, J. Y. Juang, J.-Y. Lin, K. H. Wu, T. M. Uen, Y. S. Gou, and C. H. Hsu, Physica B **365**, 141 (2005).

[103] S. Valencia, A. Gaupp, W. Gudat, Ll. Abad, Ll. Balcells, A. Cavallaro, B. Martínez, and F.J. Palomares, Phys. Rev. B **73**, 104402 (2006).

[104] R. D. Shannon, Acta Crystallogr. A **32,** 752 (1976).

[105] S. Valencia, Ll. Balcells, J. Fontcuberta, and B. Martínez, Appl. Phys. Lett. **82**, 4531 (2003).

[106] T. Y. Cheng, C. W. Lin, L. Chang, C.H. Hsu, J.M. Lee, J.M. Chen, J.-Y. Lin, K. H. Wu, T. M. Uen, Y. S. Gou, and J. Y. Juang, Phys. Rev. B. **74**, 134428 (2006).

[107] L. Morales, F. Prado, A. Caneiro, R. D. Sánchez, and A. Serquis, J. Alloys Compd. **302**, 59－64 (2000).

[108] L. W. Guo, D. L. Peng, H. Makino, K. Inaba, H. J. Ko, K. Sumiyama, and T. Yao, J. Magn. Magn. Mater. **213**, 321－325 (2000).

[109] Y.-H. Huang, F. Luo, Y. Li, Z.-M. Wang, C.-S. Liao, and C.-H. Yan, J. Appl. Phys. **91**, 10218 (2002).

[110] V. G. Prokhorov, Y. P. Lee, K. W. Kim, V. M. Ishchuk, and I. N. Chukanova, Appl. Phys. Lett. **80**, 2353 (2002).

[111] J.-H. Park, C. T. Chen, S-W. Cheong, W. Bao, G. Meigs, V. Chakarian, and Y. U. Idzerda, Phys. Rev. Lett. **76**, 4215 (1996).

[112] J.-H. Park, E. Vescovo, H.-J. Kim, C. Kwon, R. Ramesh, and T. Venkatesan, Nature **392**, 794 (1998).

[113] J.-H. Park, T. Kimura, and Y. Tokura, Phys. Rev. B **58**, 13330 (1998).

[114] V. Dyakonov, F. Bukhanko, V. Kamenev, E. Zubov, S. Baran, T. Jaworska-Gołąb, A. Szytuła, E. Wawrzyńska, B. Penc, R. Duraj, N. Stüsser, M. Arciszewska, W. Dobrowolski, K. Dyakonov, J. Pientosa, O. Manus, A. Nabialek, P. Aleshkevych, R. Puzniak, A. Wisniewski, R. Zuberek, and H. Szymczak, Phys. Rev. B **74**, 024418 (2006).

[115] Y. Tomioka, A. Asamitsu, Y. Moritomo, H. Kuwahara, and Y. Tokura, Phys. Rev. Lett. **74**, 5108 (1995).

[116] J.-Y. Lin, W. J. Chang, J. Y. Juang, T. M. Wen, K. H. Wu, Y. S. Gou, J. M. Lee, and J.

M. Chen, J. Magn. Magn. Mater. **282**, 237–239 (2004).

[117] L. Morales, A. Caneiro, R. D. Sánchez, and D. Vega, J. Magn. Magn. Mater. **226–230**, 823 (2001).

[118] L. Morales, A. Caneiro, D. Vega, R. Zysler, H. Lanza,z and R. C. Mercadery, J. Solid State Chem. 168, 100－109 (2002).

[119] L. Morales, R. Zysler, and A. Caneiro, Physica B **320**, 100－103 (2002).

Biographical notes

Personal Data:

Name: Cheng, Tsan-Yao

Sex: Male

Date of Birth: March 18, 1975

Education:

1993/09 ~ 1997/07 National Chiao-Tung University, Hsinchu, Taiwan BS. degree in
Electrophysics.

2000/09 ~ 2002/07 National Chiao-Tung University, Hsinchu, Taiwan MS. degree in
Electrophysics.

2002/09 ~ 2007/01 National Chiao-Tung University, Hsinchu, Taiwan Ph. D degree in
Electrophysics.

Publication List:

[1] **T. Y. Cheng**, C. W. Lin, L. Chang, C.H. Hsu, J.M. Lee, J.M. Chen, J.-Y. Lin, K. H. Wu, T. M. Uen, Y. S. Gou, J. Y. Juang," Magnetotransport properties, electronic structure, and microstructure of $La_{0.7}Sn_{0.3}MnO_3$ thin films", Phys. Rev. B **74**, 134428 (2006).

[2] **T. Y. Cheng**, C. C. Hsieh, J. Y. Juang, J. Y-.Y Lin, K. H. Wu, T. M. Uen, Y. S. Gou, C. H. Hsu, "The magneto-transport properties of epitaxial $La_{0.7}Sn_{0.3}MnO_3$ manganite thin films", Physica B **365**, 141-146 (2005).

[3] Chih-Wei Lin, **Tsan-Yao Cheng**, Li Chang, Jenh-Yih Juang, "Chemical vapor deposition of zinc oxide thin films on Y_2O_3/Si substrates", J. Crystal Growth **275**, e2481–e2485 (2005).

[4] C.W. Lin, **T.Y. Cheng**, L. Chang, and J.Y. Juang, "Chemical vapor deposition of zinc oxide thin films on Y_2O_3/Si substrates", Phys. Stat. Sol.(c) **1**, 851 (2004).

[5] **T. Y. Cheng**, P. I. Lin, S. F. Chen, S. J. Liu, J. Y. Juang, J.-Y. Lin, K. H. Wu, T. M. Uen, Y. S. Gou, R. L. Wang, H. C. Li, "Superconducting $NdBa_2Cu_3O_{7-\delta}$ (NBCO) Thin Films Grown on Bare (1$\underline{1}$02) Sapphire by Pulsed Laser Deposition", J. Low Temp. Phys. **131**, 557 (2003).